A new modelling method for representing the effect of spiral flow on the bed shear stress

M.C. Bregman

A new modelling method for representing the effect of spiral flow on the bed shear stress

by

M.C. Bregman

to obtain the degree of Master of Science
at the Delft University of Technology,
to be defended publicly on Tuesday May 1st, 2018 at 11:00 AM.

Student number:	4172027	
Project duration:	June 12, 2017 – May 1, 2018	
Thesis committee:	Prof. dr. ir. W. S. J. Uijttewaal,	TU Delft
	Dr. ir. E. Mosselman,	TU Delft, Deltares
	Dr. ir. C. J. Sloff,	TU Delft, Deltares
	Dr. ir. R. J. Labeur,	TU Delft
	Dr. ir. W. Ottevanger,	Deltares

Cover photo: The Morava river near Strážnice (Czech Republic), Zbyněk Hruboš,
<https://www.flickr.com/photos/hrubos/21360264055>

TU Delft

Deltares

Preface

This graduate thesis is an exploratory research into new modelling methods for representing the effect of spiral flow on the bed shear stress. The research was carried out at Deltares and concludes the master's degree in Civil Engineering (track Hydraulic Engineering) at Delft University of Technology.

I would like to thank my graduation committee for their supervision and advice during this research. Firstly, thanks go out to Erik Mosselman and Kees Sloff for the helpful and pleasant conversations during the period I was still orientating on a topic for my graduate thesis, and later for offering the opportunity to conduct this research at Deltares. I am thankful to be given the opportunity to be part of Deltares as a graduate intern. Thanks go out to Erik Mosselman for his efforts as a daily supervisor, playing a crucial role in mentoring me and keeping me focused on the main goal. I would like to thank Kees Sloff for his positive attitude and the valuable coffee-machine conversations about the research, which were often very helpful. I thank Wim Uijttewaal for chairing the committee and his advice on how to set up a scientifically sound research. Thanks also go out to Robert Jan Labeur, for emphasizing the importance of understanding the underlying physics and his elaborate reviews on the progress reports, which pushed me to write a decent and understandable report. Last but not least, I would like to thank Willem Ottevanger for his crucial role in this thesis by assisting me with modelling, and moreover for being a critical sounding board during my journey in unravelling the world behind spiral flow and numerical models. Besides my committee, thanks go out to Mohamed Nabi for addressing my questions about Delft3D that go beyond the manuals.

Moreover, I would like to thank everyone who became part of my life during my time at Delft University of Technology. It was a wonderful time, in which I learned so much more than only that what is necessary to obtain a degree. Many experiences will stay with me the rest of my life. I feel blessed and privileged to have had this opportunity. Special thanks go out to my parents and family, for supporting and motivating me during my studies. And, most of all, for reminding me and making me realise that there is much more in life than just studying and career.

Martijn Bregman
Delft, April 2018

Summary

This thesis presents a new methodology for representing the effect of spiral flow on the bed shear stress, using a low-vertical-resolution three-dimensional model. Furthermore, it discusses the performance of the new methodology in comparison with conventional three-dimensional and depth-averaged models.

Spiral flow is of importance for the morphological development of rivers. It is associated with curved flow found in meandering and braiding rivers and estuaries. One of the effects of spiral flow is an outward transport of streamwise momentum, affecting the streamwise velocity and sediment transport capacity. Furthermore, spiral flow causes the bed shear stress direction to deviate inward from the main flow direction. This affects the river morphology and can lead to erosion at the outer bank and bed, along with the formation of point bars at the inner bend. Numerical models have been developed to support engineers and scientists in understanding and predicting river behaviour. As far as spiral flow is considered, it is of importance to distinguish three-dimensional models from depth-averaged (two-dimensional) models. Three-dimensional models are able to represent three-dimensional phenomena such as spiral flow. However, the accuracy of the bed shear stress direction computed by these models depends strongly on the vertical grid resolution near the bed. This is due to the approach of equating the bed shear stress direction to the flow direction in the bottommost layer. A finer resolution leads to more accurate results, but also increases the required computational demand. Depth-averaged models are still commonly used due to their much lower computational demand. However, these are unable to resolve three-dimensional flow phenomena, which has led to the development of parametrisations in order to include the effects of spiral flow on the bed shear stress direction. The accuracy and area of application of depth-averaged is limited by a large number of simplifications and assumptions underlying these parametrisations.

The gap between depth-averaged and three-dimensional models is large in terms of computational demands, which is a crucial factor in hydro-morphodynamic models. The use of three-dimensional models becomes much more feasible when drastically reducing the vertical resolution. However, this comes at the cost of the accuracy of the computed bed shear stress direction. The new methodology presented in this thesis, referred to as *3D-LowRes-SemiPar*, circumvents this problem by supplementing a low-vertical-resolution three-dimensional model with a semi-parametrisation. The new methodology builds on the work of De Vriend (1976), who developed parametrisations based on analytical derivations from a simplified mathematical model. It is based on the spiral flow intensity, which is in essence a description of the relative magnitude of the secondary flow velocity profile. The spiral flow intensity can be determined on the basis of a normalised secondary flow profile derived by De Vriend (1976). The first calculation method presented in this research is based on the entire secondary flow profile obtained from the model data, the second method is based on solely the bottommost part. The latter is a refinement of the method and yields more accurate results, as the bed shear stress depends on the near-bed flow. De Vriend (1976) derived a relation for the transverse bed shear stress component based on the spiral flow intensity. This relation is obtained by determining the angular deviation of the combined velocity vector at the bed, where the flow velocity equals zero. This yields a description of the bed shear stress direction. As a result, the required vertical resolution is reduced to 5 equidistant layers, yielding a significant reduction of computational demands. The new methodology provides accurate results in sections with developed spiral flow. However, deviations are found in sections of the bend at which the spiral flow is either developing or decaying. This is due to the relatively faster adaptation of spiral flow close to the bed. As a result, the transverse velocities increase strongly close to the bed, which is not fully captured in low-vertical-resolution three-dimensional models.

Furthermore, comparisons with measurements show that three-dimensional models generally capture the flow pattern relatively well in mildly curved bends. In contrast to this, depth-averaged models face more issues in representing spiral flow. These models are inherently unable to account for the momentum redistribution due to spiral flow. However, the largest problem of depth-averaged models is caused by the parametrisation representing the effects of spiral flow on the bed shear stress. It was found that the angular deviation of the bed shear stress from the main flow direction is significantly underestimated.

Contents

List of Figures

List of Tables

Nomenclature

Abbreviations

2DH	Two-dimensional (depth-averaged)
3D	Three dimensional
BSS	Bed shear stress
D3D-FM	Delft3D Flexible Mesh Suite
DNS	Direct numerical simulation
HighRes	High-vertical resolution (3D model, 15 or more equidistant layers)
LES	Large eddy simulation
LowRes	Low-vertical resolution (3D model, up to 5 equidistant layers)
RANS	Reynolds-averaged Navier Stokes
SemiPar	Semi-parametrisation for determining the bed shear stress direction (applied to a 3D-LowRes model)

Latin symbols

A	Combined viscosity, existing of both the molecular (η) and eddy (ν_t) viscosity	[m^2/s]
B	Channel width	[m]
C	Chézy roughness coefficient	[$m^{1/2}/s$]
f_n	Dimensionless velocity profile in the normal direction	[-]
f_s	Dimensionless velocity profile in the streamwise direction	[-]
f_w	Distribution function describing the strength of the secondary flow over the width of the channel	[-]
f_{dev}	Tangent of the deviation angle of the combined velocity profile relative to the main flow direction	[-]
Fr	Froude number $Fr = \frac{v}{\sqrt{gh}}$	[-]
g	Gravitational acceleration	[m/s^2]
H	Overall mean depth	[m]
h	Local water depth	[m]
i_s	Spiral flow intensity as defined by De Vriend (1976)	[m/s]
I_{2D}	2DH Spiral flow intensity definition used in this research	[m/s]
I_{3D}	3D Spiral flow intensity definition used in this research	[m/s]
i_j	Water level gradient ($j = s, n$)	[-]
$i_{s,2}$	Spiral flow intensity as defined by De Vriend (1976) without the scaling factor	[m/s]

k_s	Nikuradse roughness length scale	[m]
L	Characteristic length	[m]
L_m	Mixing length	[m]
N	Number of measured or modelled velocity vectors in $0 < z/h < 1$	[m]
n	Manning friction coefficient	[s/m$^{1/3}$]
n	Normal space coordinate	[m]
p	Uniform pressure term	[kg/ms^2]
Q	Discharge	[m^3/s]
R	Radial coordinate in a cylindrical coordinate system	[m]
R_c	Radius of curvature of the channel centreline	[m]
R_s	Radius of curvature of the streamlines of depth-averaged flow	[m]
Re	Reynolds number $Re = \frac{v*L}{\nu}$	[-]
s	Streamwise space coordinate	[m]
t	Time	[s]
U	Cross-sectional averaged mean velocity	[m/s]
U_s	Depth-averaged velocity component	[m/s]
$U_{s,channel}$	Cross-sectional averaged mean velocity in the main channel (only applicable to Case 3)	[m/s]
v	Characteristic velocity	[m/s]
$v'(t)$	Fluctuating velocity component	[m/s]
$v(t)$	Instantaneous flow velocity	[m/s]
v_n	Transverse velocity component	[m/s]
v_s	Streamwise velocity component	[m/s]
v_v	Vertical velocity component	[m/s]
$v_{n,1}$	Transverse component of the bottommost velocity vector	[m/s]
$v_{s,1}$	Streamwise component of the bottommost velocity vector	[m/s]
$\overline{v}$	Time-averaged velocity component. The overbar is omitted after Equation 2.5	[m/s]
z	Vertical space coordinate	[m]
z_0	Bed roughness height	[m]
z_b	Bed level	[m]
z_s	Water surface level	[m]
Δz_b	Distance between the computed bottommost velocity vector and the bed level	[m]

Greek symbols

α	Friction parameter	[-]

ϵ_p	Bed porosity	[-]
η	Molecular viscosity	[m^2/s]
κ	Von Kármán constant	[-]
ν_t	Eddy viscosity	[m^2/s]
Φ	Tangential coordinate in a cylindrical coordinate system	[m]
ϕ_τ	Deviation between the angles of the bed shear stress and depth-averaged velocity	[°]
ϕ_v	Deviation between the angles of the flow in the bottommost computational layer and depth-averaged velocity	[°]
ρ	Water density	[kg/m^3]
σ_{ij}	Normal components of the Reynolds stress tensor ($i, j = s, n$)	[N/m^2]
τ_b	Bed shear stress vector	[N/m^2]
τ_{bn}	Bed shear stress component in streamwise (s) direction	[N/m^2]
τ_{bs}	Bed shear stress component in transverse (n) direction	[N/m^2]
τ_{ij}	Shear components of the Reynolds stress tensor ($i, j = s, n$)	[N/m^2]
θ_τ	Direction of the bed shear stress	[°]
θ_U	Direction of the cross-section averaged main (depth-averaged) flow	[°]
θ_{U_s}	Direction of the local main (depth-averaged) flow	[°]
θ_{v_1}	Direction of the flow in the bottommost computational layer	[°]

1 Introduction

1.1. Research context

Rivers are of great importance for mankind. The conveyance of water and sediments offers fresh water, land fertilisation and possibilities for navigation. River courses are subject to continuous change, especially in mild-slope alluvial plains. These changes can be induced by external factors, such as sea level rise, changing rainfall patterns and human interventions. Most rivers also have a natural tendency to continuously change course, of which the phenomenon called meandering is a well-known example. This causes the river to assume a winding shape which is continuously changing, due to erosion of the outer bend and deposition of sediments at the inner bend. This gives rise to potentially undesired effects such as bank erosion, land loss, erosion around bridge pillars and sedimentation of navigation channels. On the other hand, a more recent development is the tendency of managing authorities to renaturalise rivers which have been (partially) canalised (Blanckaert and De Vriend, 2003). This has led to a demand for understanding and predicting river behaviour. Furthermore, it is desired to be able to understand the influence of human interventions on the river system. Therefore many studies have been carried out into river dynamics, of which river meandering is an important part. An example is shown in Figure 1.1:

Figure 1.1: The Luangwa River in Zambia during a low-discharge period, showing point bars at the inner bends and the effects of erosion at the outer bends (Waite, 2017)

1.1.1. Spiral flow

Secondary flow patterns are characteristic features of curved open-channel flow. These features not only play an important role in meandering rivers, but are also of importance for other systems such as braiding river and estuaries. The predominant secondary flow pattern found in curved open channel flow is known as spiral or helical flow. Spiral flow induces additional velocity components perpendicular to the main flow direction, which strongly vary with depth. These components are generally directed toward the inner bend in the lower part of the water column, and toward the outer bend in the upper part, as seen in Figure 1.2:

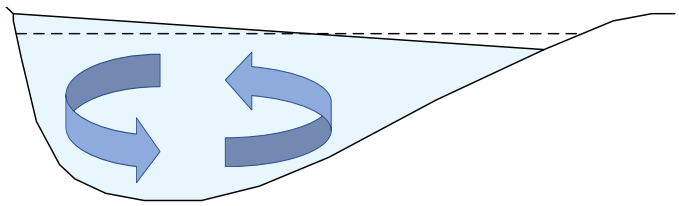

Figure 1.2: Simplified cross-sectional view of spiral flow

Spiral flow velocities are generally an order of magnitude smaller than the streamwise flow velocity. Nevertheless, important implications remain for the hydro- and morphodynamics. Among other things, spiral flow induces a redistribution of the main flow velocities which affects the sediment transport capacity. Furthermore, spiral flow causes the bed shear stresses to deviate inward from the main flow direction. As a result, a net sediment transport toward the inner bend is found. The changes in sediment transport are of influence on the river morphology. Due to the aforementioned effects, often erosion of the bed and banks at the outer bank is observed, together with the formation of point bars at the inner bend.

1.1.2. Modelling spiral flow

Numerical models have become an important tool for river engineers in understanding and predicting river behaviour. Despite the progress made so far, many assumptions and simplifications are still underlying river engineering models, which can affect the accuracy of the model results. Roughly, this is because of three reasons. At first, some physical processes are not entirely understood. Secondly, some processes are impossible or very complicated to numerically solve entirely, such as turbulence. Finally, simplifications such as dimensionality reduction can be made in order to further reduce the computational demand, which is a crucial factor in river engineering practice. The latter especially applies to hydro-morphodynamic models, due to the large computational requirements when modelling the constant interaction between the flow field and the channel morphodynamics.

Depth-averaged (2DH) models are still commonly used in river engineering practice, mainly due to their much lower computational demand. However, these models are inherently unable to solve three-dimensional flow phenomena. This leaves important implications for the flow field, because no account is taken of spiral flow. Therefore researchers have developed parametrisations in order to include the effects of spiral flow on the bed shear stress direction. These parametrisations are based on analytical derivations, obtained by considering a simplified momentum balance for fully developed flow in an idealized geometry. In essence, these parametrisations are therefore only valid at the centreline of an infinitely long bend with a mild curvature ratio and constant width. In order to apply the parametrisations to more natural geometries, additional descriptions are developed to account for the width distribution and the streamwise adaptation of the flow.

Three-dimensional (3D) models are able to represent three-dimensional phenomena such as spiral flow. These models assume a bed shear stress direction which is equated to the flow direction at the bottommost layer. As a result, the direction depends on the thickness of the bottommost layer. The direction can vary strongly with the thickness, due to the strong variability of the secondary flow velocity component over depth. The thickness depends on the resolution applied within the model.

1.2. Problem statement

Spiral flow is an important phenomenon in curved open-channel flow. It leads, among other things, to a deviation of the bed shear stress from the main flow direction. Depth-averaged models are unable to resolve spiral flow. This has led to the development of parametrisations which account for the deviation of the bed shear stress angle. However, these parametrisations are based on many assumptions and simplifications, which can be disadvantageous for the accuracy of model results. The latter might especially be the case when modelling geometries which differ strongly from the idealised conditions underlying these parametrisations. Three-dimensional models are able te resolve the phenomenon of spiral flow. Therefore these models automatically account for the angular deviation of the bed shear stress. The accuracy of the deviating bed shear stress direction depends on the layer thickness of the bottommost layer, due to the strongly varying flow

direction over depth. Consequently, a higher model resolution is likely to yield more accurate predictions. However, computational expenses will increase as well, which can be undesired in engineering practice.

In summary, both 2DH and 3D models have their own drawbacks. Depth-averaged models are computationally relatively inexpensive but potentially inaccurate, especially for more arbitrary geometries. Three-dimensional models have the potential to be relatively accurate, but are computationally an order of magnitude more expensive, especially for high-vertical-resolution models required for accurate modelling of the bed shear stress angle.

1.3. Objective and research questions

1.3.1. Objective

The objective of the research is to explore a new methodology in the context of the shortcomings of conventional 2DH and 3D models. The research aims to develop and assess a new methodology using low-vertical-resolution 3D models, supplemented by a modification. This modification, hereafter referred to as *semi-parametrisation*, aims to compute the angular deviation of the bed shear stress independent of the applied vertical resolution. This allows the use of low-vertical-resolution 3D models, leading to a significant reduction of computational expenses compared to conventional 3D models. At the same time, this new methodology is expected to yield more accurate results than 2DH models, especially in case of more arbitrary geometries. The first step required for achieving this objective is to obtain insight in the simplifications and parametrisations used in conventional 3D and 2DH models, and to understand their limiting effects on model results.

1.3.2. Research questions

Based on these objectives two main research questions are formulated for this research:

1. *How do the simplifications and parametrisations applied to conventional 2DH and 3D models affect the representation of spiral flow and the influence of spiral flow on the bed shear stress?*

2. *How can the bed shear stress vector be determined more accurately in a low-vertical-resolution 3D model?*

The first question is subdivided in the following sub-questions:

1.1 *What are the additional parametrisations in 2DH models required for simulating the effects of spiral flow, and how are these derived?*

1.2 *How is the accuracy of 3D and 2DH models affected by the applied simplifications and parametrisations, considering both idealized and more arbitrary geometries?*

The second question is subdivided as follows:

2.1 *What kind of methodology is required to enable a more accurate description of the bed shear stress vector in a low-vertical-resolution 3D model?*

2.2 *What is the performance of this new methodology in describing the bed shear stress vector, compared to conventional 2DH and high-vertical-resolution 3D models, for both idealized and more complex geometries?*

1.4. Approach

Research question 1.1 is answered by an investigation into (1) the basic equations used for modelling open-channel flow, (2) the required simplifications for solving these equations and (3) the additional parametrisations used in 2DH models. Subsequently, research question 1.2 is answered by modelling multiple cases, ranging from idealized to more arbitrary geometries. As stated before, spiral flow is interconnected with morphology. However, within the context of this research only hydrodynamic computations are carried out. This is due to the focus on describing the bed shear stress vector, which can be determined based on the flow field. The results of 2DH and 3D models are compared to one another and measurement data. In this way, deviations in the model results can be related to the simplifications and parametrisations applied to these models. Recommendations are made for future measurement studies in case of lacking measurement data.

Research question 2.1 is answered by developing the aforementioned new methodology, which is a low-vertical-resolution 3D model supplemented with a semi-parametrisation for the bed shear stress direction. This semi-parametrisation originates from the same mathematical model De Vriend (1976) used for the parametrisations used in 2DH models. The new methodology has not been applied yet in 3D hydro-morphodynamic models. In order to answer research question 2.2, a comparison is made between the new methodology based on low-vertical-resolution 3D models on the one hand, and conventional 2DH and high-resolution 3D models on the other hand.

1.5. Outline

In Chapter 2 a review is given of relevant literature concerning spiral flow. This includes an explanation of the underlying physics, mathematical descriptions and existing modelling approaches. Chapter 3 elaborates the new methodology forming the basis of this research. Subsequently, Chapter 4 gives a description on the modelling approach which is used for validating the methodology. Chapter 5 presents the results obtained in this research. An interpretation and discussion of these results is given in Chapter 6. Finally, the conclusions and recommendations for further use and research are described in Chapter 7.

2

Literature review

This chapter gives a summary of relevant literature for this research. After starting with a brief general summary of previous work in the field of secondary flow in Section 2.1, Section 2.2 continues with a review of the physics of curved flow, forming an important reference for the interpretation of model results later in the report. A review is given of the underlying physics of secondary flow, the influence of secondary flow on the main flow and the related morphodynamic implications. Section 2.3 starts with a mathematical description, starting with the general Navier-Stokes equations and solution methods. Subsequently, this section describes the background of the mathematical model set up by De Vriend (1976) for describing spiral flow, and closes with the descriptions of spiral flow characteristics derived from this model. The work of De Vriend (1976) forms the basis of the parametrisations used in 2DH models and the semi-parametrisation used in the new methodology presented in this research. Section 2.4 elaborates the current modelling practice of hydrodynamics in general and, more specific, the implementation of secondary flow in 2DH and 3D hydrodynamic models. Finally, Section 2.5 provides the conclusion of the literature review.

2.1. Previous research

Throughout this research, frequent references are made to the work of other authors as summarized below. The first experiments aimed on obtaining more insight in spiral flow were carried out by Thomson (1879). Some decades later, Einstein (1926) explained the phenomenon of spiral flow by referring to the well-known tea leaf paradox. This refers to the phenomenon of tea leaves moving to the centre of a cup when stirring the liquid, whereas one might expect the leaves to move to the edges due to the centrifugal force. The reason for the migration to the centre of the cup is the presence of spiral flow. First steps in obtaining mathematical descriptions of spiral flow were made by Van Bendegom (1947). More than a decade later, Rozovskii (1957) described the theory behind spiral flow, developed a comprehensive set of mathematical descriptions and conducted laboratory experiments in order to compare theory with reality. De Vriend (1976) extended the existing theories with descriptions for non-axisymmetrical flow in mildly curved bends and provided an important basis for depth-averaged computational methods. Later he further extended his theories in his PhD thesis (De Vriend, 1981). Bathurst et al. (1977) reported the existence of the outer bank cell in measurements in natural river bends. Shortly thereafter, De Vriend and Koch (1977) carried out laboratory measurements on mildly curved bends with a flat bed, and subsequently on a geometry with a developed bathymetry (De Vriend and Koch, 1978). Furthermore, De Vriend (1979) conducted measurements in moderately curved bends. At the time, depth-averaged numerical computations were executed by De Vriend and Kalkwijk (1980) and Booij and Pennekamp (1984). Koch (1981) researched the performance of a three-dimensional modelling approach in curved flumes. Kalkwijk and Booij (1986) developed descriptions for the generation and decay of secondary flow based on the work of De Vriend (1976), forming an important basis for multiple 2DH numerical models. Thorough research into turbulence features in curved flow was conducted by Blokland (1985). Struiksma et al. (1985) made steps in obtaining more insight in bed deformation in alluvial rivers with experiments in several flumes, a theoretical analysis of a mathematical model and the development of a depth-averaged morphological model. This is connected to the work of Olesen (1987), who developed the mathematical model in order to obtain more insight in the morphodynamic behaviour. More recently, Blanckaert and De Vriend (2003) and Ottevanger et al. (2009) developed a new method to model strongly curved flows, as existing models of-

ten failed to reproduce these flows correctly. Alongside, measurements were conducted at strongly curved bends by Blanckaert and Graf (2004), Blanckaert and De Vriend (2004) and Blanckaert (2009). Another recent development is the use of detailed large eddy simulations, which generally yield a very accurate representation of flow features. Booij (2003) and Van Balen (2010) used this modelling technique to obtain more insight in detailed flow features. Recently Ottevanger (2013) focussed in his research on flow phenomena found in (strongly) curved flow and the ability of a wide range of models to represent these phenomena.

The objective of the authors mentioned above was to obtain more insight in spiral flow or to develop improved modelling methods, or a combination thereof. Many of these authors based their work on idealized and controlled laboratory experiments or strongly simplified mathematical models. Their findings form an important basis for simplifications and parametrisations adopted in hydro-morphodynamic models, such as Delft3D. However, these models are generally used for real-world geometries, which are often much more arbitrary than the simplified cases forming the basis of parametrisations implemented in 2DH models.

2.2. Physics of curved open-channel flow

The qualitative description of the flow pattern in open-channel bends as given in this section forms an important basis for the assessment of the model results in the remainder of this research. The description is partly based on the work of De Vriend (1981) and Blokland (1985). These authors based their work upon experimental and theoretical investigations into spiral flow. The definitions used for main and secondary flow are the same as defined by De Vriend (1978). An impression of the shape of the combined flow pattern is indicated by the blue vectors and orange curve in Figure 2.1. Main flow is defined as the flow component in the direction of the streamline of the depth-averaged flow. This is indicated by the green plane which is in the same direction as the s-axis. The main flow direction not necessarily coincides with the direction of the channel axis. Spiral flow induces a deviation in the vertical distribution of the flow, as indicated by the orange line and purple plane. Hence, secondary flow is defined as the component of the combined flow which is perpendicular to the main flow direction, as indicated by the n-axis. This means that the depth-averaged secondary flow is equal to zero by definition.

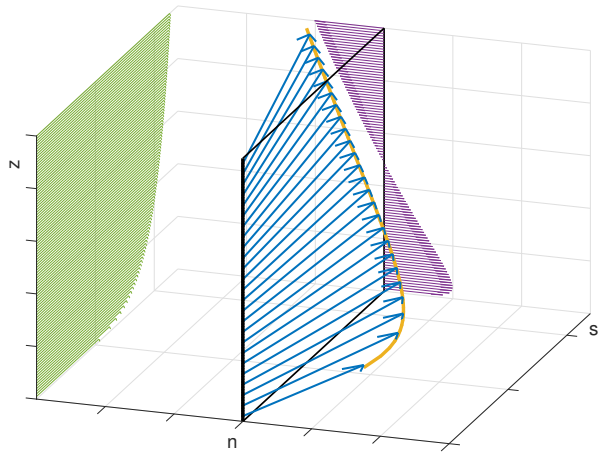

Figure 2.1: Schematic 3D-plot of combination of main and secondary flow

2.2.1. Secondary flow

Main spiral flow cell

Spiral flow is the predominant secondary flow pattern in curved open-channel flow. The underlying principle of spiral flow in river bends is shown in Figure 2.2:

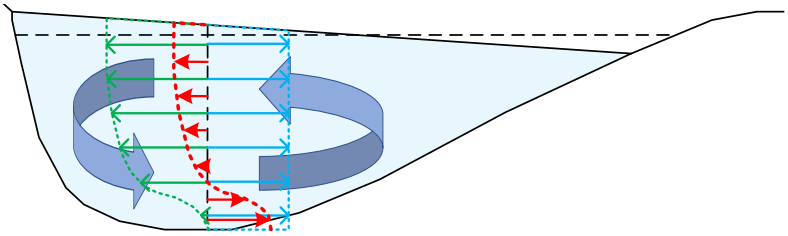

Figure 2.2: Cross-sectional view of the forcing of spiral flow

Spiral flow is caused by an interaction between a centrifugal acceleration induced by the curvature of the flow (green) and a centripetal acceleration caused by pressure forces induced by a transverse water level gradient (blue). The magnitude of the centrifugal acceleration is related to the main flow velocity. Due to the decreasing influence of the channel bed higher in the water column, the main flow velocity increases with the distance from the bed. As a result, the centrifugal acceleration increases as well with distance from the bed. The latter is due to the scaling of centrifugal acceleration with the velocity squared. At the same time, the required balancing centripetal acceleration emerges due to the development of the cross-stream water surface gradient. This acceleration is distributed uniformly over the water column in case of hydrostatic pressure, which is generally a justifiable assumption. The total centripetal and centrifugal accelerations are in balance in case of developed secondary flow. However, when considering the distribution over the water column, the centripetal acceleration is larger in the lower part, whereas the centrifugal acceleration is larger in the upper part. This leads to a shear stress gradient over depth, initiating an inward secondary flow near the bottom and an outward secondary flow near the water level surface, as shown by the net forcing indicated in red Figure 2.2. These components are generally an order of magnitude smaller than the main flow velocity. Vertical flow velocities arise due to continuity, namely upward at the inner bend and downward at the outer bend. The overall result is a spiralling motion of the flow. In reality, some distance along the channel is required for the secondary flow to develop, due to inertia of the flow. A more detailed three-dimensional representation of secondary flow and associated effects is shown in Figure 2.3.

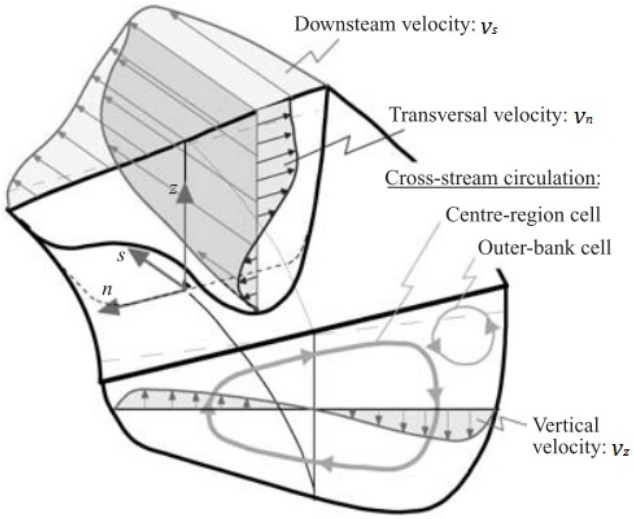

Figure 2.3: Comprehensive conceptual sketch of processes and phenomena related to secondary flow in river bends (Blanckaert and De Vriend, 2004)

Outer-bank cell

Another notable secondary flow phenomenon found in river bends is the outer-bank cell, first reported by Bathurst et al. (1977). An impression is found in the schematic overview in Figure 2.3. It is mainly observed in sufficiently curved channels with steep walls. The outer-bank cell is located in the upper part of the water column near the outer bend side wall. The width of the cell is much smaller and the direction of rotation is opposite compared to the main secondary flow cell. Most authors, among whom Blokland (1985) explain the

origin of the outer-bank cell by weak secondary flows found in the corners of the cross-section of a straight channel section. These weak secondary flows are caused by the anisotropy of turbulence. In case of a transition from straight to curved flow, the mentioned small secondary flows are influenced by the main secondary flow cell. This leads to the amplification of the secondary cell near the outer bank surface. This continues until a new equilibrium is reached, in which the outer bank cell can be clearly recognized. The weak secondary flow cells near the bed are either damped out or merged into the main secondary flow.

Predicting the effect of the outer bank cell on the morphodynamics is relatively complicated. This is due to two counteractive effects of the outer bank cell, as described by Blanckaert et al. (2012). The first effect is due to widening of the outer-bank boundary layer by the cell, leading to a reduction of the forcing on the channel bed and bank. However, the second effect is the forcing of high-momentum flow toward the lower part of the bank induced by the cell, enhancing the flow forcing on the bed and lower part of the bank.

2.2.2. Main flow

Blokland (1985) gives an explanation about the two most important factors related to secondary flow, which influence the cross-sectional distribution of the main flow velocity. Firstly, the transverse water level gradient i_n plays an important role, which emerges directly at the entrance of a bend. Low water levels are found at the inner bend, and high levels at the outer bend. As a result, the streamwise (or longitudinal) water level slope i_s is relatively large at the inner bend and relatively small at the outer bend. As a consequence, the streamwise flow accelerates along the inner bend and decelerates along the outer bend. Hence, the largest velocities are found along the inner bend. Further along the bend, this difference is mitigated by the bed shear stress, which increases quadratically with the flow velocities.

The second factor is explained by, among others, De Vriend (1981) and Blokland (1985) as the convective influence of the secondary flow on the main flow. This effect becomes dominant at some distance from the entrance of the bend and reverses the initial transverse velocity distribution induced by the deviating longitudinal water level gradients. The radial convection induced by spiral flow conveys low-momentum flow from the lower part of the water column upward at the inner bend, leading to a deceleration of the main flow in this area. Because the radial convection is the largest near the surface, the largest deceleration is found in this area. Along the inner bend, this results in a downward shift of maximum streamwise flow velocities from the surface to some distance below the water surface. On the contrary, the opposite occurs along the outer bend. Due to the radial convection, high-momentum fluid from the upper part of the water column is conveyed downward, leading to an acceleration of the main flow velocity. This effect is the largest near the surface, however, it is damped significantly in case the aforementioned outer-bank cell is present. In summary, the convective influence of secondary flow on the main flow leads to a shift of maximum flow velocities toward the outer bend.

2.2.3. Morphodynamics

Spiral flow is of significant importance for the channel morphodynamics. This is partly due to an inward directed deviation of the bed shear stress direction from the main flow direction, caused by the inward directed secondary flow component near the bed. As a result, a net sediment transport occurs towards the inner bend. This leads to a transverse bed slope (α) accommodating larger depths in the outer bend (Olesen, 1987). The forcing on the bed consists of drag (F_d), gravitational (W), normal (N) and friction (F_f) forces, as seen in Figure 2.4.

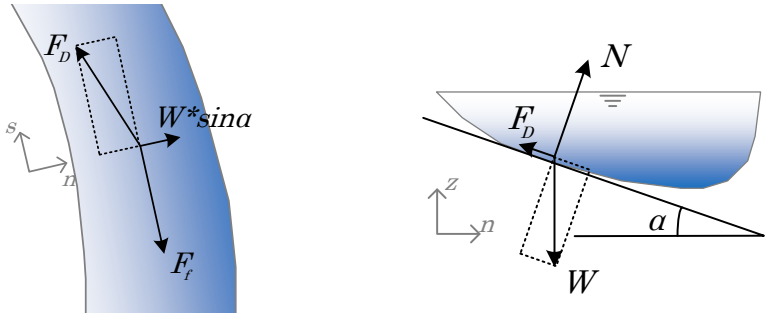

(a) Top view (b) Cross-section

Figure 2.4: Forcing of the flow on the river bed (Olesen, 1987, modified)

Furthermore, the aforementioned momentum redistribution induces an additional velocity increase at the outer bend and a decrease at the inner bend. The asymmetric width distribution of streamwise velocities leads to erosion and undermining of the outer bank and sedimentation at the inner bend. This results in erosion of the outer bank and formation of points bars at the inner bend. Both phenomena are associated with braiding and meandering rivers, and are as well of relevance in estuarine systems.

2.3. Mathematical description

This section describes the mathematical model set up by De Vriend (1976) for describing spiral flow, forming the basis of parametrisations used in 2DH models and the semi-parametrisation used in the new methodology presented hereafter in Chapter 3.

2.3.1. Basic flow equations

The motion of incompressible viscous fluids can be described by the Navier-Stokes equations, consisting of partial differential equations describing the conservation of mass and momentum. The equations form the starting point for many derivations underlying hydrodynamic models and analytical descriptions of flow. Generally these equations are expressed in a Cartesian coordinate system. However, in this research they are expressed by Equations 2.1 to 2.4 using a cylindrical coordinate system (Φ, R, z), which is more convenient for obtaining analytical descriptions of curved flow. However, analytical solutions based on this set of equations are limited to channels with a constant width and a fixed radius of curvature. The Φ-axis is taken along the channel axis, the R-axis is taken perpendicular to the channel axis and the z-axis indicates the vertical direction with $z = 0$ at the river bed. The equations are expressed as follows, after De Vriend (1976):

$$\frac{\partial v_\Phi}{\partial \Phi} + \frac{\partial v_R}{\partial R} + \frac{v_R}{R_c} + \frac{\partial v_z}{\partial z} = 0 \tag{2.1}$$

$$\frac{\partial v_\Phi}{\partial t} + v_\Phi \frac{\partial v_\Phi}{\partial \Phi} + v_R \frac{\partial v_\Phi}{\partial R} + v_z \frac{\partial v_\Phi}{\partial z} + \frac{v_\Phi v_R}{R_c} = \frac{1}{\rho}\left[\frac{\partial \sigma_{\Phi\Phi}}{\partial \Phi} + \frac{\partial \tau_{\Phi R}}{\partial R} + \frac{\partial \tau_{\Phi z}}{\partial z} + 2\frac{\tau_{\Phi R}}{R_C}\right] \tag{2.2}$$

$$\frac{\partial v_R}{\partial t} + v_\Phi \frac{\partial v_R}{\partial \Phi} + v_R \frac{\partial v_R}{\partial R} + v_z \frac{\partial v_n}{\partial z} - \frac{v_\Phi^2}{R_c} = \frac{1}{\rho}\left[\frac{\partial \tau_{\Phi R}}{\partial \Phi} + \frac{\partial \sigma_{RR}}{\partial R} + \frac{\partial \tau_{Rz}}{\partial z} + \frac{\sigma_{RR}}{R_c} - \frac{\sigma_{\Phi\Phi}}{R_c}\right] \tag{2.3}$$

$$\frac{\partial v_z}{\partial t} + v_\Phi \frac{\partial v_z}{\partial \Phi} + v_R \frac{\partial v_z}{\partial R} + v_z \frac{\partial v_z}{\partial z} = \frac{1}{\rho}\left[\frac{\partial \tau_{\Phi z}}{\partial \Phi} + \frac{\partial \tau_{Rz}}{\partial R} + \frac{\partial \sigma_{zz}}{\partial z} + \frac{\tau_{Rz}}{R_c}\right] - g \tag{2.4}$$

In which v_Φ, v_R and v_z represent the velocity components in tangential, radial and vertical directions, respectively. Additionally, g represents the gravity term and ρ the mass density of the fluid, and furthermore $\sigma_{\Phi\Phi}$, σ_{RR}, σ_{zz}, $\tau_{\Phi R}$, τ_{Rz} and $\tau_{\Phi z}$ represent the normal and shear components of the stress tensor, respectively. Compared with the Navier-Stokes equations in a Cartesian coordinate system, the following additional terms emerged:

- inertia terms ($\frac{v_\Phi v_R}{R_c}$ and $\frac{v_\Phi^2}{R_c}$ in Equations 2.2 and 2.3 resp.)
- stress terms ($\frac{2\tau_{\Phi R}}{R_c}, \frac{\sigma_{RR}}{R_c} - \frac{\sigma_{\Phi\Phi}}{R_c}$ and $\frac{\tau_{Rz}}{R_c}$ in Equations 2.2 to 2.4 resp.)

The set of partial differential equations forming the Navier-Stokes equations have a non-linear character for flows with moderate and high Reynolds numbers. Analytical solutions are difficult or impossible to find for these flows.

2.3.2. Reynolds-averaging

The time-averaged motion of the flow can be described by the Reynolds-averaged Navier-Stokes (RANS) equations, which are obtained by applying the concept of Reynolds decomposition or averaging to the Navier-Stokes equations. The RANS equations not only form the basis of many hydrodynamic models, but for analytical descriptions of flow properties as found later in this report as well. The underlying concept is separation of the instantaneous flow velocity $v(t)$ is a time-averaged $\overline{v}$ and a fluctuating component $v'(t)$, as represented by Equation 2.5:

$$v(t) = \overline{v} + v'(t) \tag{2.5}$$

The method of Reynolds averaging enables description of the mean flow properties. Additional components of the total stress tensor, known as the Reynolds stresses, are obtained as a result of the averaging procedure. The Reynolds stresses account for the effect of turbulent fluctuations on the momentum balance. Additional formulations, known as turbulence closure models, are developed to approximate the Reynolds stresses, of which no exact description has been found yet. The formulations make use of the Boussinesq (1868) hypothesis which relates the Reynolds stresses to the mean flow properties. These formulations are coupled into a turbulence closure model. Multiple turbulence closure models are available, using varying approaches with different complexity levels. An overview of these models is given by Rodi (2017). A more elaborate explanation of the Boussinesq hypothesis and closure models can be found in Appendix A. Henceforth, the overbar is omitted for the time-averaged quantities $\overline{v_\Phi}$, $\overline{v_R}$ and $\overline{v_z}$.

2.3.3. Method of solution

Background

The starting point of the derivations of De Vriend (1981) is formed by the RANS equations, after applying the Boussinesq hypothesis. The system of equations can be found in Equations B.1 to B.3 in Appendix B. De Vriend (1981) used this mathematical model for studying properties of curved flow. Derivations based on the mathematical model give more insight into flow phenomena, among which spiral flow. Furthermore, it is impossible to calculate three-dimensional flow phenomena when using reduced-dimension models. In this case, parametrisations are required, which are often based on the work of De Vriend (1981) or further elaborations of other researchers, such as Kalkwijk and Booij (1986), Olesen (1987), Blanckaert and De Vriend (2003) and Ottevanger et al. (2009). The new methodology presented in this research is also partially based on parametrisations of De Vriend (1981). De Vriend and Kalkwijk (1980) summarized the following restrictions which apply to the derivations:

- the depth to width ratio (h/B) is small
- the curvature ratio (B/R_c) is small
- the horizontal length scale of bottom variations in streamwise direction is at least of the order of magnitude of the channel width
- the flow is mainly friction controlled
- the streamwise flow component is predominant
- the Froude number is small

Conversion of coordinates

The descriptions of De Vriend (1981) are derived from a cylindrical coordinate system. Therefore these are only valid along the centreline of an axisymmetric bend. In reality, the direction of the local main flow direction not necessarily corresponds with the tangential direction in a cylindrical coordinate system, especially in case of strongly curved geometries. Nevertheless, the assumption is generally made that the descriptions derived along the centreline also apply in the direction of the main flow. This reasoning is common in describing spiral flow, and is therefore also used in the remainder of this research. This means that in the remainder of this research the tangential coordinate Φ is replaced by the streamwise coordinate s, and the radial coordinate R by the transverse coordinate n.

Additional steps

This paragraph gives a brief description of the steps taken by De Vriend (1981) in order solve the system of equations. The first step is defining three kinds of boundary conditions. At first, boundary conditions are applied at the inflow and outflow, namely the discharge Q and other conditions which may vary from case to case. In addition to these, boundary conditions are applied to the channel banks and bed. The conditions of impermeability and no-slip are used for these regions. In other words, both the normal and tangential velocities are defined to be 0 at the banks and bed. At the free surface rigid lid assumption is applied. This implies that the surface is considered as a frictionless rigid plate, only exerting normal stresses on the fluid.

De Vriend (1981) continues with normalizing the system of equations, as the equations are too complex to be solved completely. A normalization is carried out on the dominant terms within the differential equations Equations B.1 to B.3. All terms are written as the product of a constant scale factor and a variable term with order of magnitude $O(1)$. This operation restricts the applicability of the mathematical model to shallow channels with a small depth to width ratio. Furthermore, the validity is restricted to situations in which the shear stress effects dominate the inertial effects. The system is solved by means of the method of asymptotic expansion. This requires the collection of all terms of $O(1)$ in a zero-order system. Subsequently, a first-order system can be resolved in which $O(h/R_c)$ terms are included as well. Smaller order terms are neglected.

Furthermore, a turbulence closure model is adopted for resolving Equations B.1 to B.3. Only the eddy viscosity ν_t is maintained in this model, because the molecular viscosity η is assumed to be negligible. De Vriend (1981) mentions that the turbulence effects in shallow channels are most important in the vertical direction, which allows the simplification of considering the main flow as a simple shear flow in a vertical plane. This reasoning neglects the side wall effects. De Vriend (1981) uses the mixing-length model for describing the eddy viscosity:

$$\nu_t = L_m^2 \sqrt{\left(\frac{\partial v_s}{\partial z}\right)^2 + \left(\frac{\partial v_n}{\partial z}\right)^2} \tag{2.6}$$

It is mentioned by De Vriend (1981) that the mixing-length model is a crude assumption, however, it allows a simple solution and is considered to be adequate for first approximations of the shape of the main and secondary flow profiles. The secondary flow profile is based on the main flow profile, for which De Vriend (1981) assumed a logarithmic distribution. This is based on the work of Rozovskii (1957), who proved that the secondary flow profile agrees the best with the measurements when assuming a logarithmic main flow profile, rather than assuming a power-law velocity profile. The logarithmic main flow profile does not have a finite value, which is required for the no-slip boundary condition near the bed. Therefore a roughness height z_0 is prescribed at which the velocity equals 0. De Vriend (1981) assumes that this condition applies to both the main and secondary flow:

$$v_s\Big|_{z=z_0} = v_n\Big|_{z=z_0} = 0 \tag{2.7}$$

He mentions that the underlying reasoning is especially doubtful for the secondary flow, as it is unlikely that this level can be determined based on Chezy's constant as well. Nonetheless, De Vriend (1981) holds on to this assumption. Other authors use different ways of reasoning, such as Rozovskii (1957). In case of smooth beds, he assumes the transverse shear stress to vanish at some distance from the bed instead of the velocity. Subsequently, he based the transverse shear stress on the momentum balance in this small layer near the bed. In case of hydraulically rough flow, a widely applied boundary condition is given by Rozovskii (1957), who assumed a bed shear stress vector coinciding with the near-bed flow. The underlying assumption is that the bed shear stress mainly originates from roughness elements at the bed. This is fundamentally different from the case of hydraulically smooth flow, at which the bed shear stress originates from viscous effects at the bed. In case of the latter, the bed shear stress direction can differ from the flow direction near the bed. However, an issue regarding this rough-bed approach is determining the distance from the bed at which to condition can be imposed. Rozovskii (1957) determines this distance using the Nikuradse roughness length scale k_s, which is related to the Chézy roughness constant which only applies to uniform flow. De Vriend (1981) argues that it is debatable to assume the flow to be uniform near the bed. Furthermore, in case of uniform near-bed flow, Equation 2.7 can be defended as well. In summary, there are multiple ways to define the boundary conditions at the bed. The parametrisations obtained by De Vriend (1981), as shown later in this section, are based on Equation 2.7.

Linearity of parametrisations

The method developed by De Vriend (1981) as described above is a linear approach, and therefore only valid for bends with a mild curvature. This is due to the fact that these parametrisations do not account for the interaction between the main and secondary flow. Non-linear parametrisations have also been developed by, among others, Blanckaert and De Vriend (2003). The authors present a non-linear parametrisation which accounts for this interaction, and is therefore also intended to be suitable for moderate and strongly curved flow. As described before in this chapter, the interaction between the main and secondary flow leads to a flattening of the streamwise velocity profiles, which means that the flow velocity decreases in the upper part of the water column and increases in the lower part. This interaction limits the strength of the secondary flow.

2.3.4. Flow characteristics

Main and secondary flow profiles

As mentioned before, De Vriend (1976) based the streamwise velocity profile on the logarithmic distribution, which is commonly used for uniform rectilinear shear flow:

$$v_s = U_s f_s \tag{2.8}$$

In which U_s stands for the depth-averaged main flow velocity, and f_s describes the normalized vertical distribution of the streamwise flow profile:

$$f_s = 1 + \alpha + \alpha \ln\left(\frac{z}{h}\right) \tag{2.9}$$

The term z/h stands for the normalized depth ranging from 0 at the bed to 1 at the water surface. Furthermore, α is a friction parameter which is expressed as follows (in which κ represents the Von Kármán constant):

$$\alpha = \frac{\sqrt{g}}{\kappa C} \tag{2.10}$$

De Vriend (1976) obtained the secondary flow profile based on derivations of the transverse momentum balance, as given by Equation B.2. With the exception of the centrifugal term, all inertia terms are disregarded. This limits the applicability of the derivation to situations with fully developed secondary flow. Furthermore, all lateral friction terms are omitted, which can only be justified when disregarding the regions close to the side walls. As a result, the transverse momentum balance as given by Equation B.2 reduces to Equation 2.11:

$$-\frac{v_s^2}{R} + \frac{1}{\rho}\frac{\partial p}{\partial n} = \frac{1}{\rho}\frac{\partial \nu_t}{\partial z}\left(\frac{\partial v_n}{\partial z}\right) \tag{2.11}$$

In order to obtain a derivation of the secondary flow profile, a parabolic distribution of the eddy viscosity is assumed:

$$\nu_t = -\kappa^2 \alpha h U_s \left(\frac{z}{h} - 1\right)\frac{z}{h} \tag{2.12}$$

Subsequently, a derivation of the secondary flow profile can be found by substituting v_s and ν_t in Equation 2.11 by Equations 2.8 and 2.12, under the assumption of hydrostatic pressure:

$$v_n = \frac{hU_s}{\kappa^2 R_s} f_n \tag{2.13}$$

In which f_n is a complicated function describing normalised vertical distribution of the secondary flow, which is given by De Vriend (1976):

$$f_n = 2F_1 + \alpha F_2 - 2(1-\alpha) f_s \tag{2.14}$$

It is partially based on the main flow profile as given by Equation 2.9. The terms F_1 and F_2 are defined as follows:

$$F_1 = \int_{-1+z_0}^{z'/h} \frac{\ln\left(1+\frac{z'}{h}\right)}{\frac{z'}{h}} d\left(\frac{z'}{h}\right) \tag{2.15}$$

$$F_2 = \int_{-1+z_0}^{z'/h} \frac{\ln^2\left(1+\frac{z'}{h}\right)}{\frac{z'}{h}} d\left(\frac{z'}{h}\right) \tag{2.16}$$

In which z'/h and the bed roughness height z_0 are defined as follows:

$$\frac{z'}{h} = \frac{z}{h} - 1 \tag{2.17}$$

$$z_0 = e^{-1-\frac{\kappa C}{\sqrt{g}}} \tag{2.18}$$

The normalized main (f_s) and secondary (f_n) flow profile can be observed in Figure 2.5:

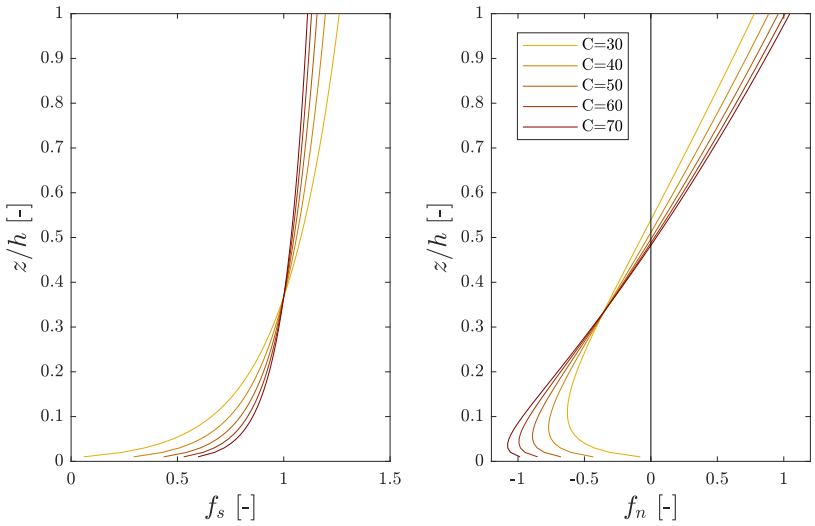

Figure 2.5: Normalised streamwise and transverse flow distributions

De Vriend (1976) defines f_{dev} as a function for the deviation of the combined flow profile from the main flow direction:

$$f_{dev} = \frac{f_n}{f_s} = \frac{2F_1 + \alpha F_2}{1 + \alpha + \alpha \ln \frac{z}{h}} - 2(1-\alpha) \tag{2.19}$$

Near the bed, where $z = z_0$, one finds:

$$f_{dev}\Big|_{z=z_0} = -2(1-\alpha) \tag{2.20}$$

Bed shear stress direction

De Vriend (1976) based his description for the bed shear components upon the vertical distributions of the shear stresses. The quadratic friction law is assumed to apply for the streamwise bed shear stress:

$$\tau_{bs} = \frac{\rho g}{C} U_s^2 \tag{2.21}$$

The transverse bed shear stress component is based on the quadratic friction law as well, and is partly based upon Equation 2.20

$$\tau_{bn} = 2\rho\alpha^2(1-\alpha)\frac{hU_s^2}{R_s} \tag{2.22}$$

The deviation of the bed shear stress direction from the main flow direction can be described by the tangent of the two components:

$$\tan\phi_\tau = \frac{\tau_{bn}}{\tau_{bs}} \tag{2.23}$$

Spiral flow intensity

Frequent use is made of descriptions for spiral flow intensity in literature. De Vriend (1976) defined a simplified prediction for a channel with a Chézy value of 60 $m^{1/2}/s$. It is based on the local curvature of the depth-averaged flow:

$$i_s \overset{\text{def}}{=} 1.67\frac{hU_s}{R_s} \tag{2.24}$$

Another method developed by De Vriend (1979) for determining the spiral flow intensity uses the integral of the absolute value of the transverse velocities. This leads to the same answers as in Equation 2.24, in case the transverse velocities are calculated using Equation 2.13:

$$i_s \overset{\text{def}}{=} 0.5\int_0^1 \left|v_n\left(\frac{z}{h}\right)\right| d\left(\frac{z}{h}\right) \tag{2.25}$$

2.4. Modelling practice

This section elaborates the current modelling practice of hydrodynamics in order to provide a background for the assessment of model results obtained in this research.

2.4.1. Model components

Models used for studying spiral flow are generally built up of three interconnected components, viz. the hydrodynamics, channel bed morphology and channel bank migration (Ottevanger, 2013). The river flow is described by the hydrodynamic component, which provides results such as the bed and bank shear stresses serving as input for the other two model components. The sediment transport can be determined based on these shear stresses, which in turn describes the bed level development. Subsequently, changes in bed and bank morphology have their impact on the flow field, closing the loop again. The computation procedure for a hydrodynamic and (bed) morphology model is shown in Figure 2.6.

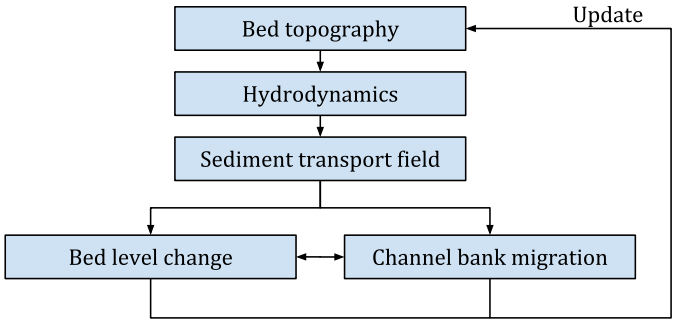

Figure 2.6: Computation steps for a hydro-morphodynamical model

This research focusses on the hydrodynamic component. The morphodynamic model components (bed level change and channel bank migration) are out of the scope of this research.

2.4.2. Solving the hydrodynamic component

The partial differential equations forming the Navier-Stokes equations have a non-linear character for flows with moderate and high Reynolds numbers. Therefore analytical solutions are difficult or impossible to find. This problem is circumvented by numerically solving the equations, which is a common approach within the field of computational fluid dynamics. Multiple numerical solution techniques are available, with different methods of resolving physics and varying degrees of computational costs. The hierarchy of available techniques is schematised by Ottevanger (2013) as shown in Figure 2.7.

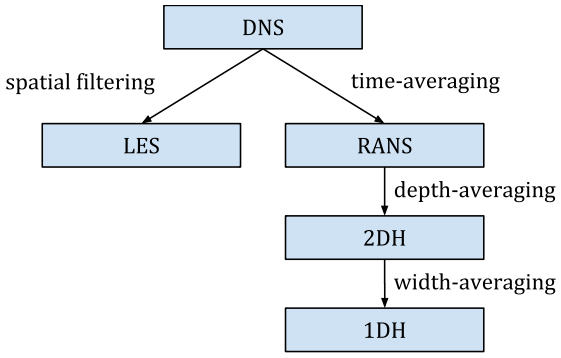

Figure 2.7: Hierarchy of hydrodynamics models (Ottevanger, 2013, modified)

Direct numerical simulation (DNS)

The hydrodynamics of open channel flow can, in theory, be simulated directly at the turbulence scale by solving the Navier-Stokes equations numerically, when the initial and boundary conditions are known. This

approach is known as Direct Numerical Simulation (DNS). However, this would require an extremely detailed grid resolution in order to be able to solve the turbulent motion down to the smallest scales of turbulence, known as the Kolmogorov micro-scales. Due to the associated extremely large demand for computational resources, this approach is only regarded to be feasible for studying the details of low-Reynolds number flows in very simple geometries. Simulation of typical hydraulic engineering problems would require vast computational power and is therefore considered to be impossible for the coming decades or centuries (Uijttewaal, 2003).

Large eddy simulation (LES)
The technique of large eddy simulation bypasses some of the problems encountered in the DNS technique by spatially filtering of smaller turbulence eddies. This leads to a significant reduction of computational resources. The large-scale motion is resolved on the numerical grid. However, the effect of the small-scale motion, which is mainly the withdrawal of energy, is generally included in the sub-grid model (Van Balen, 2010; Uijttewaal, 2003). The technique of large eddy simulations enables researchers to carry out detailed investigations on curved flow, especially for specific features which are hard to measure. Booij (2003) was one of the first applying this technique for modelling a mildly curved flume with a flat bed. He compared the results with measurements and RANS simulations, which are common in river engineering practice. Some years later, Van Balen (2010) used LES for modelling a sharply curved bend with a flat bed and compared the results with measurements conducted by Blanckaert (2009). Shortly after, Van Balen et al. (2010) also performed LES on the same flume with developed bathymetry, in comparison with measurements carried out by Blanckaert (2009). Van Sabben (2010) compared the LES with RANS model results for both of these scenarios. LES is of large added value for researching flow, especially for flow characteristics related to turbulence. However, these models are still computationally too expensive for application within engineering practice, especially for hydro-morphodynamic computations.

RANS
The procedure of Reynolds-averaging the Navier-Stokes equations is briefly explained in Section 2.3.2. A more elaborate explanation on the Boussinesq hypothesis and closure models is given in Appendix A.

Dimensionality reduction
Additional simplifications within modelling practice can be obtained by reducing the dimensionality of models. Depth-averaging a three-dimensional RANS model yields a so-called 2DH (depth-averaged) model. A next possible step is width-averaging a 2DH model, yielding a so-called 1DH model. Due to the dimensionality reduction, these models are unable to resolve three-dimensional flow phenomena, such as spiral flow. An advantage of this approach is the reduction of required computational resources by an order of magnitude per reduced dimension. Furthermore, less input data is required and the assessment of results is less laborious. The absence of three-dimensional phenomena is circumvented by including parametrisations in the model, representing the effects of three-dimensional phenomena. An important consequence is the restrictive influence of assumptions and simplifications on the reliability and area of application of parametrisations.

2.4.3. Implementation of secondary flow

Three-dimensional models
Three-dimensional models are capable of solving the main secondary flow cell. Therefore no additional parametrisations are required for including the effects of spiral flow. However, notion should be made of the method used for calculating the bed shear stress. This is based upon the near-bed flow vector found in the bottommost computational layer, as shown in Figure 2.8:

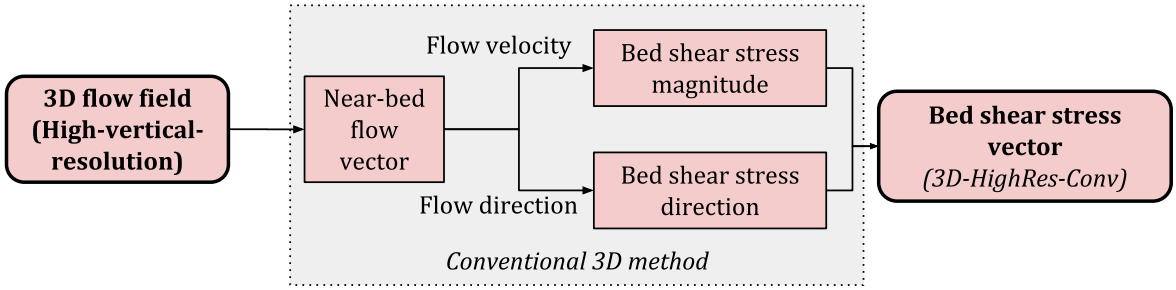

Figure 2.8: Workflow diagram of a conventional high-vertical-resolution 3D model

An issue with this approach is the dependence of the bed shear stress direction on the flow direction of the bottommost layer, which is in turn dependent on the resolution of the vertical grid. A coarser grid is therefore likely to underestimate the deviation of the bed shear stress angle. This is illustrated in Figure 2.9 showing a top view of Figure 2.1, comparing set-ups using 5 and 15 equidistant layers. One can observe a difference in the deviation of the bottommost flow vector for models with a varying resolution, as indicated by the red arrows in Figure 2.9.

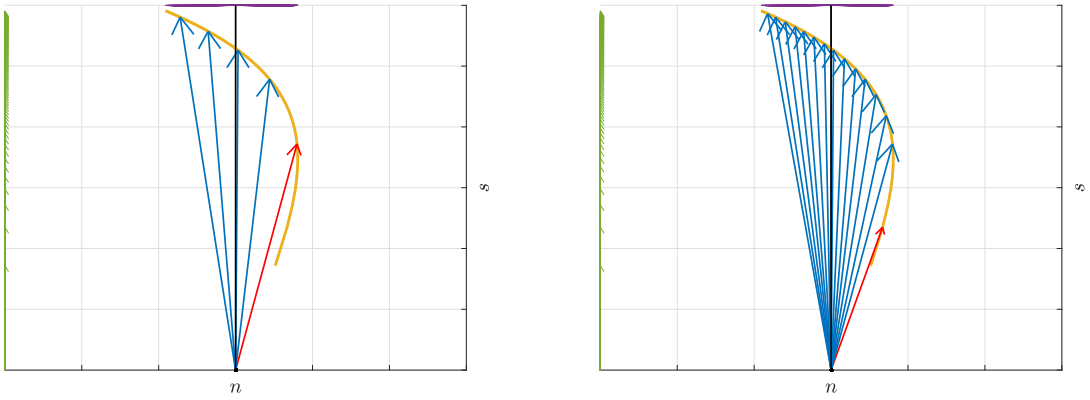

(a) 5 equidistant layers

(b) 15 equidistant layers

Figure 2.9: Top view of horizontal flow vectors in case of spiral flow

Depth-averaged models

A fundamentally different approach is required for modelling spiral flow in depth-averaged models. As stated before, depth-averaged models are inherently unable to solve three-dimensional phenomena such as spiral flow. Therefore parametrisations have been developed in order to include the effects of spiral flow in numerical models. The work of De Vriend (1976) as explained in Section 2.3 forms the foundation of many models. Ottevanger (2013) researched the implementation of spiral flow in hydrodynamic models, distinguishing the following approaches in depth-averaged models:

- Models which entirely neglect the effects of spiral flow
- Models which solely account for the influence of spiral flow on the bed shear stress, but neglect the effect of secondary flow on the depth-averaged flow field
- Models which account for the influence of spiral flow on the bed shear stress, and furthermore include the influence of additional shear stresses on the flow field, by including these in the momentum equations. The workflow of such a model is shown in Figure 2.10:

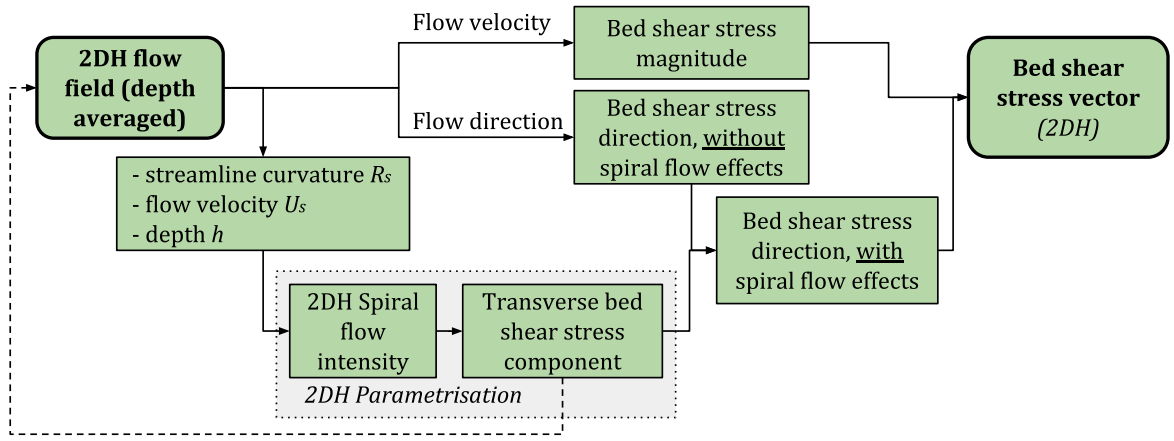

Figure 2.10: Workflow diagram of a conventional 2DH model

In this research use is made of Delft3D-Flow developed by Deltares (2017). The depth-averaged version of Delft3D uses the linear parametrisations obtained by De Vriend (1976) and further extended based on the work of Kalkwijk and Booij (1986). The Delft3D-Flow manual describes the solving procedure of the 2DH parametrisation as follows:

1. The streamline curvature $1/R_s$ is determined for each grid cell.
2. The spiral flow intensity I is calculated based on the streamline curvature $1/R_s$, flow velocity U_s and depth h (see eq. 2.24).
3. An additional advection-diffusion equation describes the generation, adaptation and decay of the spiral flow intensity in the streamwise direction, based upon the work of Kalkwijk and Booij (1986). The boundary conditions cannot be described by the user, because the secondary flow is determined locally within the model area.
4. The transverse bed shear stress component τ_{bn} is calculated based upon the effective spiral flow intensity I, using Equation 2.22.
5. Finally, the effect of additional shear stresses is included in the depth-averaged momentum equations.

An important side note is regarding this procedure is the possible influence of a large number of underlying assumptions and simplifications, as described in the previous sections. An important drawback of the procedure itself is mentioned by Ottevanger (2013). He explains that the parametrisation is derived from the flow equations at the centreline of geometries with a constant width and a fixed radius of curvature, as mentioned in Section 2.3. Delft3D extends the secondary flow parametrisation over the width of the channel by substituting local flow quantities. However, this is fundamentally incorrect, because the underlying assumptions do not hold near the banks. Another important restrictive factor in using the explained approach is the limitation of the underlying theory to mildly curved bends, as explained in Section 2.3. This leads to an overestimation of the spiral flow effects in strongly curved bends. Blanckaert and De Vriend (2003) and other researchers have developed parametrisations circumventing this problem with the use of correction factors, but this has not been implemented yet in models.

2.5. Conclusion

Spiral flow is a predominant form of secondary flow in curved open channel flow, leading to additional flow components perpendicular to the main flow. These are directed toward the inner bend in the lower part of the water column and toward the outer bend in the upper part of the water column. The most important morphodynamic consequences of spiral flow follow from a deviation of the bed shear stress towards the inner bend and the redistribution of flow momentum. The latter leads to a shift of the largest flow velocities towards the outer bend and in general higher flow velocities near the bed. As a result, the outer bank of a river is prone to erosion and at the inner bank a point bar can develop. Multiple modelling approaches can be used for describing spiral flow, of which models based upon the Reynolds-averaged Navier-Stokes equations

are prevalent in river engineering practice. These models use a strongly simplified description for turbulence leading to the need for closure models, reducing the reliability and accuracy of the model. De Vriend (1976) derived a mathematical model based upon the RANS equations enabling the description of spiral flow characteristics. These descriptions allow the inclusion of the effects of spiral flow in depth-averaged models, which are not able to capture three-dimensional phenomena such as spiral flow. However, many assumptions and simplifications underlie the model, potentially limiting the area of applicability and reliability of the obtained descriptions. On the contrary, three-dimensional models are able to capture these phenomena and do not require the use of parametrisations. However, these models are generally computationally an order of magnitude more expensive. Furthermore, the accuracy of the bed shear stress direction is dependent on the vertical resolution of a three-dimensional model. However, this problem in three-dimensional models can be circumvented by using descriptions which relate the bed shear stress to the spiral flow intensity, which allows a determination independent of the applied resolution. These descriptions are also obtained by De Vriend (1976), but never used in three-dimensional models.

3

Methodology

This chapter presents the new methodology developed in this research for modelling spiral flow with a low-vertical-resolution three-dimensional model. Section 3.1 describes the new methodology in general terms. Subsequently, Section 3.2 presents an overview of the new methodology in comparison with conventional three-dimensional and depth-averaged methodologies. A distinction is drawn between three distinct research components, namely the flow field, spiral flow intensity and bed shear stress. Section 3.3 first describes how the flow field is compared for each of the methodologies. Subsequently, it elaborates on the functioning of the new methodology in comparison with conventional methodologies, on the basis of the computation methods for the spiral flow intensity and bed shear stress.

3.1. New methodology

The workflow of the new methodology is presented in Figure 3.1, in a similar way as the presentation of conventional three-dimensional and depth-averaged models in Section 2.4.3:

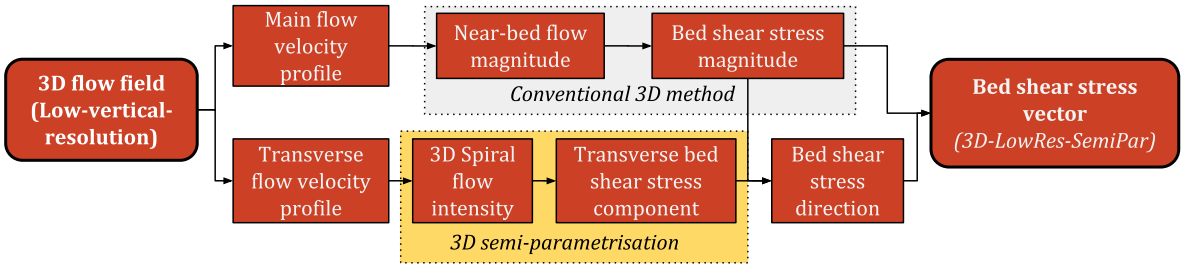

Figure 3.1: Workflow diagram of the new methodology

The first step is the determination of the main flow direction, using the same approach as De Vriend (1978). This is defined as the flow component in the direction of the depth-averaged flow, also called the streamwise direction (s). The main flow direction not necessarily coincides with the direction of the channel axis (Φ), and might vary over the width of a geometry. The main flow velocity profile is the vertical distribution of the streamwise component of the horizontal flow vectors. Subsequently, the light-grey box describes the procedure of determining the bed shear stress magnitude in streamwise direction. This is analogous to the conventional approach for three-dimensional models, as seen in Figure 2.8. The main flow velocity profile is shown in green in Figure 3.2:

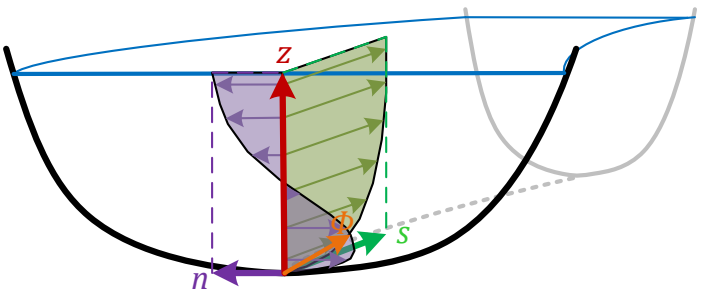

Figure 3.2: Main and transverse velocity profiles

Secondly, the transverse flow velocity profile is determined. This profile is the vertical distribution of the horizontal flow vector components oriented perpendicular (n) to the main flow direction, indicated in purple in Figure 3.2. This means that the depth-averaged transverse flow is equal to zero by definition. The transverse flow velocity profile provides insight into the characteristics of the spiral flow. Subsequently, the transverse flow velocity profile serves as input for the so-called *3D semi-parametrisation*, indicated in yellow in Figure 3.1. This parametrisation is built up of two components, one for determining the spiral flow intensity and the second for determining the transverse bed shear stress component. Multiple methods were developed for determining the spiral flow intensity. A more extensive explanation is given in Section 3.3.2. The 3D semi-parametrisation is expected to be much more accurate than the 2DH parametrisation which is presented in Figure 2.10 in Section 2.4.3. This is due to the fact that it is based on the actual transverse velocity profile, rather than general parameters representing the streamline curvature, depth and streamwise velocity. The second component of the 3D semi-parametrisation is the determination of the transverse bed shear stress component based on the spiral flow intensity, which is similar to the current approach in 2DH models. This allows the calculation of the bed shear stress direction, and subsequently the bed shear stress vector.

Before the start of the research, a Delft3D FM research model was already available within Deltares also aiming to determine the bed shear stress directions more accurately in low-vertical-resolution models, developed by Willem Ottevanger and Mohamed Nabi. It also made use of the spiral flow intensity, however, a different method was chosen for determining this parameter, based on a curve-fitting approach. Although this approach can be considered to be analogous to the methodology developed in this report, it did not yield consistent results. The calculated bed shear stress directions turned out to depend on the vertical resolution. Therefore during this research a new approach was developed for calculating the spiral flow intensity, partly based on the available research model and partly based upon the work of De Vriend (1976).

3.2. Methodology comparison

The performance of the new methodology using a low-vertical-resolution 3D model is compared with a conventional 3D and 2DH model. Furthermore, a comparison is made with measurement data, as far as available. A distinction is made between three research components, namely the flow field, spiral flow intensity and bed shear stress. An overview is given in Figure 3.3:

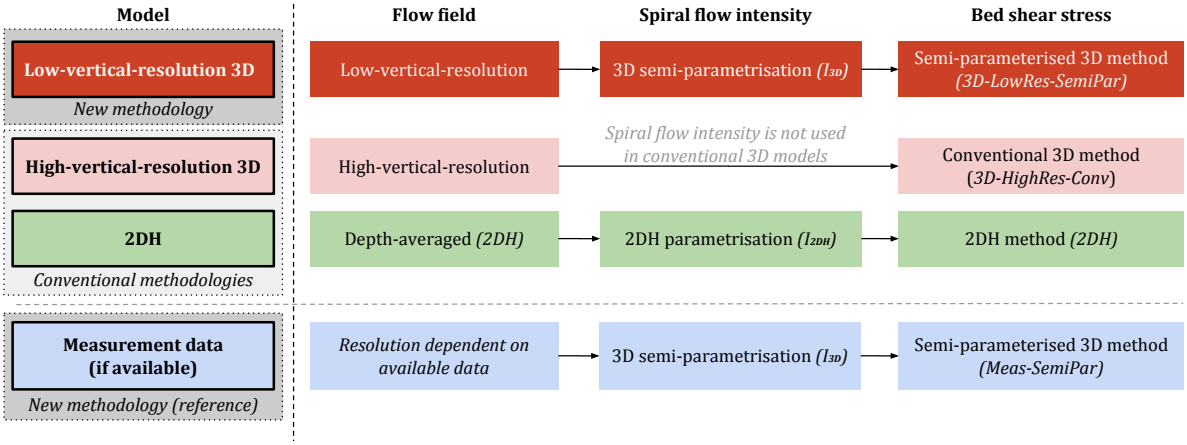

Figure 3.3: Overview of methodologies of different models

The first column distinguishes the different models which are compared. Each of the models provides a different flow field due to the various computational methods. The only difference between low and high-vertical-resolution 3D models is the vertical resolution. The flow field is the first research component, as found in the second column. The second and third research components are the spiral flow intensity and bed shear stress, indicated in the third and fourth column respectively. This distinction is made because each the methodologies uses a different approach for determining these parameters. Table 3.1 gives an overview of the new methodology using a low-vertical-resolution 3D model in comparison with conventional 2DH and 3D methodologies. References are made to the underlying formulas, presented in Section 3.3

Methodology / *Parameter*	New methodology (*3D-LowRes-SemiPar*)	Conventional 3D methodology (*3D-HighRes-Conv*)	Conventional 2DH methodology
Spiral flow intensity (I)	3D approach based on the transverse velocity profile v_n (De Vriend, 1979; I_{3D} determined by eqs. 3.5 and 3.6)	*not calculated separately*	2DH approach (De Vriend, 1976; eq. 3.1, $I_{2D} = \frac{hU_s}{R_s}$)
Streamwise bed shear stress component (τ_{bs})	Based on the streamwise flow velocity in the bottommost layer (v_{s_1}, eq. 3.13)	*not calculated separately*	Based on the depth-averaged streamwise flow velocity (U_s, eq. 3.10)
Transverse bed shear stress component (τ_{bn})	Calculated with the 2D equation of De Vriend (1976) (eq. 3.11)	*not calculated separately*	Calculated with the 2D equation of De Vriend (1976) (eq. 3.16)
Bed shear stress angle deviation (ϕ_τ)	$\tan\phi_\tau = \frac{\tau_{bn}}{\tau_{bs}}$	Based on flow direction in bottommost layer (v_1)	$\tan\phi_\tau = \frac{\tau_{bn}}{\tau_{bs}}$
Bed shear stress magnitude (τ_b)	$\tau_b = \sqrt{\tau_{bn}^2 + \tau_{bs}^2}$	Based on flow magnitude of bottommost layer (v_1)	$\tau_b = \sqrt{\tau_{bn}^2 + \tau_{bs}^2}$
Additional descriptions	*not applicable*	*not applicable*	Distribution functions in streamwise and transverse directions

Table 3.1: Overview of methods for determining the bed shear stress

3.3. Research components

This section gives a more detailed description of the research components presented in Figure 3.3 in Section 3.2. A comparison with conventional methodologies is made where relevant.

3.3.1. Flow field

Evaluating the hydrodynamics of the low- and high-vertical resolution 3D models and 2DH model provides an answer to the first research question about the performance of conventional methodologies, and forms the basis for the new methodology.

General water level and velocity development
The roughness and downstream water level boundary are chosen such that the water levels and mean velocities agree as much as possible with the measurements. The general flow field of the 2DH and low-vertical-resolution 3D model results are analysed and compared with measurements, insofar measurement data is available. Among other things, this gives insight in the consequence of the inability of 2DH models to reproduce the redistribution of streamwise momentum induced by spiral flow. Furthermore, it gives insight in the performance of three-dimensional models regarding the aforementioned redistribution.

Streamwise and transverse development of velocity profiles
The more general comparison as described above is followed by a detailed research into specific features, by analysing the velocity profiles of three-dimensional models and measurement data in more detail. This gives more insight in the consequences of the inability of three-dimensional RANS models to represent turbulent features, such as the outer bank cell. Furthermore, it gives insight into the performance of three-dimensional models to capture the distortion of the velocity profiles along the bend. This requires the decomposition of the combined velocity profile into a streamwise and transverse part, as described in Section 3.1. There is no information about the velocity profiles in a depth-averaged model. However, Delft3D implicitly assumes a logarithmic main flow profile and the normalized secondary flow distribution based upon the work of De Vriend (1976), as depicted in Figure 2.5 in Section 2.3. These profiles are included in the results as a reference at locations with fully developed secondary flow, which is one of the assumptions underlying these profiles.

3.3.2. Spiral flow intensity
The new methodology using a low-vertical-resolution 3D model uses a different method for calculating the spiral flow intensity than the conventional 2DH method. This section presents the 3D semi-parametrisation used in the new methodology after recalling the conventional 2DH parametrisation. The spiral flow intensity is not only a measure of the spiral flow itself. It also forms the basis for determining the transverse bed shear stress component in both the 3D semi-parametrisation and 2DH parametrisation. This method is not used in conventional 3D models, as indicated in Figure 3.3.

According to De Vriend (1976), both parametrisations should theoretically yield the same spiral flow intensities, i.e. $I_{2D} = I_{3D}$. However, in reality, this is not necessarily the case because of two reasons. Firstly, a 3D model is able to capture more processes than a 2DH model. This leads to differences in the computed flow fields of the distinct models, hence leading to differences in the computed intensities. The second cause is due to the different methods for computing the spiral flow intensity, which are described in this section. In theory, these methods should yield the same result for idealized cases complying with the assumptions underlying the derivations of De Vriend (1976). This would be the case when the streamwise and transverse velocity profiles found in the 3D model results agree with Figure 2.5 in Section 2.3. However, this is not to be expected in reality due to the large number of assumptions underlying the velocity profiles of Figure 2.5.

2DH parametrisation
The 2DH method is based on a strongly simplified predictive description for the spiral flow intensity given by De Vriend (1979):

$$I_{2D} \overset{\text{def}}{=} \frac{hU_s}{R} \tag{3.1}$$

This description is used in multiple 2DH models, among which the 2DH version of Delft3D. It only applies to fully developed flow and neglects the interaction between the main and secondary flow. Additional descriptions are required describing for the development, adaptation and decay of the intensity along the flume, which are based on the work of Kalkwijk and Booij (1986).

3D semi-parametrisation
The starting point of the method is based upon the derivations of De Vriend (1976). The transverse velocities can be calculated by Equation 2.13 as found in Section 2.3, recalled by Equation 3.2:

$$v_n = \frac{hU_s}{\kappa^2 R} f_n\left(\frac{z}{h}, \alpha\right) \tag{3.2}$$

The next step is inserting Equation 3.1 in Equation 3.2, yielding Equation 3.3 describing the transverse flow velocity:

$$v_n\left(\frac{z}{h}\right) = I_{2D}\frac{1}{\kappa^2} f_n\left(\frac{z}{h}\right) \tag{3.3}$$

Rewriting Equation 3.3 yields Equation 3.4 (recalling the theoretical agreement between I_{2D} and I_{3D}):

$$I_{k,3D} = \kappa^2 \frac{v_n\left(\frac{z}{h}\right)}{f_n\left(\frac{z}{h}\right)} \tag{3.4}$$

Equation 3.4 shows how the spiral flow intensity I_{3D} can be computed based on any point k in the transverse flow profile v_n. Furthermore, the Von Kármán constant κ and the normalized transverse flow velocity profile f_n are required. The latter depends on the roughness, as seen in Figure 2.5 in Section 2.3. The 3D semi-parametrisation for the spiral flow intensity I (eq. 3.4) is expected to be more appropriate than the 2D parametrisation (eq. 3.1), due to the fact that it is based upon the actual transverse velocity profiles. Furthermore, this expression does not require additional descriptions to account for the streamwise development, adaptation and decay of the spiral flow. Additionally, 3D models account for the interaction between the main and secondary flow. Hence, the effect of this interaction is automatically included in the 3D semi-parametrisation.

Based on Equation 3.4, the spiral flow intensity can be calculated locally for any point k in the transverse velocity profile v_n, for example the near-bed vector. The intensity based on the entire profile can be described by Equation 3.5

$$I_{3D} = \frac{1}{N}\sum_{k=1}^{N} I_{k,3D} \tag{3.5}$$

In which N is the total number of velocity points which are used for determining the spiral flow intensity. This is illustrated in Figure 3.4, in which Figure 3.4a makes use of all five velocity points, and Figure 3.4b only the bottommost point:

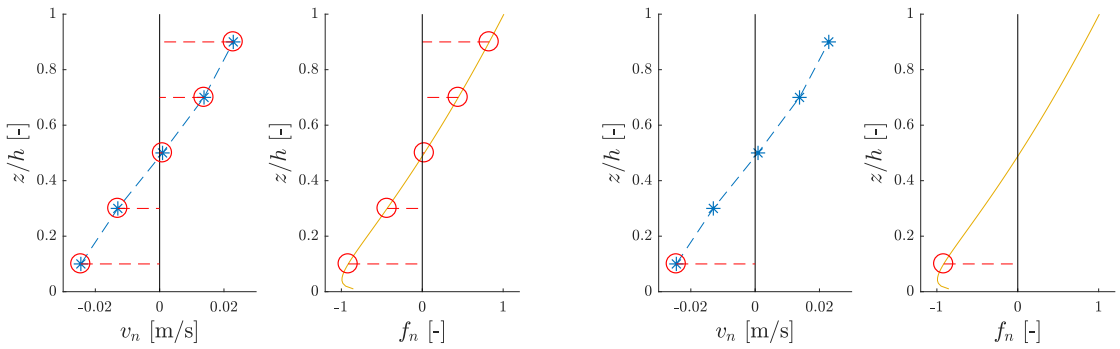

(a) All velocity points

(b) Single velocity point

Figure 3.4: Spiral flow calculation method based using Equation 3.5

However, this calculation method leads to problems near $z/h = 0.5$. In that case, the denominator f_n of Equation 3.4 takes a value of 0. A refinement of Equations 3.4 and 3.5 circumventing this problem can be obtained by basing the spiral flow intensity upon the integrated transverse profile, leading to Equation 3.6:

$$I_{3D} = \text{sign}(v_{n,1})\kappa^2 \frac{\int_0^1 \left|v_n\left(\frac{z}{h}\right)\right| d\left(\frac{z}{h}\right)}{\int_{z_0/h}^1 \left|f_n\left(\frac{z}{h}\right)\right| d\left(\frac{z}{h}\right)} \tag{3.6}$$

In which $\text{sign}(v_{n,1})$ describes the sign of the bottommost transverse velocity vector, as this information disappears when taking the absolute value of the transverse velocity profiles. The integral of the denominator can be calculated based on the descriptions of De Vriend (1976) indicated in Figure 2.5 in Section 2.3.

Equation 3.6 is based on the integral of the vertical flow profile. One could calculate the spiral flow velocity based on the absolute integral of the profile from the bed to the surface, as indicated in Figure 3.5a. Another

method is taking only the bottommost part of the profile as seen in Figure 3.5b, because this part is the most important for calculating the bed shear stresses. This might especially be a solution for flow profiles which deviate strongly from the normalized f_n profile as depicted. It can be considered as a further refinement of the methodology.

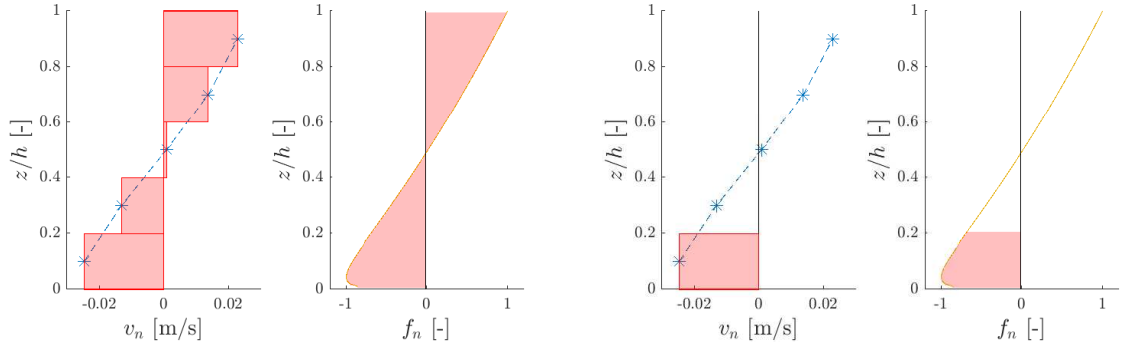

(a) Integral of entire profile (calculation method A)

(b) Integral of bottommost part (calculation method B)

Figure 3.5: Spiral flow calculation method using Equation 3.6

The two calculation methods as presented in Figure 3.5 are schematically shown in Figure 3.6, which is an expansion of Figure 3.1 as presented at the beginning of this chapter.

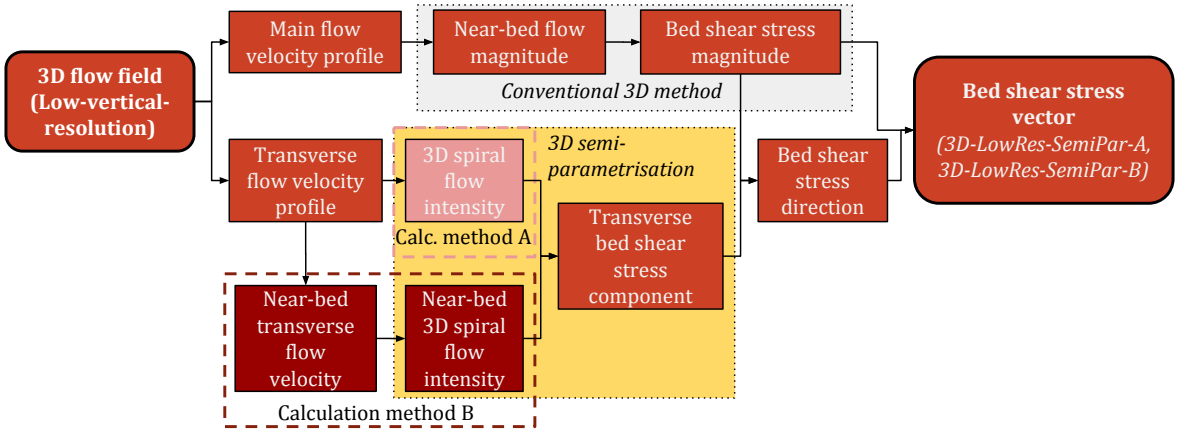

Figure 3.6: Workflow diagram of the new methodology

Validation with descriptions of De Vriend (1979)

This paragraph validates the obtained description for the spiral flow intensity (eq. 3.6) with the description obtained by De Vriend (1979) in case of a Chézy value of 60 $m^{1/2}/s$, which De Vriend (1979) supplemented by a scaling factor:

$$i_s \overset{\text{def}}{=} 1.67\frac{hU_s}{R} = 0.5\int_0^1 \left|v_n\left(\frac{z}{h}\right)\right| d\left(\frac{z}{h}\right) \tag{3.7}$$

When taking away the scaling factor, the following descriptions are obtained:

$$i_{s,2} \overset{\text{def}}{=} \frac{hU_s}{R} = 0.3\int_0^1 \left|v_n\left(\frac{z}{h}\right)\right| d\left(\frac{z}{h}\right) \tag{3.8}$$

Recalling Equation 3.6, one can compute that the denominator takes a value of 0.54 for a Chézy value of 60 $m^{1/2}/s$:

$$I_{3D} = \text{sign}(v_{n,1})\kappa^2 \frac{\int_0^1 \left|v_n\left(\frac{z}{h}\right)\right| d\left(\frac{z}{h}\right)}{\int_{z_0/h}^1 \left|f_n\left(\frac{z}{h}\right)\right| d\left(\frac{z}{h}\right)} = \text{sign}(v_{n,1}) * 0.3\int_0^1 \left|v_n\left(\frac{z}{h}\right)\right| d\left(\frac{z}{h}\right) \tag{3.9}$$

This is in agreement with Equation 3.8.

3.3.3. Bed shear stress

The descriptions for the spiral flow intensity form the basis for computing the bed shear stress direction for the 2DH method and semi-parametrised 3D method. The 2DH methodology is repeated briefly because it forms the basis for the semi-parametrised 3D method presented in this research. The new methodology allows computation of the bed shear stress direction independent of the vertical resolution of the flow field. The conventional 3D method is not treated in this section, because it does not make use of the spiral flow intensity. The functioning of this method is explained in Section 2.4.3

2DH method

The bed shear stress magnitude is calculated assuming the quadratic friction law. It can be calculated based on the depth-averaged velocity as indicated in Equation 3.10 (recalling Equation 2.21 in Section 2.3):

$$\tau_{bs,2D} = \frac{\rho g}{C} U_s^2 \tag{3.10}$$

The transverse component of the bed shear stress (τ_{bn}) can be calculated using Equation 3.11 using the spiral flow intensity obtained from Equation 3.1, following the method of De Vriend (1976) as described in Section 2.3.

$$\tau_{bn,2D} = 2\rho\alpha^2(1-\alpha)U_s I_{2D} \tag{3.11}$$

In which α is a friction parameter which is expressed as follows, in which κ represents the Von Kármán constant:

$$\alpha = \frac{\sqrt{g}}{\kappa C} \tag{3.12}$$

Semi-parametrised 3D method

The approach used for determining the bed shear stress magnitude of 3D models is based on the approach described in the Delft3D-FM manual of Deltares (2017). It is largely comparable to the method used for depth-averaged models. The main difference is that the streamwise shear stress is based on the flow velocity in the bottommost layer, rather than the depth-averaged velocity. This approach is expected to be more accurate, especially when the streamwise flow velocity profile deviates strongly from the logarithmic profile. The bed shear stress magnitude is calculated as follows:

$$\tau_{bs,3D} = \rho v_s^* \left| v_s^* \right| \tag{3.13}$$

The shear velocity v_s^* is calculated as follows, based on the Delft3D FM manual (Deltares, 2017):

$$v_s^* = \frac{v_{s,1}\kappa}{\ln\left(\frac{\Delta z_b + \mu z_0}{e z_0}\right)} \tag{3.14}$$

In which $v_{s,1}$ is the flow velocity in the bottommost computational point, Δz_b represents the distance from this point to the bed. The variable μ is a constant set equal to 9. The variable z_0 represents the bed roughness height, calculated as follows:

$$z_0 = \frac{h}{e^{1+\frac{\kappa C}{\sqrt{g}}} - e} \tag{3.15}$$

Subsequently, the transverse component of the bed shear stress (τ_{bn}) is computed similarly as in the 2DH method given by Equation 3.11. In case of adopting the three-dimensional approach, Equation 3.16 can be described using the 3D spiral flow definition given by Equation 3.6:

$$\tau_{bn,3D} = 2\rho\alpha^2(1-\alpha)U_s I_{3D} \tag{3.16}$$

The relation is based upon the first order approximation of De Vriend (1976) which is based on many assumptions and simplifications. However, the strongly simplified 2DH determination of the spiral flow intensity is bypassed by the 3D semi-parametrised method. This is expected to lead to a significant improvement of the 3D semi-parametrised method in comparison with the conventional 2DH method.

Calculation of bed shear stress vector

The angular deviation of the bed shear stress deviation is indicated by ϕ_τ. It represents the deviation between the bed shear stress direction θ_τ and the local main flow direction θ_{U_s}. It is calculated by Equation 3.17:

$$\tan\phi_\tau = \frac{\tau_{bn}}{\tau_{bs}} \tag{3.17}$$

The bed shear stress magnitudes and directions obtained with the 3D semi-parametrised method are compared with the conventional 3D and 2DH methods. The conventional approach for three-dimensional models is setting the bed shear stress direction equal to the flow direction of the bottommost layer. Figure 3.7 gives an overview of the relevant directions and angles. The directions can be defined relative to the local geometry or a fixed reference system. This in not of main importance, due to the focus on angular deviations in this research.

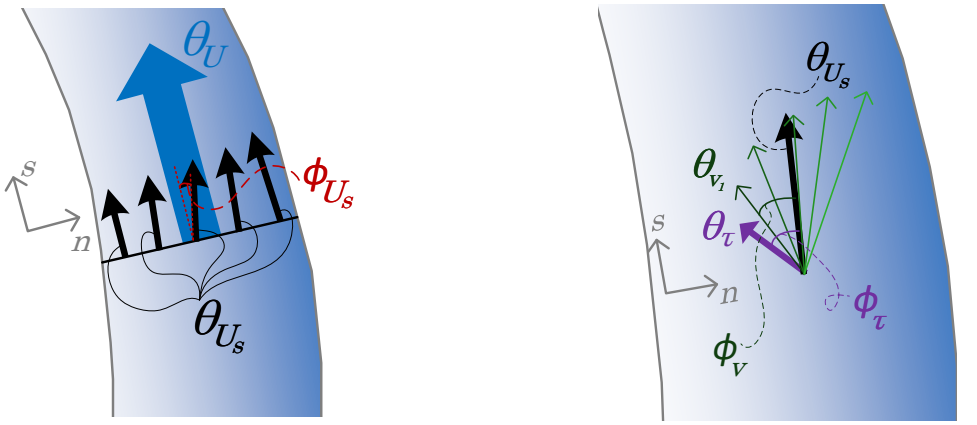

(a) Local and cross-section averaged main flow directions

(b) Flow and bed shear stress directions

Figure 3.7: Overview of relevant flow and bed shear stress directions

In Figure 3.7a one can observe:

- θ_U describes the cross-section averaged main flow direction, which does not necessarily run parallel with the channel centreline.
- θ_{U_s} describes the direction of the local depth-averaged flow, defined as the main flow direction. When averaging these vectors over the width, one obtains the aforementioned direction θ_U. The angular deviation of θ_{U_s} from θ_U is indicated in red by ϕ_{U_s}.

One can observe a detailed representation of one of the main flow vectors indicated by θ_{U_s} in Figure 3.7b, in which:

- θ_{v_1} indicates the direction of the bottommost velocity vector. The angular deviation of θ_{v_1} from θ_{U_s} is indicated by ϕ_v. The similarly shaped vectors ranging from dark to light green represent five velocity vectors ranging from the bed to the free surface. When depth-averaging these vectors, one obtains θ_{U_s}.
- θ_τ indicates the direction of the bed shear stress. The angular deviation of θ_τ from θ_{U_s} is indicated in purple by ϕ_τ. This angular deviation is generally larger than ϕ_v.

The 3D semi-parametrised method provides a new description for determining ϕ_τ, rather than equating it with ϕ_v as applied in conventional 3D methods. The results of the 3D semi-parametrised method are verified by a conventional 3D method with a very high level of vertical detail, which enables an accurate calculation of the flow direction and magnitude of the bottommost layer, which is very close to bed. Within the context of this research, the assumption is made that this is the most accurate method for calculating the bed shear stress direction.

4

Modelling approach

The chapter presents the modelling approach used for applying and validating the new methodology as presented in Chapter 3. Firstly, Section 4.1 gives information about the modelling software used in this research. Subsequently, Section 4.2 describes the three distinct cases modelled within this research.

4.1. Modelling software

4.1.1. Delft3D

This research makes use of the hydrodynamic simulation module D-Flow FM within the Delft3D Flexible Mesh Suite, further referred to as D3D-FM. D3D-FM allows modelling flow, waves, water quality and ecology of coastal, riverine and estuarine areas (Deltares, 2017). It is suitable for this research due to its ability to conduct both depth-averaged and three-dimensional hydrodynamic calculations. Furthermore, it also allows morphological modelling, however, this option is not used within this research. D3D-FM is the successor of D3D-4 in which only structured curvilinear grids could be used. It is able to handle multiple grids types giving the user more freedom in defining geometries. The latter makes D3D-FM more suitable than D3D-4 for modelling more random geometries, fitting the aim of this research of modelling more arbitrary geometries. Both the 2DH- and 3D-functionality of D3D-FM are used in this research. The implementation of spiral flow is discussed in Section 2.4. All model runs were carried out using a σ-grid which fits the chosen number of layers within the vertical boundaries. In depth-averaged models a σ-grid is required for enabling the secondary flow parametrisation. Furthermore, a σ-grid allows the calculation of the secondary flow profile at the same level of detail for any depth, contrary to a Z-grid with a fixed sequence of layers. Furthermore use is made of the $k-\epsilon$ turbulence model, which is a widely used in modelling practice. Nevertheless, there are some shortcomings which can be of relevance for this research, as described in Appendix A. According to Rodi (2017), the model is known to produce unsatisfactory results in situations at which the anisotrophy of turbulence and streamline curvature play a large role.

4.1.2. Assumptions and approximations

In Delft3D the non-linear shallow water equations are solved using multiple assumptions and approximations. The section describes relevant assumptions within the context of this research, based on the Delft3D manual written by Deltares (2017):

- The shallow water assumption requires the depth to be much smaller than the horizontal length scales. This enables simplification of the vertical momentum balance, leading to the hydrostatic pressure relation. This means that the vertical accelerations are assumed to be negligible compared with the gravitational acceleration.
- The model assumes a no-slip boundary condition at the bed. This enables the application of a quadratic friction law for the bed shear stress.
- The fluid is assumed to be incompressible.
- The flow equations are Reynolds-averaged which introduces the Reynolds stresses. The Boussinesq hypothesis is applied and closure models are used the calculate these Reynolds stresses (Appendix A).

- The production of turbulence within the closure models is solely based on the vertical gradients of the horizontal component of the flow velocity, which is considered to be justified when the shallow water assumption applies.
- The $k-\epsilon$ model requires transport equations to be solved for the turbulent kinetic energy k and energy dissipation ϵ. The underlying assumptions are that the production, buoyancy and dissipation terms are dominant, and furthermore, the shallow water assumption is applied. The boundary condition applied at the bed is a local equilibrium of production and dissipation of kinetic energy. The kinetic energy is set to zero at the surface.

4.1.3. General validation

The 3D-functionality of D3D-FM has not been validated entirely and is therefore still a beta-functionality. In this research the 3D-cases have been validated using predecessor D3D-4. At first, D3D-FM showed inconsistent results with a varying number of layers, which appeared to be related to default background coefficients for the horizontal viscosity and diffusivity. The problem was solved by disabling these coefficients, leading to consistent results and good correspondence with measurement data. Validation runs in predecessor D3D-4 yielded results corresponding with these of the D3D-FM model without the background coefficients.

Efforts were made to research the influence of the hydrostatic pressure assumption in 3D computations by using a Z-grid in D3D-4, which allows non-hydrostatic computations. However, this resulted in erroneous behaviour of the model, whereas no problems were encountered using a σ-grid in D3D-4. After some efforts no time was left within the context of this research to find out the reason of the error.

4.1.4. Implementation of new methodology

The starting point of the new methodology is formed by a low-vertical-resolution 3D model in D3D-FM, i.e. a 3D model with a limited number of layers. Only equidistant layers were used within the context of this research. The next step is extracting the *NetCDF* data file in MATLAB. Subsequently, the new methodology as presented in Chapter 3 is applied to the model data by post-processing the flow velocity data in MATLAB. This is compared with the outcomes of conventional high-vertical-resolution 3D and 2DH models. This method of implementation is sufficient to give a proof of concept, by comparing the computed bed shear stress vectors. However, the methodology is not implemented in the Fortran code of Delft3D. As a consequence, it is not possible to conduct hydro-morphodynamics computations. Therefore, it is impossible to assess the performance of the new methodology in simulating the morphodynamic behaviour within the context of this research. This would require implementation of the new methodology in the Fortran code of Delft3D.

4.2. Geometries and model set-up

The performance of the new methodology in comparison with the conventional methodologies is tested on multiple geometries. This section presents the geometries selected for the research. The goal of the research was to compare the model performance for both idealized and more complex geometries, and apply the new methodology as presented in Chapter 3 on each of the cases. The first two cases are based upon simplified flume experiments of which measurement data is available. Case 3 is based on a bend in the Waal river in the Netherlands, of which no measurement data was available.

4.2.1. Case 1: Mildly curved circular U-bend, rectangular cross-section

General

The first case can be considered as a relatively simple geometry which forms the starting point of the research. It is a reproduction of a flume used at the Laboratory of Fluid Mechanics (LFM) at the TU Delft in the 1980s. The main parameters and geometry of this flume can be observed in Figure 4.1 and Table 4.1. This geometry is chosen for the first case because of to the following reasons:

1. The relative simplicity of the geometry, allowing easy modelling and yielding predictable and explainable flow behaviour.
2. The availability of extensive measurement data obtained by Blokland (1985) and LES datasets computed by Van Balen (2010) and Booij (2003).
3. The elaborate descriptions of Blokland (1985) on the flow patterns found during the measurements.

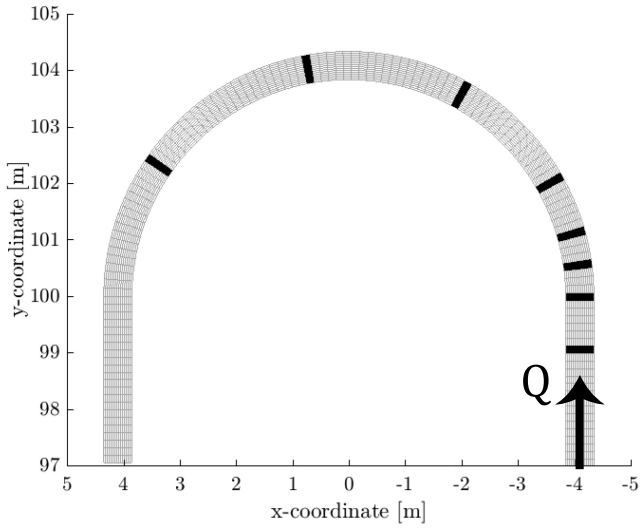

Figure 4.1: Case 1, computational grid. The inflow is located at the bottom right, the outflow at the bottom left. The black marks indicate the sections of which measurement data is available.

Parameter		Value	
discharge	Q	0.0064	m^3/s
mean flow velocity	U	0.26	m/s
average depth	h	0.05	m
width	B	0.5	m
radius of curvature	R_c	4.1	m
curvature ratio	B/R	0.12	
depth to width ratio	h/B	0.1	
Reynolds number	Re	$12 * 10^3$	

Table 4.1: Case 1, physical parameters

Measurement data

This research makes use of extensive measurements carried out in the context of the graduation thesis of Blokland (1985). His work was aimed at obtaining more insight in the turbulence structure of flow in a curved channel. Measurements were carried out using the technique of Laser Doppler Velocimetry (LDV). The measurement dataset from Blokland (1985) contains velocities in streamwise, transverse and vertical direction and all normal and Reynolds stresses. The measurements were conducted at 8 cross sections: -1 m (just before the circular section), 0°, 7.5°, 15°, 29°, 60°, 100° and 145°, all indicated in Figure 4.1. No measurements were executed in areas with decaying spiral flow. For each cross-section Blokland (1985) measured at 11 locations unequally distributed over the width, somewhat denser near the walls and somewhat sparser near the channel centreline. Each location contains about 11 measurements over depth, distributed denser near the bed and sparser near the water surface. Furthermore, a detailed LES dataset is available, measured at the same locations but with a denser distribution of measurements points over depth.

Modelling set-up

The details of the computational grid can be found in Table 4.2 and the relevant modelling parameters are listed in Table 4.3. The downstream water level boundary condition and wall roughness are calibrated such that the overall mean velocities and water levels are in agreement with the measurements. The same boundary conditions have been used for the 2DH and 3D models. The results can be found in Figure E.2 in Appendix E.1.2.

Parameter	Value
Grid cell number in s-direction	136
Average grid cell length (s-direction)	0.133 m
Grid cell number in n-direction	15
Average grid cell width (n-direction)	0.033 m
Number of layers	[1,50]
Layer thickness (z-direction)	$[0.02h\ ,\ h]$

Table 4.2: Case 1, grid parameters

Parameter		Value
Chezy roughness	C	60 $m^{1/2}/s$
Nikuradse side walls roughness	k_s	0.00026 m (partial slip)
Upstream discharge boundary cond.	$Q_{upstream}$	0.0064 m^3/s
Downstream water level boundary cond.	$h_{downstream}$	0.0465 m
Turbulence model		$k-\epsilon$

Table 4.3: Case 1, modelling parameters

4.2.2. Case 2: Mildly curved circular 90° bend, developed morphology

General

Case 2 is a mildly curved bend which only differs in size and bed topography from the first case. Furthermore, it is limited to 90° instead of 180°. The curvature is as well equal to Case 1, however, the depth to width ratio is much smaller. The geometry used in Delft3D is based upon a flume used at the Delft Hydraulics Laboratory (currently Deltares) in the late 1970s. De Vriend and Koch (1978) have carried out several experiments, initially using a rectangular cross-section and later a schematised developed bed topography. For this case, only use was made of the measurements of the developed bed topography. Unfortunately, only limited data was available. In spite of the lack of data the choice was made for this case, because it allows an investigation on the influence of the bed topography, which is the main difference with Case 1 besides the much smaller depth to width ratio. The geometry, bed topography and main parameters of this case can be observed in Figures 4.2 and 4.3 and Table 4.4.

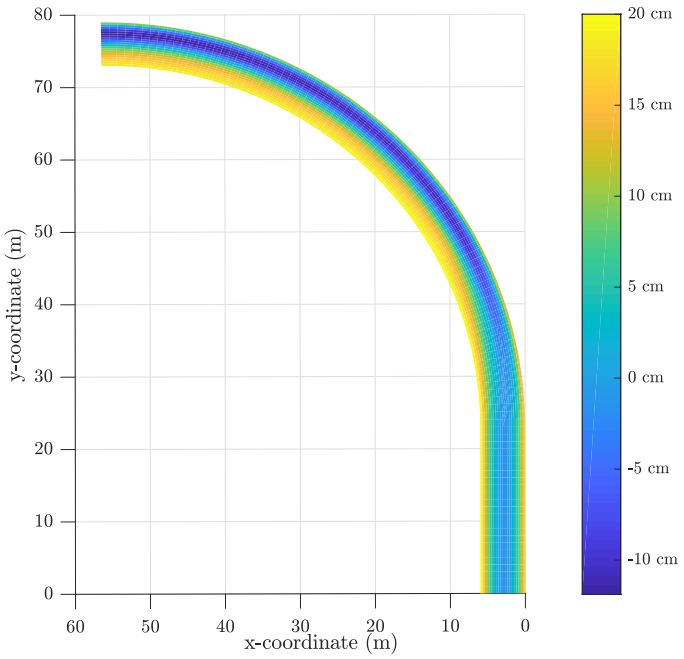

Figure 4.2: Geometry and bed topography of the DHL flume experiment

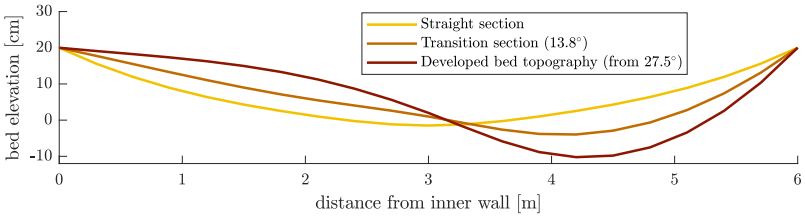

Figure 4.3: Case 2, bed levels throughout the geometry

Parameter		Value	
discharge	Q	0.463	m^3/s
mean flow velocity	U	0.4	m/s
average depth	h	[0.05,0.4]	m
width	B	6	m
Channel slope	i_s	$3 * 10^{-4}$	m (from 27.5° onward)
radius of curvature	R_c	50	m
curvature ratio	B/R	0.12	
depth to width ratio	h/B	0.04	
Reynolds number	Re	$1 * 10^5$	

Table 4.4: Case 2, physical parameters

Measurement data

De Vriend and Koch (1978) made use of a current-velocity/direction meter built up out of a miniature propeller and vane, which is an older and less accurate technique as used by Blokland (1985). Multiple measurements were conducted in the straight section and at six locations equally distributed over the bend, with an angle of 13.8° in between each pair. De Vriend and Koch (1978) measured at 13 locations equally distributed over the width of each cross-section . Unfortunately, it was impossible in the context of this research to get access to the raw measurement data. Only the report was available containing information limited to depth averaged velocities U_s and water levels h. Furthermore, the spiral flow intensities I were included, computed based on the measured transverse velocity profiles. No detailed data was available about the exact distribution of flow over the vertical, in contrast to Case 1. Furthermore, the bed topography had to be defined manually based on information of Figure 4.3.

Modelling set-up

Table 4.5 shows the details of the computational grid and Table 4.6 shows the relevant modelling parameters. Same as for Case 1, the downstream water level boundary condition and wall roughness are chosen such that the cross-sectional averaged velocities and water levels are in agreement with the measured quantities. The results after calibration can be found in Figure E.16 in Appendix E.2.2. The maximum deviation of the water levels and velocities of the 2D and 3D model results from the measurements remain limited to 4%, as can be observed in Figure E.2 in Appendix E.1.2. Manning's equation was chosen for describing the bed roughness, in order to account for the varying flow velocities due to the varying bed topography. The average roughness over the entire grid is about $C = 60\ m^{1/2}/s$.

Parameter	Value
Grid cell number in s-direction	102
Average grid cell length (s-direction)	1 m
Grid cell number in n-direction	20
Average grid cell width (n-direction)	0.3 m
Number of layers	[1,30]
Layer thickness (z-direction)	[$0.033h$, h]

Table 4.5: Case 2, grid parameters

Parameter		Value	
Manning friction coefficient	n	0.0120	s/m$^{1/3}$
Nikuradse side walls roughness	k_s	0.00026	m (partial slip)
Upstream discharge boundary cond.	$Q_{upstream}$	0.463	m^3/s
Downstream water level boundary cond.	$h_{downstream}$	0.239	m
Turbulence model		$k-\epsilon$	

Table 4.6: Case 2, modelling parameters

4.2.3. Case 3: Waal river bend

General

The goal of the third case is to investigate the effect of spiral flow on the bed shear stress in compound channels, which are composed of a main channel and floodplains. The chosen geometry is more complex than Cases 1 and 2 because it is based upon a natural river section, which is taken from a model of the Rhine river branches in the Netherlands. It is doubtful whether the parametrisations for 2DH models, which are based upon idealized conditions, are still accurate for more complex geometries. The third case is selected in order to investigate whether this suspicion is justified. The area of interest is located along the Waal river at some kilometres upstream of Nijmegen, between the villages of Gendt and Bemmel. The location is indicated by Figures C.1 and C.2 in Appendix C. A detailed representation of the geometry and bed topography can be found in Figure 4.4. The inflow is at the south-east (bottom right) of the area, just after another curved section. It is a typical example of a compound river section with a deeper main channel and more elevated floodplains. The main channel is normalized by groynes, which are constructed normal to the channel aiming to increase navigability and flood safety (Jansen et al., 1979). The land use of the floodplains varies. At the inner bend a recreation lake is located which has emerged due to sand mining activities in the 1950s. Furthermore, multiple tree rows are located adjacent to the lake. The first part of the outer bend is relatively vacant. However, further in the outer bend some buildings and industries are located at mounds along the outer bend. These can be recognized in Figure 4.4 by the local elevations. A more detailed illustration can be found in Figure C.2 in Appendix C. The choice for this geometry was made because it shows a typical river bend in a relatively desolate area. Other comparable locations often contain much more buildings and other obstructions close to the main channel. These obstructions are undesired for this research, as they are likely to disturb the spiral flow effects.

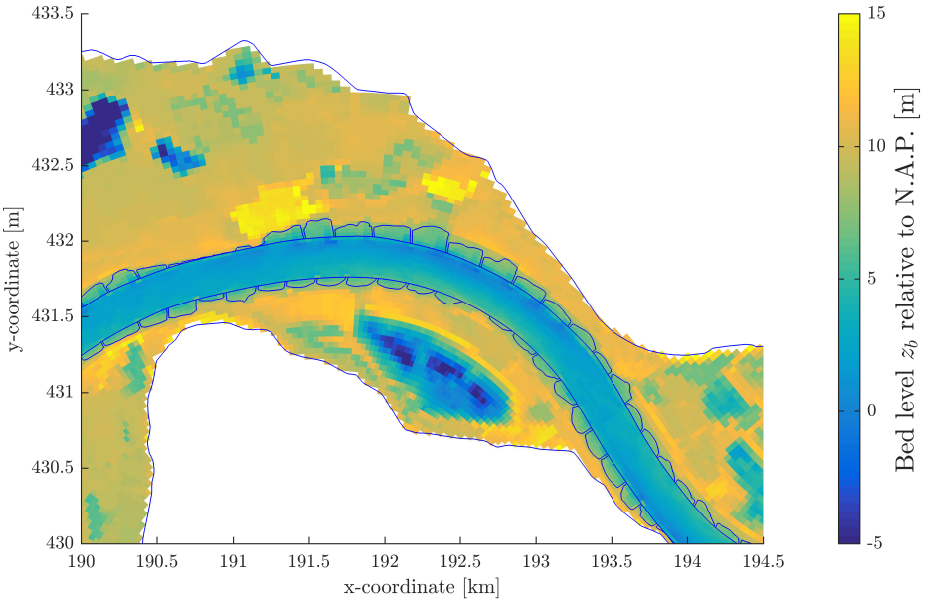

Figure 4.4: Case 3, bed topography of area of interest, with the boundaries of the main channel and dikes indicated in blue

Table 4.7 gives an overview of the relevant physical parameters.

Parameter		Value	
Total discharge	Q	7500	m^3/s
mean flow velocity	U	~1.5	m/s
depth	h	[7,13]	m
width	B	~250	m
radius of curvature	R_c	~2	km
curvature ratio	B/R	~ 0.125	
depth to width ratio	h/B	~ 0.04	
Reynolds number	Re	$1.5 * 10^7$	

Table 4.7: Case 3, physical parameters at the main channel

The discharge was chosen such that significant flow velocities were found in the areas adjacent to the main channel, and furthermore, as well at some places in the floodplains. In this way, it is not only possible to research the presence of spiral flow at the main channel, but as well along the groynes and floodplains. Therefore the choice was made for a total discharge of 7,500 m^3/s, which is considered as an extremely high but still realistic value. It is of the same order of magnitude as found during the flood waves in 1993 and 1995, which led to discharges of 11,000 to 12,000 m^3/s in the Rhine at Lobith. These flood waves can have important morphological consequences due to the increased flow velocities and flooding of floodplains. The other parameters listed in Table 4.7 apply only for the main channel section in between the groynes. The depth varies from 7 m at the inner bend to 13 m at the outer bend. The width of the main channel as measured in between the groynes is 250 m throughout the entire bend. The maximum radius of curvature is about 2 km. The curvature and depth to width ratios are about the same as for Case 2.

Measurement data

Unfortunately, no detailed measurement data is available of meandering compound channels such as found in the Netherlands. As presented in Section 2.1, curved open channels are researched elaborately and this work formed the basis of Cases 1 and 2. However, these investigations are solely focussed on normal non-compound channels. Straight compound channels have been researched elaborately, of which the work of Sellin (1964) and others are well known. Later Ervine et al. (2000) also carried out two-dimensional computations meandering overbank flows. Furthermore, among others, Shiono and Muto (1998) conducted measurements on the development of secondary flow in compound meandering channels. However, each of this researches mainly focusses on turbulence data in idealized rectangular channels. This is not in line with the focus of this research, which is mainly aimed on the performance of numerical models in simulating the bed shear stress in both idealized and natural geometries. Furthermore, it was not feasible within the limited time of this research to entirely set up and validate a numerical model representing the measurements conducted by for example Shiono and Muto (1998), which is a laborious assignment. Therefore the choice was made to solely compare the outcomes of the 2DH and 3D model. Furthermore, the performance of the new methodology applied on low-vertical resolution 3D set-up can still be evaluated in comparison with the conventional 2DH and 3D approaches.

Modelling approach

The model is taken from a comprehensive D3D-FM model of the Rhine river branches in the Netherlands. It is used for conducting hydro- and morphodynamic computations at the Dutch distributaries of the Rijn, namely the rivers IJssel, Waal and Nederrijn. This model is more complex than Cases 1 and 2 and contains the following model components:

- A curvilinear grid (see Table 4.8)
- The bathymetry of the area of interest (see Figure 4.4)
- A polygon file indicating dry areas (outside the dikes, see Figure 4.4)
- A polygon file of weirs, which are used for the groynes and other elevated areas in the model, such as summer dikes and roads in the floodplains
- A polygon file indicating dry areas within the models, such as houses and other obstructions (see Figure C.2)

Table 4.8 gives more information about the grid at or close to the main channel:

Parameter	Value
Average grid cell length (s-direction)	40 m
Average grid cell width (n-direction)	20 m
Number of layers	[1,50]
Layer thickness (z-direction)	$[0.02h, h]$

Table 4.8: Case 3, grid parameters at main channel

The values differ significantly at large distances from the main channel as seen in Figure C.3, but these areas will not be of interest in this research, due to the negligible role of secondary flow farther away from the main channel. Other relevant modelling parameters are indicated in Table 4.9:

Parameter	Value
Manning friction coefficient n	0.023 $s/m^{1/3}$
Upstream discharge boundary cond. $Q_{upstream}$	7500 m^3/s
Downstream water level boundary cond. $h_{downstream}$	13 m
Turbulence model	$k-\epsilon$

Table 4.9: Case 3, modelling parameters

The boundary conditions were applied at several kilometres upstream and downstream of the area of interest. A fixed roughness coefficient was applied to the model, which is a crude assumption due to the large variety of bed types in the river and floodplains. Nevertheless, it is not considered to be of essential influence on the objective of the research.

5
Results

The results obtained based on the methodology and modelling approach explained in Chapters 3 and 4 are described in this chapter. Section 5.1 summarizes the findings from an investigation into the minimally required vertical resolution of the 3D model underlying the new methodology. For the sake of readability, a comparison of low and a high-vertical-resolution 3D models is discussed separately in Appendix D. The outcomes are used in the remainder of the research. In Sections 5.2 to 5.4 a comparison is made for each of the methodologies on the basis of the distinct research components, namely the flow field, spiral flow intensity and bed shear stress. This chapter only contains the most important figures. Additional and more elaborate figures can be found in Appendix E. The entire chapter is written from an observational point of view, as no interpretations are made of the model results. The interpretation and explanation of the results are discussed hereafter in Chapter 6.

5.1. Consistency of the new methodology

Before applying the methodology and assessing the results, it is of importance to find the minimally required vertical resolution for the new methodology to remain consistent. This section presents a summary of the results which can be found in Appendix D. The results were obtained based on 3D model simulations on Case 1 with a number of equidistant layers ranging from 3 to 50. The effect of a varying resolution is assessed for each of the three research components, namely the flow field, spiral flow intensity and bed shear stress. The main conclusion is that a set-up with 5 layers yields sufficiently consistent results. Obviously there is a smaller level of detail in the flow field, however, the general agreement is considered to be sufficient for the aim of this research. The transverse velocities, which are of main importance, generally deviate no more than 10% from high-resolution simulations. Therefore, Section 5.2 only contains the flow field of the low-vertical-resolution 3D model, as it agrees very closely with the flow field of a high-vertical-resolution 3D model, as shown in Appendix D.1. Furthermore, the calculation methods for determining the spiral flow intensity as described in Section 3.3.2 were assessed. It is found that calculation methods using a point-to-point comparison method (see fig. 3.4) yield inconsistent results. Calculation methods using the surface-based determination method (fig. 3.5) provide consistent results. In the remainder of the research, both surface-based calculation methods shown in Figures 3.5 and 3.6 are applied and compared to one another.

5.2. Case 1

5.2.1. Flow field

General water level and velocity development

The maximum deviation of the modelled water levels and velocities of the 2DH and 3D model results remains limited to 4% with respect to the measurements, as can be observed in Figure E.2 in Appendix E.1.2. Another difference is the more steady development of the modelled velocities and water levels in comparison the measurements. Instead of a steady increase of flow velocities, the measurement data shows a stronger acceleration before and at the first stage of the bend, followed by a section in which the flow barely accelerates. Figure 5.1 gives more insight in the cross-sectional distribution of the depth-averaged velocities. Figure 5.1a depicts the results of the 2DH simulation and Figure 5.1b of the 3D simulation. A comparison of the model

results with the measurements is made in Figure 5.2.

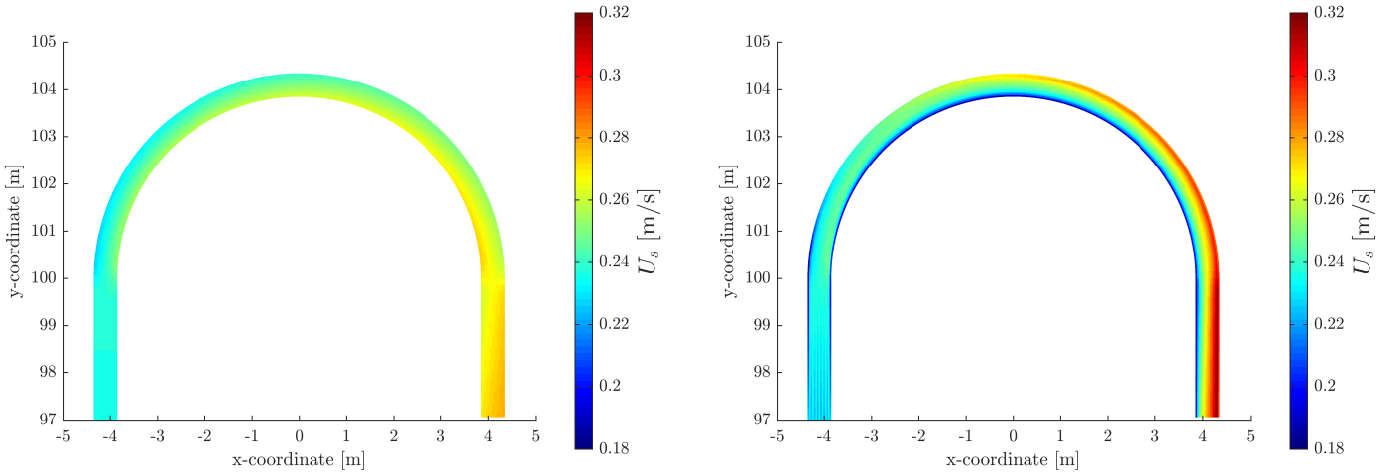

(a) 2DH (b) 3D-LowRes (5 layers)

Figure 5.1: Case 1, top view of the depth-averaged flow velocities

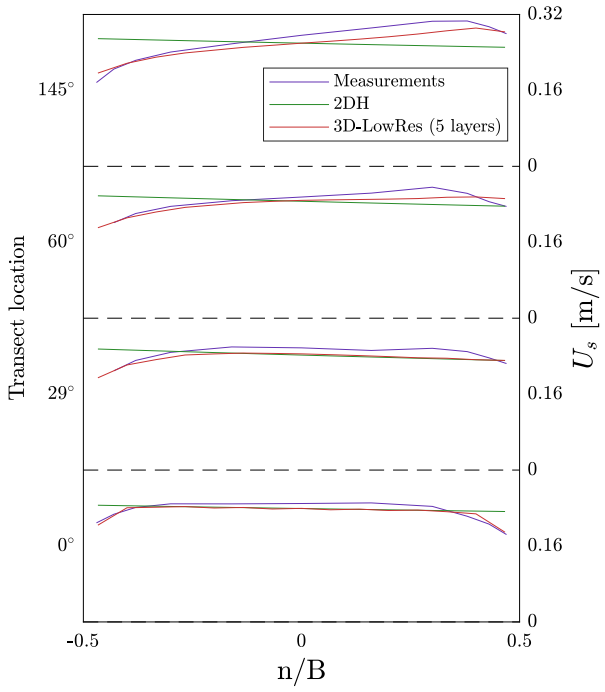

Figure 5.2: Case 1, distribution of the depth-averaged flow velocity at several cross-sections

The noteworthy items in Figures 5.1 and 5.2 are as follows:

- The 2DH model does not represent the decreasing velocities near the side walls, whereas the 3D model clearly succeeds in representing the phenomenon.
- Both the 2DH and 3D models show a more or less equal main velocity redistribution towards the inner bend close to the bend entrance. This can be seen in the 0° section, and to a lesser extent the 29° section. The measurements show less redistribution which can be observed by the flatter profile at the 29° section and the somewhat larger velocities in general.
- This effect remains more or less equal throughout the bend for the 2DH model. On the contrary, the 3D model and measurements show a redistribution towards the outer bend which dominates the initial

effect after the 29° section. The 3D model slightly underestimates the velocities, especially along the outer bend.

Streamwise and transverse development of velocity profiles

Comprehensive plots are made of the cross-sectional distribution of streamwise and transverse velocities. A comparison is made at each of the eight sections of which measurement data of Blokland (1985) and LES data of Booij (2003) was available. The 3D model results originate from a low-vertical-resolution set-up using 5 equidistant layers. The 2DH model results are not plotted, because only the depth-averaged velocity is calculated. Therefore a representative logarithmic streamwise velocity profile is plotted at the channel axis, which underlies 2DH model. The comparison can be found in Figures E.4 to E.11 in Appendix E.1.3. This section only contains a comparison of the cross-sections at 1 m before the bend entrance and at 145° from the bend entrance, shown in Figures 5.3 and 5.4.

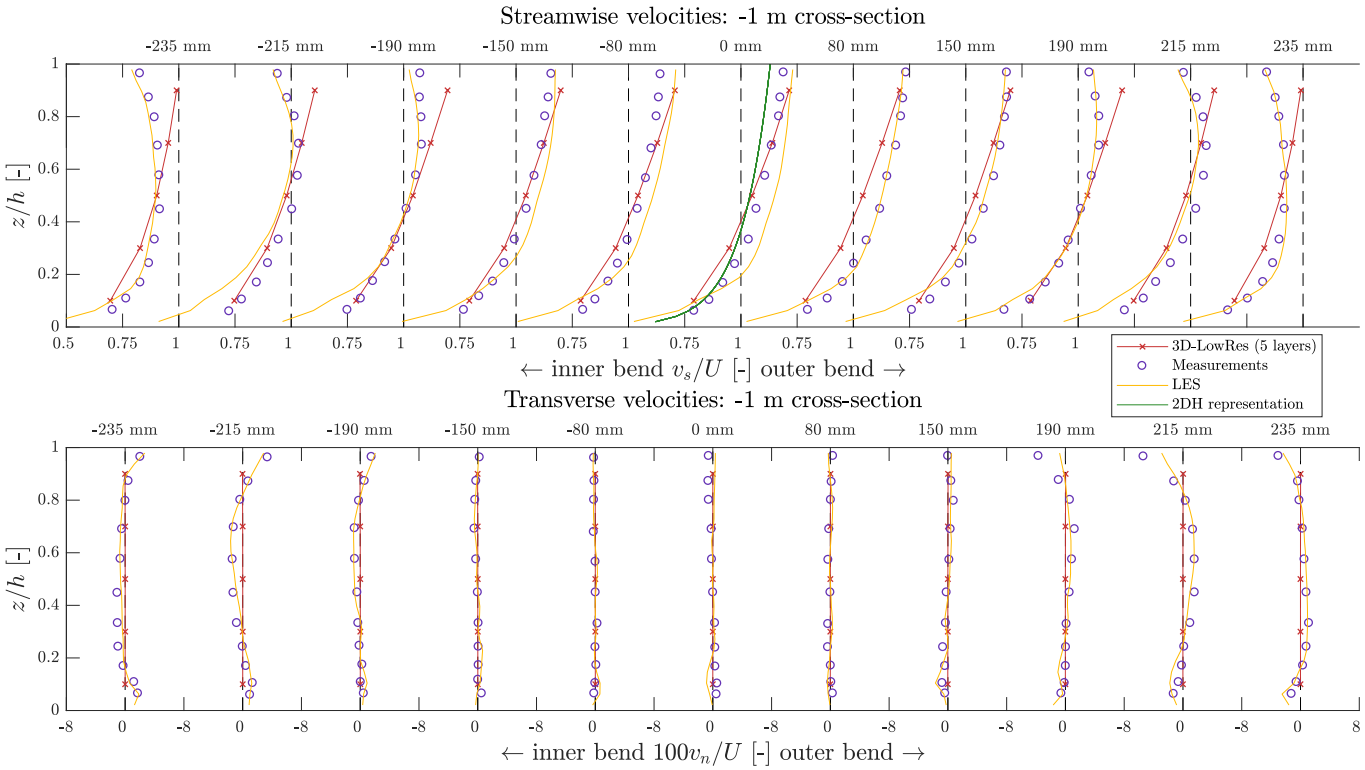

Figure 5.3: Case 1, flow velocities at cross-section 1 m before bend

The most particular characteristics which can be observed in the streamwise velocities (upper half) of Figure 5.3 are as follows:

- The model results near the channel axis (0 mm) agree relatively well with the measurements, except for a small velocity underestimation close to the bed. The gradient of the profile is somewhat larger than the logarithmic velocity profile indicated in green.
- Near the walls (±190, ±215 and ±235 mm) the model results do not represent the significant velocity decrease observed in the upper part of the water column of the measurements.
- Especially in the outermost sections (±235 mm) the velocities near the bed are somewhat underestimated compared with the measurements.

A noteworthy difference in the transverse velocities (lower half) of Figure 5.3 is the absence of the small secondary flows in the model results. These can be observed near the bed and surface at the side walls of the measured profiles.

Figure 5.4 shows the velocity profiles at the end of the bend, at which spiral flow can be considered to be fully developed. The secondary flow velocity profile based upon the derivations of De Vriend (1976) is visualized in green.

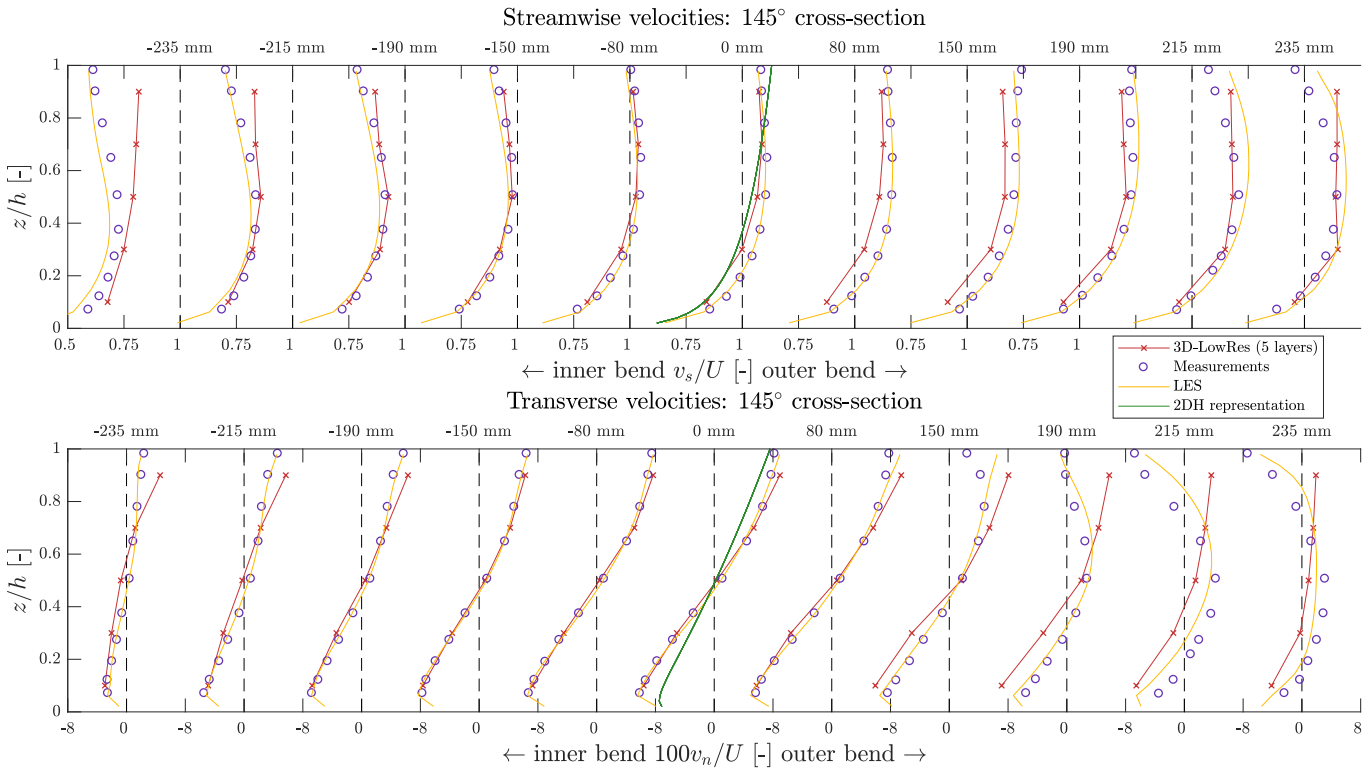

Figure 5.4: Case 1, flow velocities at 145° cross-section

For fully developed secondary flow as shown in Figure 5.4, the most particular observations are as following for the streamwise velocities (upper half):

- Near the channel axis, the velocity profile of both the measurements and model results is flatter than the logarithmic 2DH profile. The 3D model results agree relatively well with the measurements, except for a small underestimation of the velocity magnitudes.
- As well for developed secondary flow, the model results hardly show a velocity decrease near the water surface.
- The velocity decrease at the inner bend and increase at the outer bend is represented fairly well by the 3D model. However, it slightly underestimates the velocities at the outer bend, and overestimates the velocities at the inner bend. This can also be observed more clearly in Figure E.3 in Appendix E.1.2

Based upon the transverse flow velocity information in the lower half of Figure 5.4, the following can be observed:

- The transverse velocity profile agrees well with the measurements near the channel axis. The 2DH representation underestimates the magnitude of the velocities significantly.
- The 3D model overestimates the velocity magnitudes near the inner wall.
- The outer bank cell can be observed in the measurements near the outer wall, which is not captured by the 3D model. The velocities near the surface are in opposite direction compared with the measurements. The near-bed velocities are overestimated by the model.

The above-listed findings do as well apply for the cross-sections with developing flow as found in Figures E.4 to E.11 in Appendix E.1.3. However, at the 15° and 29° cross-sections, one can observe that the 3D model underestimates the transverse velocities in the central region of the flow.

5.2.2. Spiral flow intensity

The spiral flow intensity calculated for the low-vertical-resolution 3D model is compared with the measurements and 2DH results. The spiral flow intensities of the 3D model and the measurements are calculated in the same way, using calculation method A based upon the integral of the transverse velocity profile, as

described in Section 3.3.2 and shown in Figure 3.5a. The intensity of the 2DH model is calculated using the conventional 2DH method, based upon the method of De Vriend (1976) also described in Section 3.3.2. The cross-sectional distribution of the spiral flow intensity is shown for the 29°, 60° and 145° cross-sections in Figure 5.5.

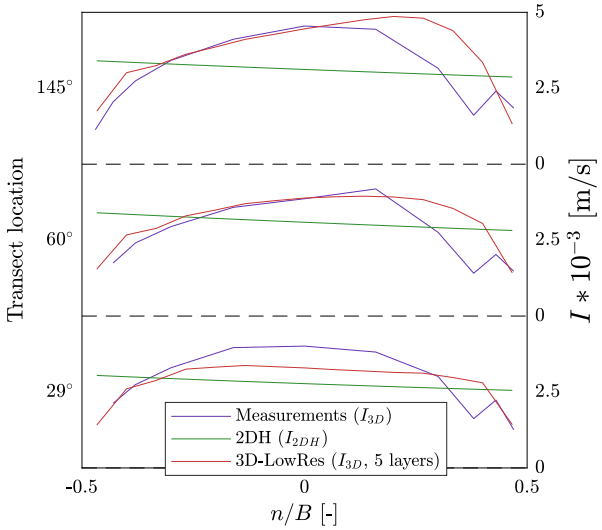

Figure 5.5: Case 1, distribution of the spiral flow intensity at several cross-sections

The following can be observed:

- At the 29° cross-section, the 2DH and 3D models significantly underestimate the spiral flow intensity. The effects of the outer bank cell can already be seen at the far right of the measurement data.
- Further in the bend at the 60° and 145° cross-sections, the 2DH model largely deviates from the intensity of the measurements. The magnitude is overestimated near the banks and underestimated in the central region, and the general gradient is opposite to the gradient of the measurements.
- The 3D model agrees relatively well with the measurements at the 60° and 145° cross-sections, except a significant overestimation near the outer bend. This area corresponds to the outer bank cell region, which is not represented by the 3D model.

5.2.3. Bed shear stress

Magnitude

The bed shear stress magnitude is compared with the measurements and 2DH model in Figure 5.6. Because the bed shear stress is proportional to the velocity squared, it is comparable with what one could expect based on the hydrodynamics reviewed in section 5.2.1. However, for the measurements and 3D model results additional variations may appear due to the strong deviations of velocity profiles from a standard logarithmic profile. The results are shown in Figure 5.6:

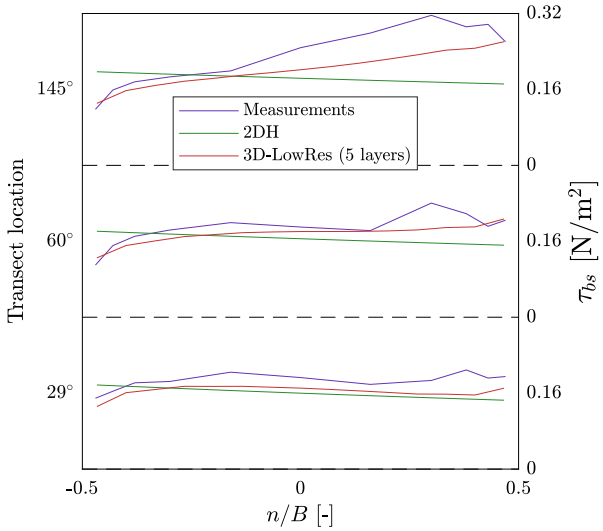

Figure 5.6: Case 1, distribution of the bed shear stress magnitude at several cross-sections

The main observation from are as follows:

- At the 29° cross-section the 2DH and 3D model agree relatively well with one another, but both show a significant underestimation compared with the measurements.
- Further along the bend at the 60° and 145° cross-sections, the 2DH model shows strongly deviating behaviour due to the inverse cross-sectional distribution of the flow velocity, as described in Section 5.2.1. The 3D model roughly follows the development of the measurements, except for a significant underestimation, mainly near the outer bend. This leads as well to an overall underestimation of the cross-section averaged bed shear stress.

Direction

Finally, Figure 5.7 shows a concluding comparison of the bed shear stress directions of the measurements and 2DH and 3D models. Both the measurements and 3D model results are based on the new methodology, whereas the 2DH model uses the conventional 2DH approach for determining the bed shear stress direction.

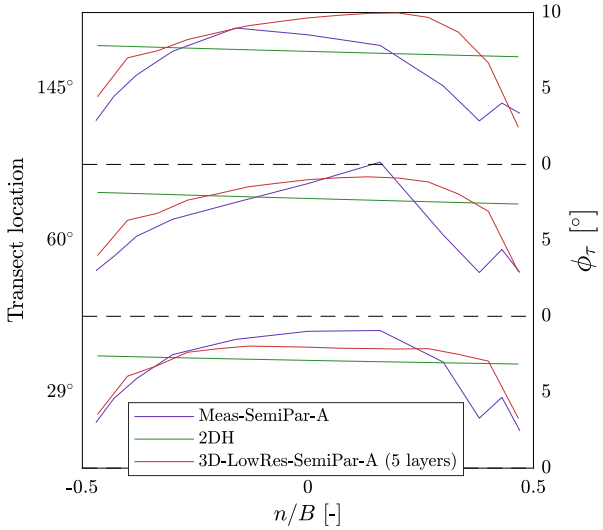

Figure 5.7: Case 1, distribution of the bed shear stress angle deviation at several cross-sections

The deviations of the 2DH model in the flow field and spiral flow intensity are of influence on the bed shear stress direction, as observed in Figure 5.7. One can observe a relatively good agreement of the 3D model with the measurements at the 29° cross-section, except for the area near the outer bank wall. This deviation in the outer bend becomes larger further down the bend.

A deeper look into the performance of the new methodology is taken in Figure 5.8. It contains the results of the following methodologies:

- A conventional 2DH model, which is widely used in river engineering practice (*2DH*).
- The new methodology applied to a low-vertical-resolution 3D model with 5 layers (*3D-LowRes-SemiPar*), using:
  - Calculation method *A* based on the integral of the entire transverse velocity curve (see fig. 3.5a in section 3.3.2).
  - Calculation method *B* based on the integral of the bottommost 20% of the transverse velocity curve (see fig. 3.5b).
- A 3D model using the conventional approach of equating the bed shear stress direction to the flow direction of the bottommost computational layers (*3D-Conv*), using:
  - 5 layers (*LowRes*), i.e. based on the bottommost flow vector at 10% of the depth. This is an additional reference case.
  - 50 layers (*HighRes*), i.e. based on the bottommost flow vector at 1% of the depth. This is considered to be the most accurate representation of the bed shear stress angle deviation.

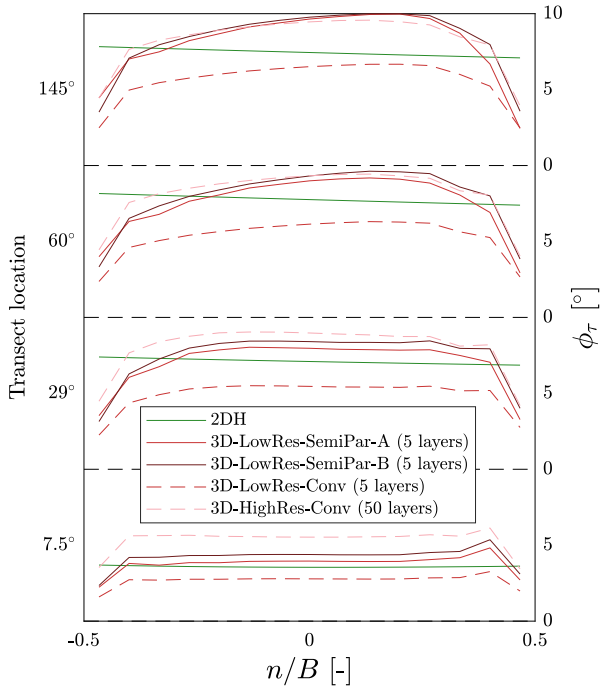

Figure 5.8: Case 1, the bed shear stress angle deviation, overview performances of the new methodology in comparison with conventional methodologies

When comparing the results with the *3D-HighRes-Conv* reference case, the following can be observed:

- The 2DH model underestimates the bed shear stress direction altogether, except for an overestimation near the side walls.
- The *3D-LowRes-Conv* model shows that the angle deviation is significantly underestimated along the entire bend when using a low-vertical-resolution 3D model with the conventional methodology.
- The new methodology (*3D-LowRes-SemiPar-A* and *B*) shows a significant improvement compared with *3D-LowRes-Conv*. However, still a significant underestimation is made compared with the reference case for cross-sections with developing flow (15° and 29°). In case of fully developed flow (60° and 145°), the new methodology closely agrees with the reference case, aside from a small underestimation near the inner bend and an overestimation near the outer bend.

- When comparing calculation methods *A* and *B* of the new methodology, one can observe that *B* offers a slight improvement to *A*. However it still differs significantly from the reference case still at the 7.5° cross-section with developing spiral flow.

5.3. Case 2

5.3.1. Flow field

General water level and velocity development

The deviation of the water levels and depth-averaged velocity of the 2DH and 3D model results for Case 2 also remained limited to 4%, as can be observed in Figure E.16 in Appendix E.2.2. The main differences which remained is a smoother velocity development of 2DH and 3D models in comparison with the measurements. Furthermore, the 2DH and 3D models predicted a slightly higher water level than found in the measurements.

Figure 5.9 gives more insight in the cross-sectional distribution of the depth-averaged velocities of the 2DH (Figure 5.9a) and 3D (fig. 5.9b) models:

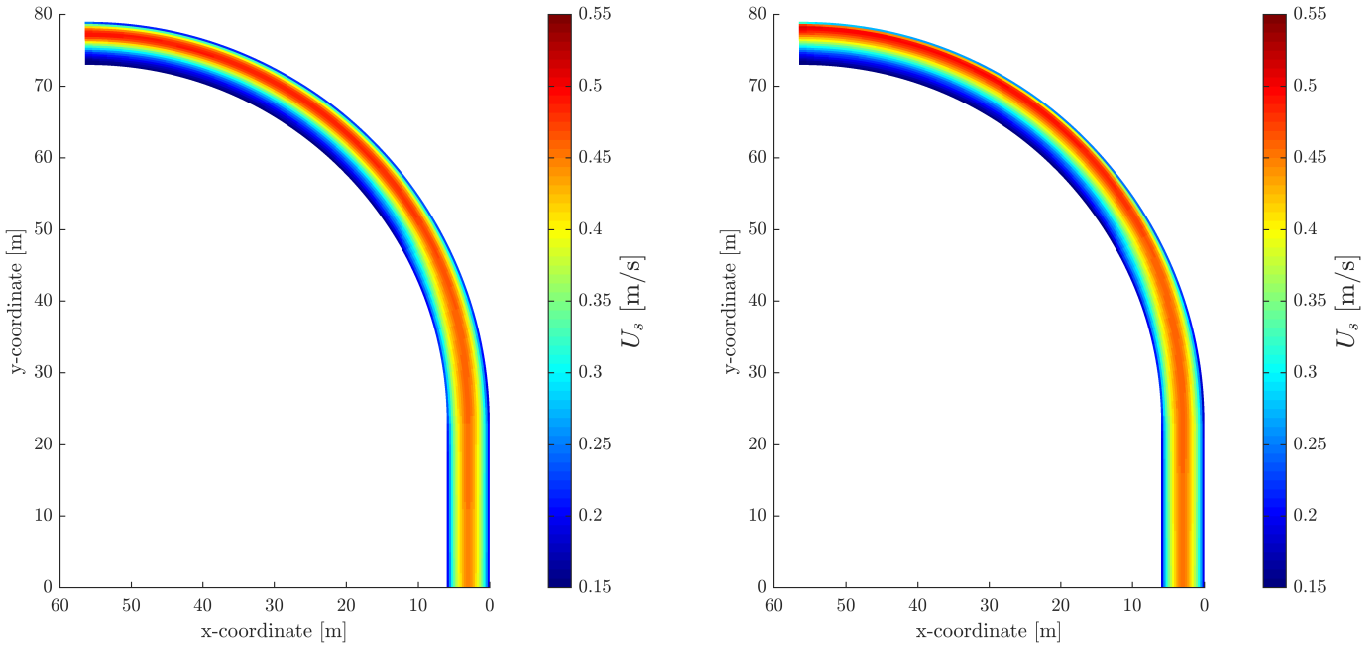

(a) 2DH

(b) 3D-LowRes (5 layers)

Figure 5.9: Case 2, top view of the depth-averaged flow velocities

A comparison of the model results with the measurements is made in Figure 5.10 for three cross-sections, namely at the 0°, 27.5° and 82.5° from the bend entrance.

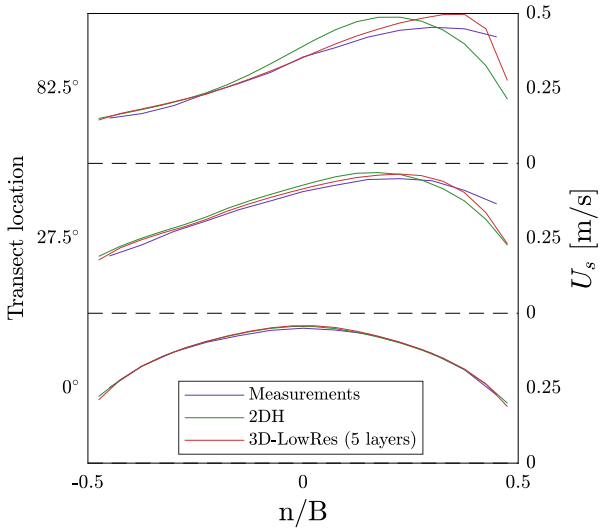

Figure 5.10: Case 2, depth-averaged flow velocities

The developed bed topography leads to much smaller differences between the 2DH and 3D model results and measurements in comparison with Case 1. Nevertheless, still a clear difference can be observed between the 2DH model on the one hand and the 3D model results and measurements on the other hand. The 2DH model underestimates the shift of the higher flow velocities towards the outer bend, which becomes clearer as the secondary flow develops throughout the bend.

Streamwise and transverse development of velocity profiles

As stated in Section 4.2.2 the available measurement data found in the report of De Vriend and Koch (1978) as limited to the depth-averaged velocity, spiral flow intensity and water level. Only low-detail graphs were available of some of the velocity profiles. Therefore an elaborate comparison as for Case 1 is not possible. Figure 5.11 shows the velocity profiles throughout the bend, originating from a low-vertical-resolution 3D model using 5 layers. Figures E.18 to E.25 in Appendix E.2 show the profiles separately for each of the 8 sections along with the local bed topography.

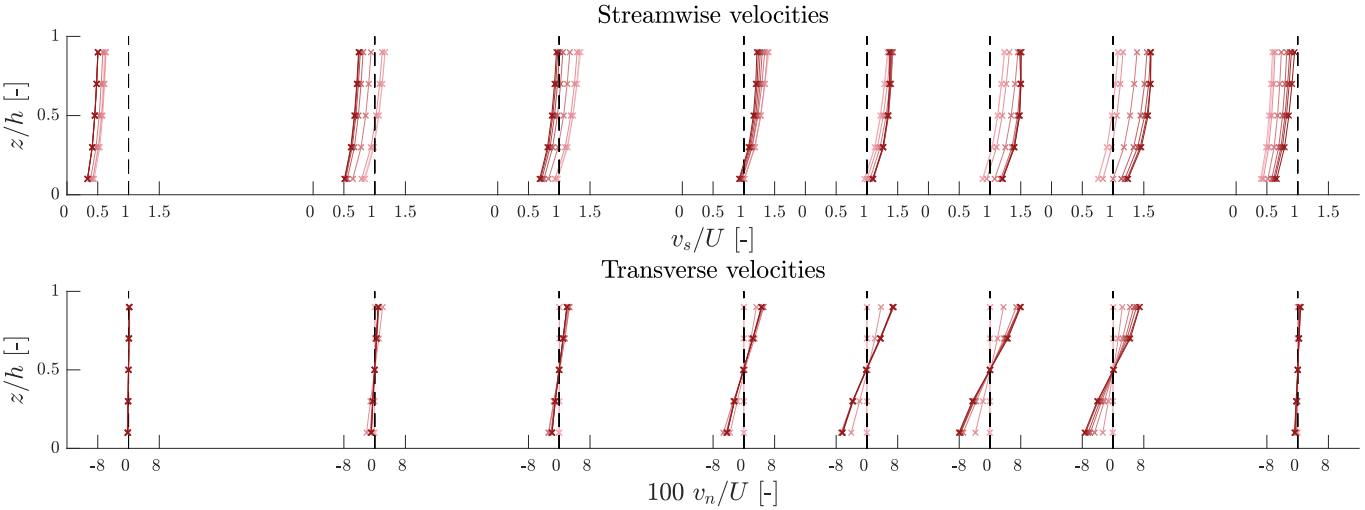

Figure 5.11: Case 2, flow velocities throughout the bend, changing from pink before the entrance of the bend to dark red at the last section located at 82.5° from the entrance

Figure 5.11 confirms the shift of velocities toward the outer bend as observed in Figures 5.9 and 5.10. The secondary flow velocity profiles develop very quickly. On the contrary, the flattening of the streamwise velocity profiles occurs much further in the bend. A visual comparison of the model results with the measured profiles in the report De Vriend and Koch (1978) shows the same type of deviations as found for Case 1, albeit to a significantly smaller extent. The 3D model seems to underestimate the flattening of the streamwise velocity

profiles. Furthermore, according to De Vriend and Koch (1978) the outer bank cell was not observed in the measurements.

5.3.2. Spiral flow intensity

The spiral flow intensity has been calculated for the low-vertical-resolution 3D model in comparison with the measurements and 2DH model. The spiral flow intensities of the measurements were given in the report of De Vriend and Koch (1978). The cross-sectional distribution of the spiral flow intensity is shown in Figure 5.12:

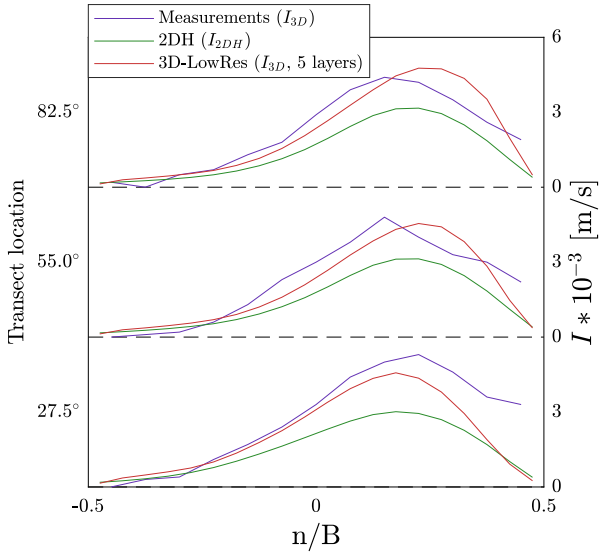

Figure 5.12: Case 2, spiral flow intensity

The most striking difference is the significant underestimation of the 2DH model in comparison with the measurements. The 3D model and the measurements agree better, however, still significant differences can be found. When looking at the development throughout the bend, the 3D model shows an outward directed shift of the velocity peak, whereas the measurements show the opposite. Another difference is the sudden drastic increase ('overshoot') of the measured spiral flow intensity in comparison with the 2DH and 3D models, which both show a gradual increase instead of an initial overshoot.

5.3.3. Bed shear stress

Magnitude

The development of bed shear stress magnitude for the measurements and 2DH and 3D model can be found in Figure E.17 in Appendix E.2.3. The results are comparable with the depth-averaged velocities in Figure 5.10, upon which the bed shear stress is based. A deliberate choice was made to base the bed shear stress of the 3D model on the depth-averaged velocity, whereas taking the velocity near the bed would be more accurate. This is due to the fact that only depth-averaged velocity data was available from the measurements. Therefore the choice was made to use the depth-averaged velocity of the 3D model as well, in order to allow a fair comparison between the model results with the measurements. In reality, the bed shear stress magnitude of the measurements and 3D model is expected to be somewhat larger. This is due to the flattening of the streamwise profile, leading to relatively large flow velocities near the bed, as explained in Section 5.3.1.

Direction

Figure 5.13 shows a comparison of the bed shear stress directions of the 2DH model, low-resolution 3D model and measurements. The new approach for determining the bed shear stress direction is applied to the 3D model and measurements. The streamwise component of the bed shear stress is based upon the depth-averaged velocity, which is expected to be underestimated as explained above. This might lead to an overestimation of the bed shear stress angle deviation of both the measurements and 3D results.

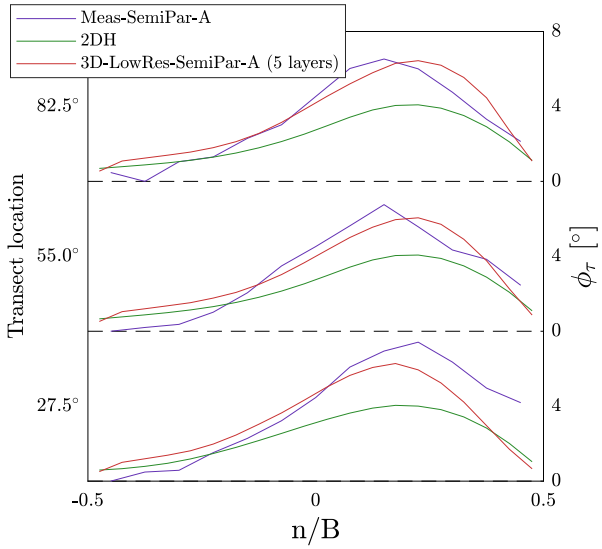

Figure 5.13: Case 2, bed shear stress angle deviation

The large differences in the spiral flow intensity as shown in Figure 5.12 directly affect the transverse bed shear stress component. As a result, the bed shear stress angle differs strongly between the measurements and 3D model results at one hand, and the 2DH results on the other hand. The 2DH model results show a significant underestimation.

In a similar way to Case 1, a deeper look is taken at the performance of the new methodology for Case 2 in Figure 5.14. It is the same comparison as for Case 1 in Figure 5.8 in Section 5.2.3. The only difference is that the *3D-HighRes-Conv* reference case is based on 30 rather than 50 layers. Therefore it might still slightly underestimate that bed shear stress angle deviation.

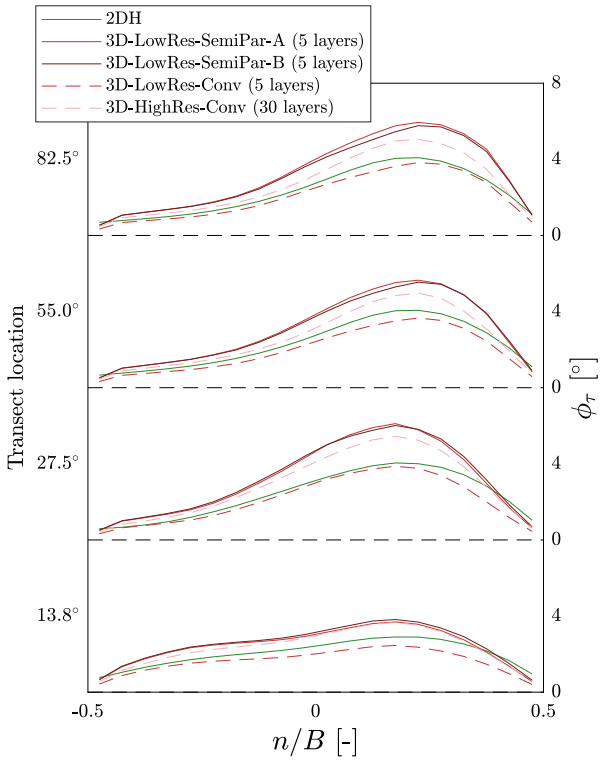

Figure 5.14: Case 2, the bed shear stress angle deviation, overview performances of the new methodology in comparison with conventional methodologies

When comparing the results with the *3D-HighRes-Conv* reference case, the following can be observed:

- Similar to Case 1, the 2DH model underestimates the bed shear stress direction altogether. However, it does not show large deviations near the side walls as found for Case 1.
- Similar to Case 1, the *3D-LowRes-Conv* model shows that the angle deviation is significantly underestimated along the entire bend when using a low-vertical-resolution 3D model with the conventional methodology.
- The new methodology (*3D-LowRes-SemiPar-A* and *B*) shows a significant improvement compared with *3D-LowRes-Conv*. However, it slightly overestimates the angle deviation from the 27.5° cross-section onward.
- When comparing calculation methods *A* and *B* of the new methodology, one can observe that *B* only offers a minor improvement to *A* at the 55° and 82.5° cross-sections.

5.4. Case 3

5.4.1. Flow field

General water level and velocity development

Contrary to Cases 1 and 2, no measurement data is available for Case 3. Therefore only a comparison is made between the 2DH and 3D model and the performance of the new methodology is assessed. The downstream water level boundary is located at some distance from the area of interest. It roughly corresponds with an expected water level for the imposed discharge. However, the exact boundary conditions are not of essential importance within the context of this research.

The general data analysis is carried out for the entire area indicated by Figure 5.16. However, colour maps can be inconvenient for indicating small differences. Therefore, analogous to the other cases, 7 cross-sections were chosen for more detailed data analyses. These are shown in Figure 5.15. The cross sections were chosen such that all stages of developing flow are covered, up to the last section at which the spiral flow is decaying. These sections are more or less equidistant and located such that there is no or little influence of flow around the groynes. The sections are referred to by their angle relative to the first cross-section, namely 0°, 2.5°, 9°, 22°, 34°, 50° and 66°,

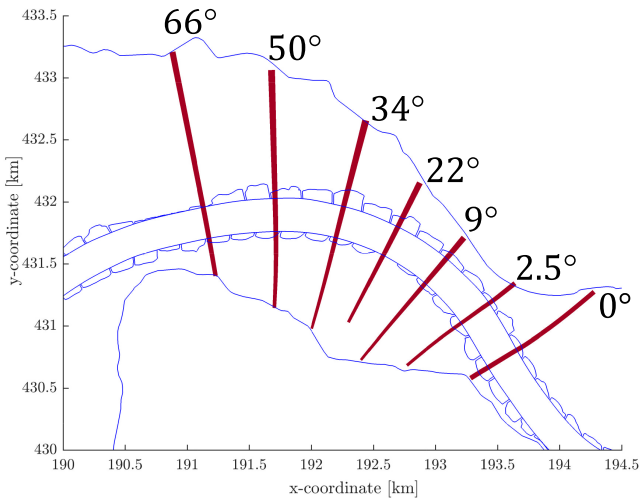

Figure 5.15: Case 3, location of the analysed cross-sections

Figure 5.16 shows the depth-averaged velocities of the 2DH and 3D models. Figures E.27 and E.28 in Appendix E.3 show enlarged versions.

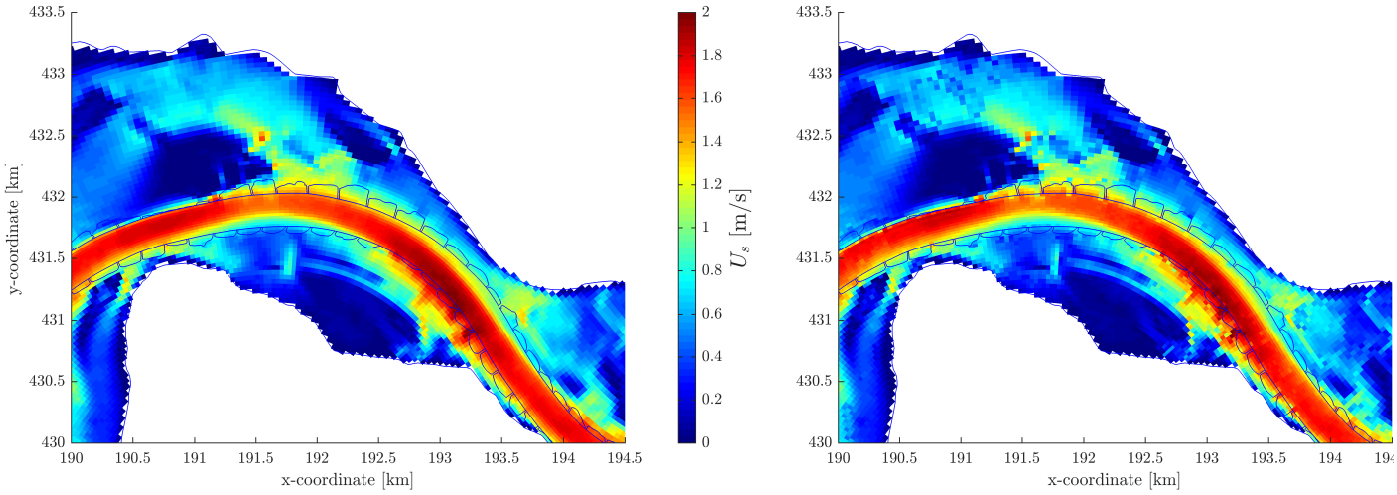

(a) 2DH model

(b) 3D model

Figure 5.16: Case 3, depth-averaged flow velocities

No large differences between the 2DH and 3D model results can be observed in these figures. The most prevailing difference is the smoothness of the 2DH model results on the one hand, and the more local variation of the 3D model results, recognizable by the more scattered representation. This is especially visible near the groynes, where the 3D model shows a local deceleration which is barely captured by the 2DH model. Furthermore, when closely observing the velocities at the outer bend, one can observe that the 3D model shows slightly larger velocities than the 2DH model. This is confirmed by comparing the depth-averaged velocities as shown in Figure 5.17. It shows the velocity distribution in a cross-sectional range of twice the width of the main channel.

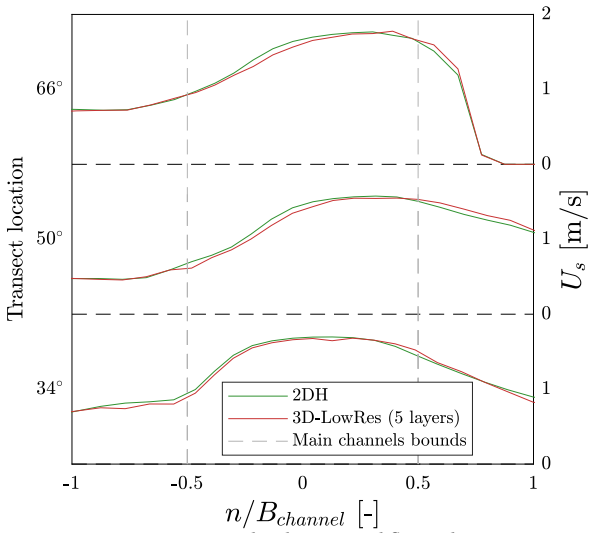

Figure 5.17: Case 3, depth-averaged flow velocities

Streamwise and transverse development of velocity profiles

The velocity profiles at each of the cross-sections indicated in Figure 5.15 are depicted in Figures E.32 to E.38 in Appendix E.3.4. In this section only Figure 5.18 is shown, indicating the velocity profiles at the 34° cross-section. The channel width $B_{channel}$ is for each of the cross-sections 250 m. The velocity profiles are based on the outcomes of a high-vertical-resolution 3D model with 5 equidistant layers. The main flow direction is determined for each velocity profile separately and varies slightly within the main channel bounds. Outside the main channel bounds, the local main flow directions vary strongly from the main flow direction of the main channel. More attention will be paid to this in Section 5.4.3.

The 0° cross-section still shows the decaying spiral flow of the upstream bend, which is more or less vanished

at the 2.5° cross-section. The transverse velocities along the 0°, 2.5° and 9° cross-sections are still largely influenced by an inflow from the upstream floodplain. This inflow generates secondary flow cells in the opposite direction of the curvature induced spiral flow cell, as can be observed in the 2.5° and 9° cross-sections indicated in Figures E.33 and E.34. The 22°, 34° and 50° cross-sections show a relatively undisturbed and consistent presence of spiral flow over the width of the main channel, comparable to Figure 5.18. Outside the main channel bounds the spiral flow effects vanish rapidly. Only at the 50° cross-section one can observe significant influence of the spiral flow outside the main channel bounds. At the 66° cross-section the transverse velocities have decreased significantly, and furthermore, some disturbing effects can be observed at the outer bend. This is due to steep banks close to an industrial area which is located next to the main channel. The streamwise velocity profiles at each of the cross-sections clearly appear to flatten throughout the bend. This mainly occurs in areas within the main channel bounds, where significant transverse velocities are found.

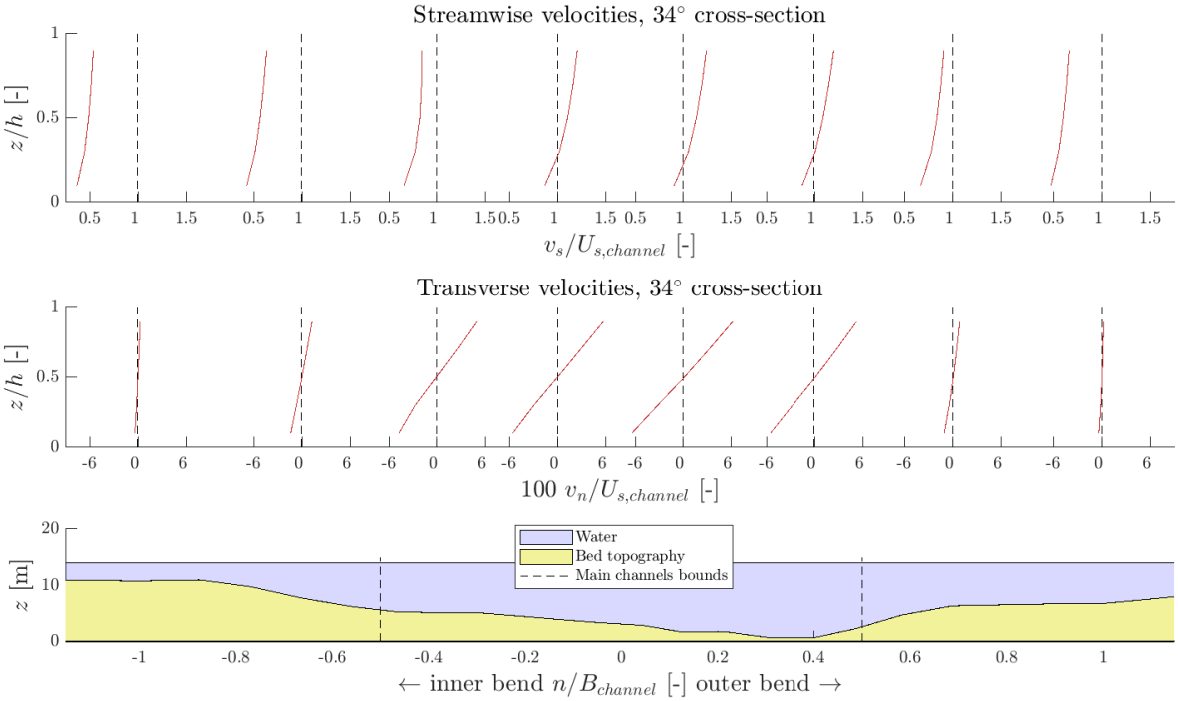

Figure 5.18: Case 3, flow velocities at 34° cross-section

5.4.2. Spiral flow intensity

The next step is comparing the spiral flow intensity of the low-vertical resolution 3D model with 5 layers with the 2DH model. The outcomes of the 22°, 34°, 50° and 66° cross-sections are depicted in Figure 5.19.

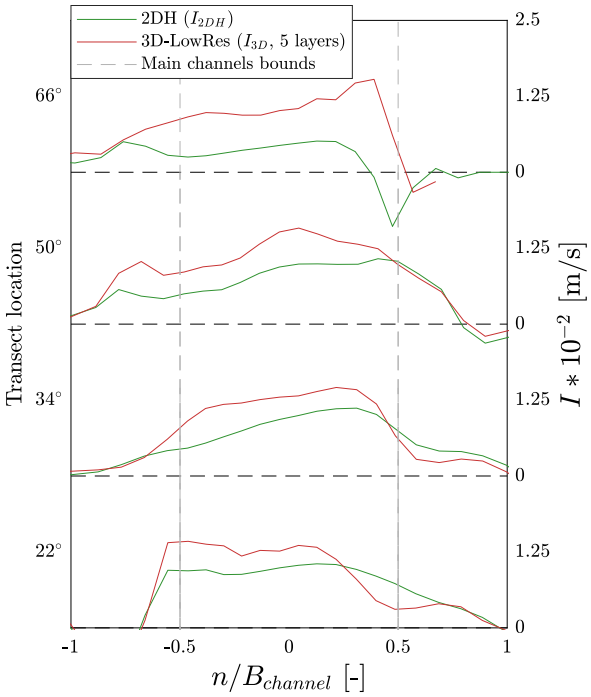

Figure 5.19: Case 3, spiral flow intensity

In comparison with Cases 1 and 2, the effect of local disturbances clearly influences the development of the secondary flow. This is especially the case for the 66° cross-section where higher grounds are located close to the main channel. Nevertheless, still some generic observations can be made. In general, one can observe that both models show a quick decay of the spiral flow outside the main channel bounds. The intensity generally decreases to minor magnitudes at a distance of $0.5B_{channel}$ away from the main channel bounds. Furthermore, a large difference can be observed between the intensity of the 2DH and 3D model, which is in agreement with the results found for Cases 1 and 2. This difference is the largest for the 66° cross-section. In addition to this, near the right channel bound ($n/B_{channel} = 0.5$) of the 22°, 34° and 50° cross-sections, a relatively quick outward decay of the intensity can be observed at the 3D model, whereas the relative decay of the 2DH model is much smaller.

5.4.3. Bed shear stress

Magnitude

The bed shear stress magnitudes are depicted in Figure E.31 in Appendix E.3.3. The results are comparable with the depth-averaged velocities as shown in Figure 5.17. The 3D model shows somewhat larger bed shear stresses at the outer bend. However, the differences remain relatively small in contrast to Cases 1 and 2, at which more obvious deviations were found between the 2DH and 3D model.

Direction

In a similar way to Cases 1 and 2, a comparison is made for Case 3 between the new methodology and conventional methodologies. It is the same comparison as for Case 1 and 2 in Figures 5.8 and 5.14 in Sections 5.2.3 and 5.3.3 respectively. The depicted angle deviations are relative to the local main flow direction. The local main flow directions can differ from the cross-section averaged main flow direction. This is much more prevalent for Case 3 than for Cases 1 and 2, due to the more arbitrary geometry. The comparison is shown in Figure 5.20:

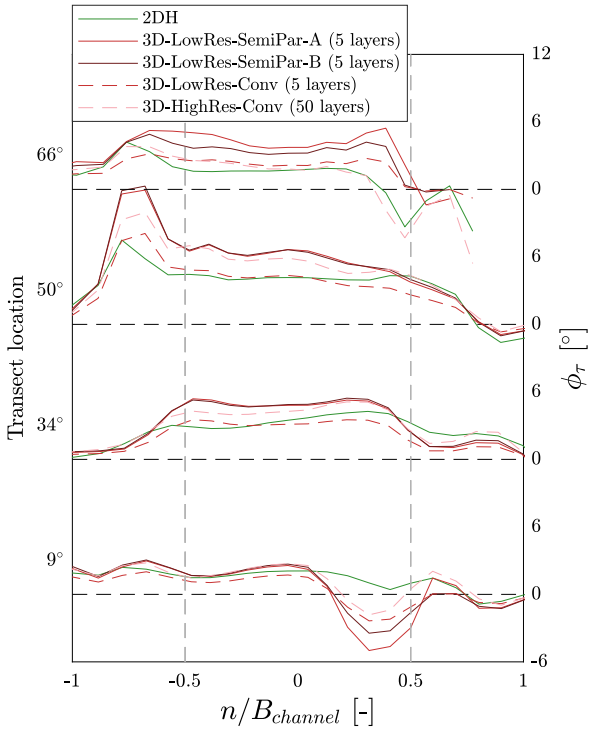

Figure 5.20: Case 3, the bed shear stress angle deviation, overview performances of the new methodology in comparison with conventional methodologies

When comparing the results with the *3D-HighRes-Conv* reference case, the following can be observed:

- The 2DH model underestimates the bed shear stress direction, mainly at the 34° and 50° cross-sections. Furthermore, it shows relatively large angle deviations near the outer band channel bound at the 34° and 50° cross-sections, whereas the reference case shows a much stronger decrease of the angle deviation. Finally, in shows erroneous behaviour at the inflow of the floodplain at $n/B_{channel} \approx 0.4$ of the 9° cross-section
- The *3D-LowRes-Conv* model shows that the angle deviation is significantly underestimated at most locations when using a low-vertical-resolution 3D model with the conventional methodology. However, it is in close agreement with the reference case at the 66° cross-section.
- The new methodology (*3D-LowRes-SemiPar-A* and *B*) shows an improvement compared with *3D-LowRes-Conv* at the 34° and 50° cross-sections. However, it shows erroneous behaviour near the higher grounds at $n/B_{channel} \approx 0.5$ of the 9° cross-section. Furthermore, it overestimates the angle deviation at the entire 66° cross-section.
- When comparing calculation methods *A* and *B* of the new methodology, one can observe that *B* offers a slight improvement to *A* at the 9° and 66° cross-sections.

The figure depicted above shows the angle deviations relative to the local main flow direction. However, the local main flow directions can deviate strongly from the main flow direction averaged over the cross-section of the main channel, especially in the transition area from main channel to the floodplains. This is due to the larger variations in the topography and the presence of the floodplains. For Cases 1 and 2 this was not of relevance, as the deviations between the local and cross-section averaged main flow directions were negligible. However, this does not apply for Case 3. This is confirmed by Figure E.29 in Appendix E.3.2, showing the vectors of the depth-averaged flow at the seven analysed cross-sections. A more detailed view is given in the left graph of Figure 5.21. It shows the angle deviation of the local main flow θ_{U_s} relative to the main flow direction averaged over the entire main channel θ_U, as shown in Figure 3.7a in Section 3.3.1. This means that the cross-sectional average of the angle deviation of the main flow (ϕ_{U_s}) within the main channel bounds is by definition zero. Outside the main channel bounds one can observe negative values, indicating local flow directed toward the outer bend. The middle graph of Figure 5.21 shows is the same as Figure 5.20,

which is the bed shear stress angle deviation relative to the local main flow direction θ_{U_s}. The right graph is the combination of the left and middle graphs, showing the angle deviation of the bed shear stress relative to the main flow direction of the main channel θ_U. The results within the main channel bounds are comparable with Figure 5.20. However, when observing the results outside the main channel bounds, one can observe that the bed shear stress angle deviation is mainly caused by the dynamics of the local channel topography, and only to a small extent by the spiral flow. In summary, when observing the areas outside the main channel bounds in Figure 5.21, one can observe the minor effect of the spiral flow on the bed shear stress direction with respect to the influence of the local flow conditions.

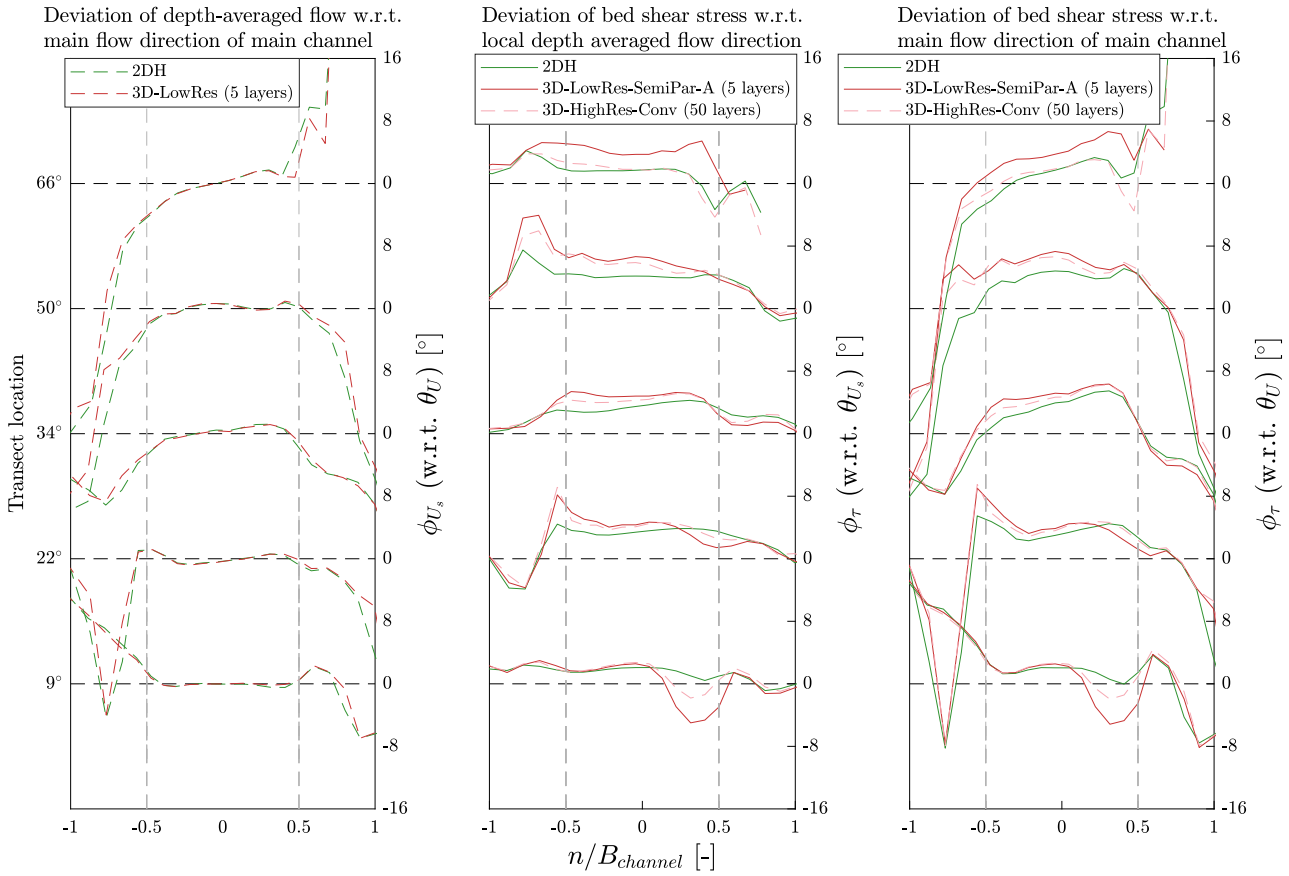

Figure 5.21: Case 3, combined plot of angle deviations

6

Discussion

This chapter discusses the results presented in Chapter 5. It gives an interpretation and explanation of the results and evaluates the new methodology presented in this research. At first, Section 6.1 discusses the investigation into the minimally required vertical resolution for the new methodology to remain consistent. Subsequently, the research components are evaluated one by one in Sections 6.2 to 6.4. The discussion is combined for the three cases, in contrast to Chapter 5, at which the cases were treated one by one. Referrals will be made to figures found in Chapter 5 in order to avoid repetition.

6.1. Consistency of the new methodology

The results of the investigation to the consistency of the new methodology are presented in Section 5.1. This is assessed separately for the flow field, spiral flow intensity and bed shear stress. Due to the limited time available, the consistency of the methodology was only assessed for Case 1. The hydrodynamics are sufficiently consistent for 3D models when using set-ups of at least 5 layers. Only at some locations small deviations were found for a 5-layer set-up in comparison with a high-vertical-resolution set-up using 15 layers. An example of this is shown in Figure 6.1. One of the most particular deviations is an underestimation of transverse velocities in sections with developing flow (fig. 6.1a). On the contrary, higher transverse velocities are observed in sections with developed flow (fig. 6.1b).

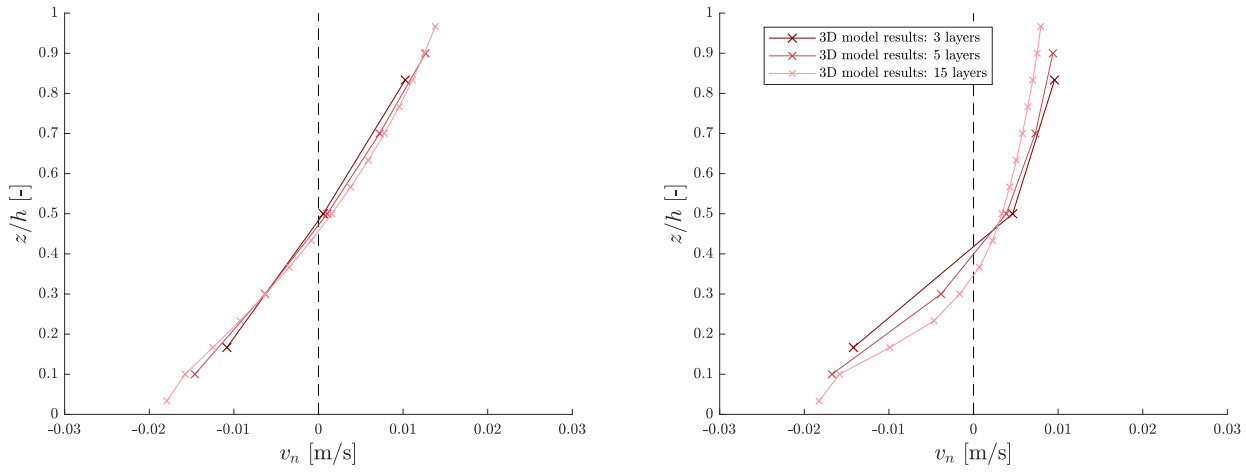

(a) 15° cross-section, channel axis (developing flow) (b) 145° cross-section, outer bend (developed flow)

Figure 6.1: Case 1, dependency of transverse velocity profiles on vertical resolution

This leads to the suspicion that low-resolution models initially have some difficulty with reproducing the momentum redistribution in case of developing flow, but ultimately overestimate the redistribution in case of fully developed flow. The deviations in the flow field affect the determination of the spiral flow intensity, and consequently the angular deviation of the bed shear stress. However, applying the new methodology

on a low-vertical-resolution 3D model with 5 layers still yielded sufficiently consistent results for the spiral flow intensity and bed shear stress angle deviation. However, it should be recalled that this is solely based on a review of Case 1. Especially for Case 3 this might be a blunt assumption, due to the relatively large local variability of the flow field compared with Cases 1 and 2.

6.2. Flow field

6.2.1. General development

The incapability of 2DH models to represent the spiral flow-induced transverse redistribution of momentum can be clearly recognized for Case 1 in Figure 5.2. The depth-averaged velocities computed by the 2DH model deviate largely from the measurement quantities. In contrast to the 2DH model, the low-vertical-resolution 3D model is able to represent the momentum redistribution, and therefore agrees relatively well with the available measurements for Case 1, and to a lesser extent for Case 2. The developed bed topography of Case 2 (fig. 5.10) leads to less prevalent differences between the models and measurements. The differences between the computed depth-averaged velocities of the 2DH and 3D model appear to be minor for Case 3 (fig. E.30), indicating that the effect of momentum redistribution is small for this specific case. The combined results demonstrate the major influence of the bed topography on the velocity redistribution in comparison with the influence of spiral flow. When the aim of an investigation is limited to modelling the general velocity development in a geometry similar to an equilibrium situation, the added value of 3D models relative to 2DH models for determining the flow field can be small or even minor.

The depth-averaged velocities of the measurements and model results deviate to some extent, which can be partially attributed to difficulties in calibrating the models with the measurements. This is due to the relatively unsteady development of the measured velocities throughout the bend, in contrast to a more smooth development of the model results. However, the deviation of the model from the measurements remains limited to 10%.

6.2.2. Streamwise and transverse development of velocity profiles

General

A detailed comparison of the velocity profiles was only possible for Case 1, due to the insufficient availability of measurement data for Cases 2 and 3. However, it is still possible to compare the outcomes of the 3D model results of Cases 2 and 3 in comparison with the analytically derived velocity profiles of De Vriend (1976), which form a representation for the derivations underlying a 2DH model. In this section, three aspects of the velocity profiles are discussed separately, namely a more detailed look into the velocity redistribution (1), the representation of turbulence features (2), and lastly the deformation of velocity profiles (3).

Momentum redistribution

Section 5.2.1 shows for Case 1 that the low-vertical-resolution 3D model slightly underestimates the transverse velocities at stages of developing flow, mainly near the channel centre. The transverse flow induces a redistribution of momentum, leading to an increase of streamwise velocities along the outer bend and a decrease along the inner bend. It is also shown for Case 1 that the 3D model underestimates the redistribution of streamwise velocities. Based on these findings it appears that the 3D model underestimates the redistribution of momentum. This is not only related to the use of low-vertical resolution model set-ups as discussed in Section 6.1, but apparently inherently related to 3D models, as the underestimation is also found for higher-vertical-resolution 3D model set-ups. This is in line with suspicions drawn by Ottevanger et al. (2009), who link this behaviour to the use of the isotropic k-ϵ turbulence closure model. The authors state that models with isotropic turbulence modelling underestimate the transverse velocities and related outward transport of momentum, which complies with the results found for Case 1. However, this cannot be proved for Case 2 when comparing the depth-averaged velocities of the 3D model and measurements in Figure 5.12 in Section 5.3.1. More insight could be obtained when raw measurement data of Case 2 would be available, which was not the case for this research.

Turbulence features

The low-vertical-resolution 3D model does not represent the outer bank cell as found in the measurements of Case 1. This problem is inherently related to 3D RANS models, and therefore independent on the applied resolution. In contrast to Case 1, De Vriend and Koch (1978) reported that the outer bank cell was not found

during the measurement campaign on the geometry of Case 2. These cells are generally neither found in real-world rivers with a comparable geometry as modelled for Case 3. As far as Case 1 is concerned, the disagreement of the 3D model with the measurements is not only limited to the non-inclusion of the outer bank cell. The 3D model fails as well to fully reproduce the strong decrease of streamwise velocity near the surface which is mainly found near the channel walls, as described in Section 5.2.1 and recalled by Figure 6.2. This figure indicates the profiles found for the measurements and 3D model results. Many authors, including Van Balen (2010), Van Sabben (2010) and the references herein, attribute the outer bank cell to the anisotropy of turbulence in the corners of a rectangular cross-section. This gives rise to the aforementioned decrease of streamwise velocity near the water surface and leads to the development of the outer bank cell. The aforementioned authors attribute the failure of the 3D model in reproducing these phenomena to the use of the linear $k-\epsilon$ turbulence model in Delft3D. This turbulence model is unable to predict anisotropic turbulent stresses. These limitations of the Delft3D model appear to be of smaller importance for Cases 2 and 3, because these are not based upon rectangular cross-sections. The same is expected to apply for Case 3, but this cannot be validated due to the absence of measurement data.

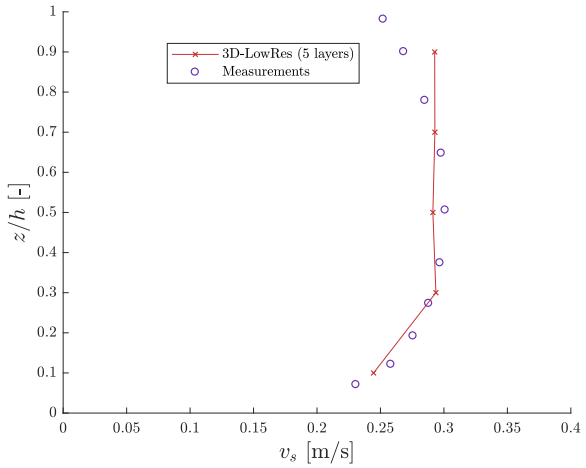

Figure 6.2: Case 1, streamwise velocity profile close to the outer bend side wall of the 145° section

Deformation of velocity profiles

The differences between the measured and modelled velocity profiles are not only caused by the turbulence phenomena, as indicated in Figure 6.2 for the region near the outer bend side wall. Near the channel axis deviations are observed as well. This is depicted in Figure 6.3 which shows the streamwise and transverse profiles found for the low-vertical-resolution 3D model, along with the measurements and 2DH representation:

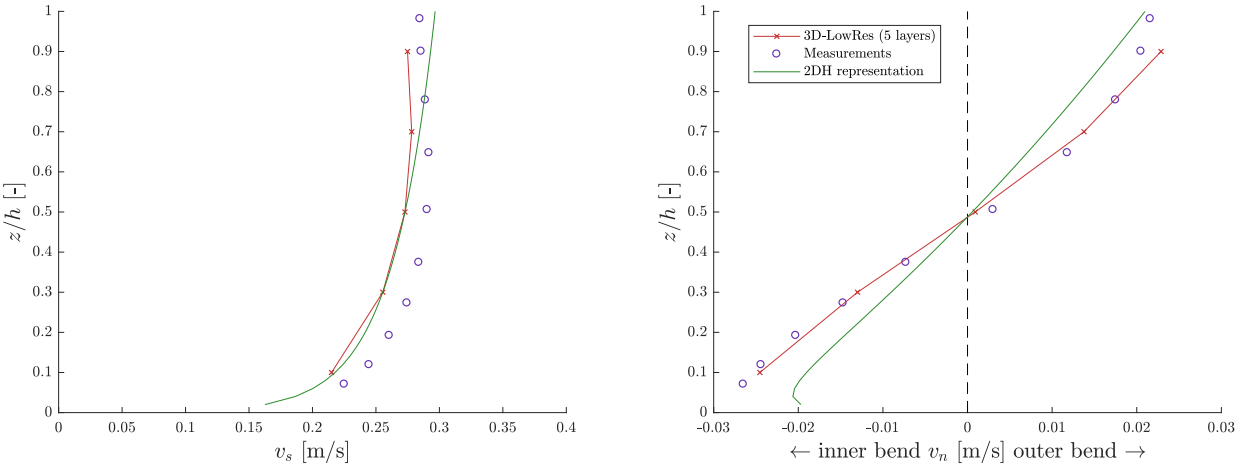

(a) Streamwise profile (b) Transverse profile

Figure 6.3: Case 1, flow velocity profiles at the channel axis of the 145° section

Figure 6.3a clearly indicates a flattening of the streamwise velocity profiles of 3D model results and measurements in comparison with the 2DH representation. The flattening should be distinguished from the distortion of the upper part of the profiles due to turbulence features as discussed previously. This can be argued based on the occurrence of the deformation in both the 3D model results and measurements, whereas the aforementioned turbulence features are only found in the measurements. Furthermore, the deformation can be found at the entire cross-section, whereas the turbulence related distortion in the measurements is mainly found near the side walls. The deformation of the streamwise velocity profiles can be recognized by a flattening of the entire profile throughout the bend, as seen in both 3D model results and the measurements for each of the three cases. The process of flattening does not occur simultaneously with the emergence of secondary flow but arises somewhat further along the bend, where the spiral flow is already prevailing. The flattening of the streamwise velocity profile is caused by interaction between the transverse and streamwise velocity profiles, explained in Section 2.2. As far as Case 1 is concerned, the 3D model appears to slightly underestimate the flattening in comparison with the measurements, as shown in Figure 6.3a. This can be attributed to the aforementioned underestimated momentum redistribution of the 3D model, which is the driving force of the flattening of the profiles. The 2DH representation of De Vriend (1976) does not account for this interaction at all, because the derivations are based upon a linear model. Other authors, among whom Blanckaert and De Vriend (2003) and Ottevanger et al. (2009) did account for this interaction in more extensive derivations.

The transverse velocity profiles of both the low-vertical-resolution 3D models and measurements deviate as well from the 2DH representation, as depicted in Figure 6.3b. The most striking difference is a general underestimation of the 2DH representation. The underestimation is caused by the 2DH parametrisation, which is explained hereafter in Section 6.3. Additionally, the shape of the transverse velocity profile of the measurements and 3D model also differs from the 2DH velocity profile. The distortion of the velocity profile can be recognized in Figure 6.3b by the relatively large negative velocities in a smaller lower part (about 45%) of the water column, and relatively small velocities in the larger upper part of the water column (about 55%). This results in larger transverse flow velocities near the bed than near the surface. The latter is explained by Blokland (1985) as a consequence of smaller streamwise velocities near the surface as shown in Figure 6.3a. This reduces the required centripetal acceleration near the surface, leading to relatively smaller transverse velocities. This phenomenon is observed for each of the three cases, albeit to varying degrees. The effect of this phenomena on the transverse velocity profiles is as well included in descriptions of Blanckaert and De Vriend (2003) and Ottevanger et al. (2009).

6.3. Spiral flow intensity

6.3.1. 2DH parametrisation

The spiral flow intensities are depicted for each of the cases in Figures 5.5, 5.12 and 5.19. These are of crucial importance for the bed shear stress direction of the new methodology using a low-vertical-resolution 3D model and the 2DH model, because these methodologies determine the transverse bed shear stress component based on the spiral flow intensity. The novelty of this research is the application of this methodology on 3D model results, and as well on measurement data as a reference. The most prevailing result for each of the cases is the significant underestimated spiral flow intensity of the 2DH model, in comparison to measurements and 3D model results. This leads to the suspicion that there are problems with the 2DH description for spiral flow, as formulated by Equation 3.1 in Section 3.3.2 based upon the work of De Vriend (1976). It should yield similar results to the 3D formulation as depicted in Equation 3.6 when all assumptions and simplifications of De Vriend (1976) described in Section 2.3 are justified. Apparently this is not the case, although most of the assumptions seem to be valid for the cases investigated in this research. Other authors, among whom De Vriend and Koch (1978), encountered the same problem. De Vriend and Koch (1978) question the validity of the vertical distribution of the eddy viscosity, which is assumed to be parabolic by, among others, Rozovskii (1957) and De Vriend (1976). The assumption of a parabolic eddy viscosity distribution underlies the formulations forming the basis of 2DH models, which are presented in Section 2.3. In reality, the vertical distributions appear to be flatter than the parabolic curve, which is confirmed by the measurements of Blokland (1985) on the same set-up as used for Case 1. An improvement might be found when a more realistic vertical distribution of the eddy viscosity would be used in analytical derivations underlying 2DH models.

Another specific issue found in the 2DH results of Case 1 is the unrealistically large magnitude of the spiral flow intensity close to the side walls. This is due to the fact that the underlying derivations are only valid at

some distance from the side walls. The 2DH model bases the intensity on the local flow velocity, which is still relatively large close to the side walls in case of a plain bed. As a result, the 2DH model computes unrealistically large intensities near the side walls. In reality, the spiral flow intensity is by definition zero at the side walls, and some distance from these walls is required for the intensity to reach full strength. This problem is not encountered for Cases 2 and 3, where the intensities gradually decrease toward the channel side walls. This is a result of the decreasing flow velocity toward the side walls, induced by a decreasing water depth.

6.3.2. 3D semi-parametrisation

The spiral flow intensities calculated with the 3D semi-parametrisation based on a low-vertical-resolution 3D model accord much better with the measurements than the 2DH model results. However, the non-inclusion of the outer bank cell in the 3D model results of Case 1 leads to a clear overestimation of the spiral flow intensity at the outer bend. This is due to the limiting effect of the outer bank cell on the spiral flow intensity, as found in the results based on the measurements. The limiting effect of the outer bank cell seems to grow throughout the bend. As far as Case 2 is concerned, two particular features are observed. At first, a significant overshoot is found for the measurements in the cross-section at which the secondary flow is still developing. This phenomenon is not represented at all by the 2DH and 3D models, which show a steadily decreasing growth of the intensity throughout the bend. The second feature of Case 2 is the shift of the highest spiral flow intensities toward the channel centre, whereas the peak of the intensity of the 3D model results shifts toward the side wall. This is largely comparable to Case 1, in which this behaviour is attributed to the outer bank cell. However, De Vriend and Koch (1978) explicitly noted that no outer bank cell was found in the measurements. The report does not contain transverse velocity profiles of the regions near the outer bend side wall. This gives rise to the suspicion that there might still be some influence of turbulence features near the outer bank side wall, which limit the local secondary flow intensity. However, this cannot be validated due to the lacking availability of measurement data.

6.4. Bed shear stress

6.4.1. Magnitude

The development of the bed shear stress magnitudes (figs. 5.6, E.17 and E.31) is comparable to the depth-averaged velocities, which are discussed in Section 6.2.1. However, the flattening of the streamwise velocity profiles as discussed in Section 6.2.2 also plays a role. The flattening of the velocity profiles can lead to relatively large flow velocities near the bed. As a consequence, the bed shear stress is larger than the value which would be found when assuming a logarithmic profile, which is implicitly assumed in the 2DH model. The results of Case 1 show that this probably plays a role in the measurement data, of which the profiles are generally more flattened than the 3D model results. Based on this, it can be concluded for Case 1 that the bed shear stress magnitudes computed by the 2DH and low-vertical-resolution 3D model are underestimated compared with the measurements. This might as well apply for Cases 2 and 3, but this cannot be proven due to lacking measurement data. When comparing the 2DH with the 3D model results for each of the three cases, the flattening of the streamwise velocity profiles of the 3D model results is clearly present. However, this appears to be of minor influence on the magnitude of the bed shear stresses. This leads to the suspicion that the flattening mainly affects the upper part of the velocity profiles, whereas the lower part is of importance for the bed shear stress. Within the context of this research, it can be concluded based on this information that the bed shear stress determination based upon the depth-averaged velocity barely differs from the determination based upon the near-bed velocity.

6.4.2. Direction

General

The bed shear stress angle deviation is the end point of the research. A comparison is made between the new methodology applied to the results of both a low-vertical resolution 3D model and measurements, and the conventional 2DH and 3D model approaches. The main challenge is finding a justified approach to validate the bed shear stress directions. In Section 2.3.3 notice is made of the far-reaching assumptions and simplifications made by De Vriend (1976) in obtaining the description for the bed shear stress direction, which is used in 2DH parametrisation and 3D semi-parametrisation. Other authors who tried to validate outcomes of mathematical models with experimental research, among whom Talmon et al. (1995), encountered several difficulties. This is due to the fact that the direction is not only determined by spiral flow, but as well by

bed slope effects. Furthermore, the formation of bed forms was a complicating factor in determining relations. Unfortunately, no measurement data about the bed shear stress directions was available for the cases investigated in this research.

Comparison with measurements
At first, a comparison is made in Chapter 5 between the outcomes obtained by applying the new methodology on both low-vertical-resolution 3D model results and measurement data, as found in Figures 5.7 and 5.13 in Sections 5.2.3 and 5.3.3. The outcomes based on the measurement data and 3D model results show a relatively good agreement, except for regions near the outer bend side wall. This is caused by the outer bank effects in the measurements which are not represented by the 3D model, as discussed in Sections 6.2.2 and 6.3. Another deviation connected with Case 2 is caused by the 3D model failing to represent the 'overshoot' of the spiral flow intensity, found just after the bend entrance.

The problems encountered with the 2DH method for determining the spiral flow intensity Section 6.3 directly affect the calculated bed shear stress direction. 2DH models significantly underestimate the bed shear stress angle deviation, ranging up to 35% in comparison with the measurements. Furthermore, the 2DH model clearly fails in predicting the bed shear stress angle deviation at Case 1, due to the erroneous distribution of the spiral flow intensity. However, this problem remains mostly limited to geometries with a rectangular cross-section.

Comparison with conventional methodologies
Second, a more detailed investigation is conducted to the new methodology using a low-vertical-resolution 3D model in Figures 5.8, 5.14 and 5.20 in Sections 5.2.3, 5.3.3 and 5.4.3. It is validated by a comparison with a reference case based on a high-vertical-resolution 3D model with 50 layers. This model might still slightly underestimate the angular deviation of the bed shear stress. However, within the context of this research, it is considered to be the best validation option available. The new methodology generally agrees well with the high-resolution reference case. It yields relatively accurate results, and thus takes away the need of high-vertical resolution models for accurate modelling of the bed shear stress angle deviation. A vertical resolution of 5 layers appears to be sufficient for most situations. Generally, it is found that the methodology leads to significant improvements in comparison with the conventional 2DH and 3D methodologies. The conventional 2DH methodology underestimates the bed shear stress deviation significantly in comparison with the new methodology, mainly due to the erroneous determination of the spiral flow intensity as explained in Section 6.3. The conventional 3D approach also significantly underestimates the angle in case of a low-vertical resolution 3D model, which can only be circumvented by using a computationally expensive high-vertical resolution model.

Nonetheless, the new methodology still deviates significantly with the high-vertical resolution 3D reference set-up for some scenarios. It is shown for Case 1 in Figure 5.8 in Section 5.2.3 that the new methodology underestimates the bed shear stress angle deviation at sections with developing flow by about 15%, although it agrees well for developed flow. The results of Case 2, as depicted in Figure 5.14 in Section 5.2.3, show that the deviations of the new methodology from to the reference set-up remain limited to an overestimation of about 15%, mostly at sections with developed flow. Lastly, when considering Case 3, some differences are found which can be mainly attributed to local disruptions. Apart from these, the new methodology performs relatively well, except for the 66° cross-section where the spiral flow decays. The new methodology severely overestimates the angle deviation by about 50% at this location. No attention was paid to areas with decaying spiral flow in Cases 1 and 2, because the available measurement data was limited to sections of developing and developed spiral flow. These results as summarized above indicate that the new methodology encounters issues in regions with developing and decaying spiral flow, whereas it performs well for sections with developed spiral flow. This is due to the relatively accurate agreement of the transverse velocity profile obtained in 3D model results in comparison with the shape of the 2DH profile derived by De Vriend (1976). This is confirmed by Figure 6.4 in which the normalized representative 2DH profile is fitted on the transverse velocity profile obtained from the 3D model results of Case 1:

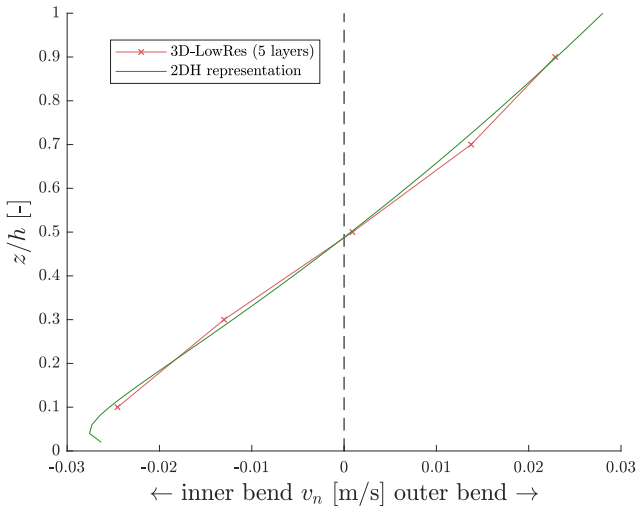

Figure 6.4: Case 1, transverse velocity profile at the 145° cross-section with a representative 2DH curve as used in the new methodology

Despite the good agreement, some small improvements could be made. However, a perfectly fitting profile cannot be found as the flow field differs per situation.

The issues encountered with developing and decaying spiral flow are due to the deviating transverse velocity profiles found at the associated cross-sections. This is confirmed by the transverse velocity profiles depicted in Appendices E.1.3, E.2.4 and E.3.4. This is explored in more detail in Figure 6.5, which shows illustrative examples for developing (pink), developed (red) and decaying (dark-red) spiral flow of a low-vertical-resolution 3D model:

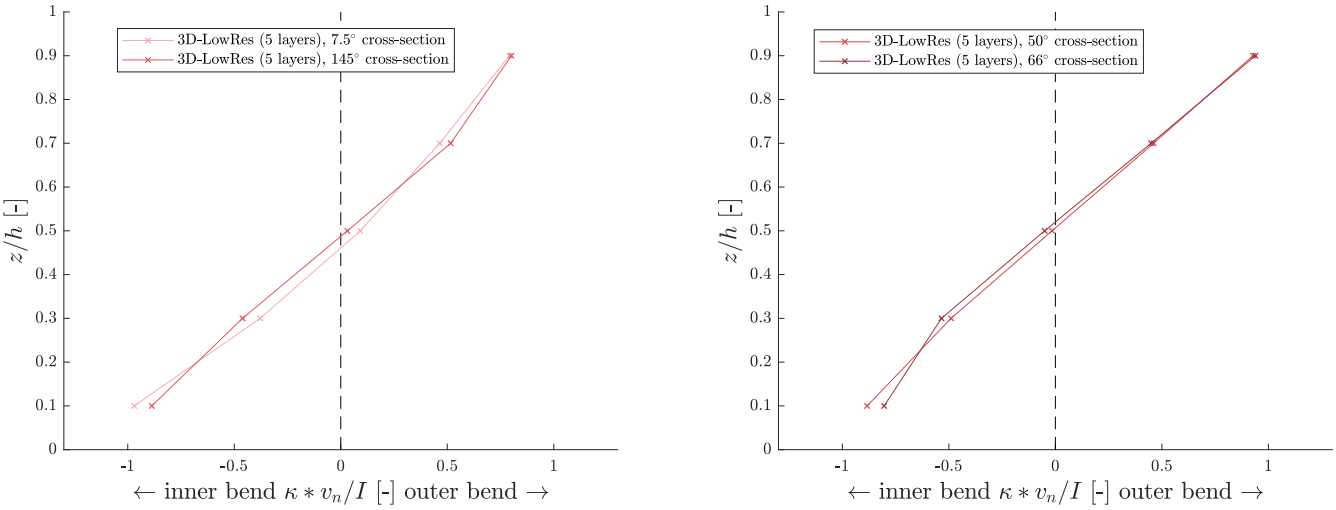

(a) Case 1, developing and developed spiral flow

(b) Case 3, developed and decaying spiral flow

Figure 6.5: Case 1 and 3, normalized transverse velocity profiles in developing, developed and decaying spiral flow (3D-LowRes)

Figure 6.5a shows that the transverse velocities are larger near the bed than near the surface in case of developing spiral flow. This is found for each of the three cases. The opposite is found in the section with decaying spiral flow of Case 3, as shown in Figure 6.5b. This shows that the transverse velocities near the bed decay faster than the entire transverse velocity profile. The deviation velocity profiles reveal the weakness of the new methodology based on calculation method A (as shown in fig. 3.5a in section 3.3.2), which implicitly assumes the shape of the representative velocity profile, shown in green in fig. 6.4. It was expected that calculation method B (fig. 3.5b) would cause an improvement, as it is only based on the bottommost part of the transverse velocity profile. However, it only yields a limited improvement. The new methodology using calculation method B still underestimates the angular deviation of the bed shear stress in comparison with a high-vertical-resolution reference case. This can be attributed to the inability of a low-vertical-resolution

3D model with an equidistant layering to capture processes very close the bed. As a reference, the transverse velocities of a high-vertical-resolution 3D model are shown in Figure 6.6, along with the measured profiles of Case 1:

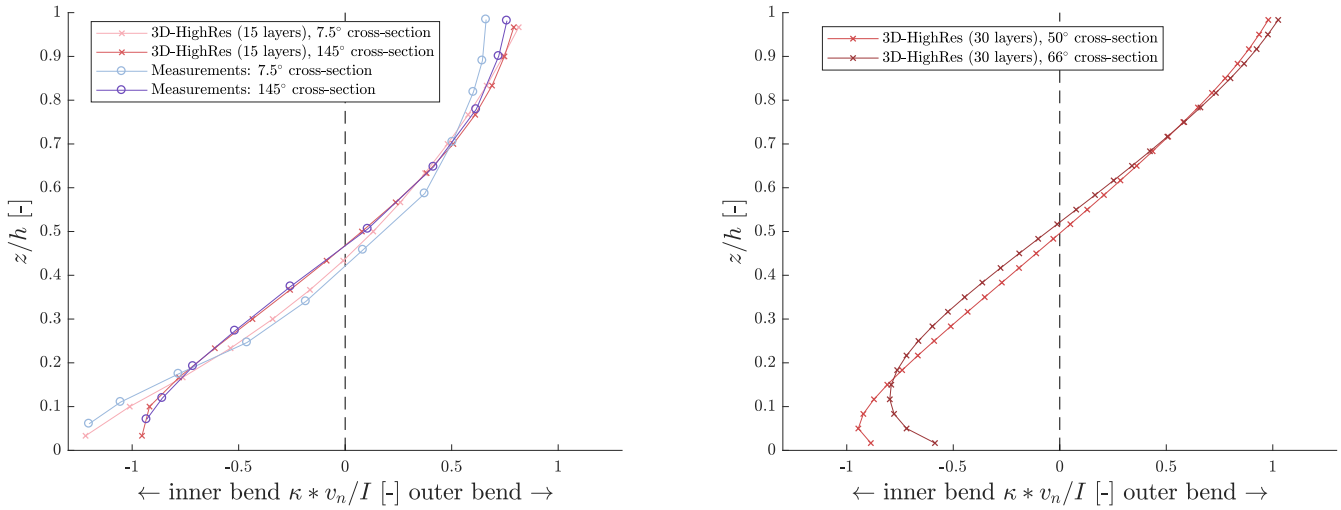

(a) Case 1, developing and developed spiral flow

(b) Case 3, developed and decaying spiral flow

Figure 6.6: Case 1 and 3, normalized transverse velocity profiles in developing, developed and decaying spiral flow (3D-HighRes)

Figure 6.6 shows that the deviations are much larger close to the bed than further away from the bed, as shown in Figure 6.5. A low-vertical-resolution 3D model is therefore only able to partially represent these deviations, which is the reason for the deviations of the new methodology from the high-vertical-resolution reference case. The issue can be solved partially by using a model set-up with a finer resolution near the bed. Another solution would be the development of a range of normalized secondary flow velocity profiles, in which profiles are included which are more suitable for developing and decaying spiral flow.

The underlying reason for the deformation of the transverse velocity profiles in case of developing or decaying spiral flow is given by Kalkwijk and Booij (1986). It is believed to be caused by the relatively large effect of the driving force on the transverse velocity profile, due to the lower flow velocity close to the bed. As a result, changing flow conditions will sooner affect the near-bed transverse velocities.

Besides the issue discussed above for developing and decaying spiral flow, some other reasons were found as well for the deviating results of the new methodology. The combined effect of these items varies per situation, and therefore differs among the cases. The possible issues are listed below:

- Low-vertical resolution models show a somewhat larger streamwise bed shear stress magnitude, as seen in Figure D.6. This leads to smaller bed shear stress angle deviations, in case of an unchanged transverse bed shear stress component. This might cause the low-vertical resolution models to underestimate the bed shear stress angle deviation to some extent.

- Section 6.1 points out that low-vertical resolution models underestimate the transverse velocities at sections with developing flow, as depicted in Figure 6.1a. At the same time, low-vertical resolution models appear to overestimate the transverse velocities along the outer bend of sections with developed flow, as indicated in Figure 6.1b. This is an additional cause for the new methodology to underestimate the bed shear stress angle deviation at sections with developing flow, and the overestimation at sections with developed flow.

7

Conclusion and Recommendations

7.1. Conclusion

The conclusion is built up out of answers found to the research questions, derived from the research objective as presented in Section 1.3.

7.1.1. Research objective and questions

The objective of the research is to explore a new methodology in the context of the shortcomings of conventional 2DH and 3D models. The research aim was to develop and assess a new methodology using low-vertical-resolution 3D models, supplemented by a modification. Based on the objectives two main research questions were formulated for this research:

1. *How do the simplifications and parametrisations applied to conventional 2DH and 3D models affect the representation of spiral flow and the influence of spiral flow on the bed shear stress?*

2. *How can the bed shear stress vector be determined more accurately in a low-vertical-resolution 3D model?*

7.1.2. Research question 1

1.1 *What are the additional parametrisations in 2DH models required for simulating the effects of spiral flow, and how are these derived?*

Due to the loss of three-dimensional phenomena as a result of depth-averaging, parametrisations are included in models in order to represent the effects of spiral flow. These parametrisations are based on the work of De Vriend (1976), who obtained the derivations from a first order mathematical system based on the normalized RANS equations. A detailed description on the assumptions underlying the mathematical system is given in Section 2.3.3. The descriptions for the influence of spiral flow on the bed shear stress are derived using a mixing length model assuming a parabolic eddy viscosity distribution. The parametrisations are derived for a channel with a fixed curvature and constant width. Furthermore, the applicability is limited to the channel centreline, as no account is taken for side wall effects.

1.2 *How is the accuracy of 3D and 2DH models affected by the applied simplifications and parametrisations, considering both idealized and more arbitrary geometries?*

Three-dimensional models are able to capture the flow pattern relatively well for the mildly curved bends investigated in this research. The agreement with the measurements is the largest near the channel centreline, whereas the strongest deviations can be found near the side walls. Based upon the scarce measurement data available for geometries without vertical side walls, it can be concluded that the deviations are still present for these geometries, but to a lesser extent. As far as geometries based on real river sections are concerned, it is seen that spiral flow effects are of subordinate importance outside the main channel bounds, due to the dominance of local flow effects around groynes and other obstacles. Furthermore, 3D models seem to underestimate the

momentum redistribution caused by spiral flow at stages of developing flow, leading to an underestimation of the outward velocity shift of streamwise velocities as found in open channel bends. Another related consequence is the underestimation of the process of flattening of the streamwise velocity profile, and hence the flow velocities near the bed.

Depth-averaged models face more issues in representing spiral flow. This is especially of relevance for cases in which momentum redistribution due to spiral flow plays a large role. This process is not resolved in depth-averaged models. In this research, it was found that this process plays a much smaller or even negligible role for large-scale river with a developed bed topography. The largest problem of depth-averaged models is caused by the parametrisation representing the effects of spiral flow on the bed shear stress. It is found that the deviation of the bed shear stress angle from the main flow direction is significantly underestimated. This is believed to be caused by the assumption of a parabolic eddy viscosity distribution, which underlies the parametrisation of the transverse bed shear stress component.

7.1.3. Research question 2

The second question is subdivided as follows:

2.1 *What kind of methodology is required to enable a more accurate description of the bed shear stress vector in a low-vertical-resolution 3D model?*

The new methodology presented in this thesis, referred to as *3D-LowRes-SemiPar*, circumvents the resolution problem of low-vertical-resolution 3D models by supplementing the model with a semi-parametrisation. The new methodology builds on the work of De Vriend (1976), who developed parametrisations based on analytical derivations from a simplified mathematical model. It is based on the spiral flow intensity, which is in essence a description for the relative magnitude of the secondary flow velocity profile. The spiral flow intensity can be determined on the basis of a normalised secondary flow profile derived by De Vriend (1976). The first calculation method presented in this research is based on the entire secondary flow profile, the second method is based on solely the bottommost part. The latter is a refinement of the method in order to obtain more accurate results, as the bed shear stress only depends on the near-bed flow. De Vriend (1976) derived a relation for the transverse bed shear stress component based on the spiral flow intensity. This relation is obtained by determining the angular deviation of the combined velocity vector down to the bed, at which the velocities equal zero. This allows the calculation of the bed shear stress direction.

2.2 *What is the performance of this new methodology in describing the bed shear stress vector, compared to conventional 2DH and high-vertical-resolution 3D models, for both idealized and more complex geometries?*

A part of the advantage of the new methodology is due to the aforementioned better performance of 3D models in comparison with 2DH models. With regard to conventional 3D models, the new methodology allows a more accurate determination of the bed shear stress direction. It enables modelling with low-vertical-resolution models at a comparable accuracy of model with a much higher resolution. This is especially the case for sections with developed spiral flow, due to the close agreement of the normalized profile of De Vriend (1976) with the transverse flow velocity profile found in the model. Problems are encountered for sections of the bend at which the spiral flow is either developing or decaying. This is due to the disproportional adjustment of the transverse velocity profile to spiral flow. It is found for developing secondary flow that the effects of spiral flow are prevailing near the bed and, by contrast, fade more rapidly near the bed in case of decaying secondary flow. This leads to deviations of the results obtained with the new methodology from a high-vertical-resolution reference case. This is due to two reasons. Firstly, a discrepancy is found between the transverse velocity profiles observed and the normalized profile of De Vriend (1976), implicitly underlying the first calculation method of the new methodology. And secondly, a low-vertical-resolution 3D model with an equidistant layering is not able to capture the processes very close to the bed. As a result, the second calculation method only yields a limited improvement to the first calculation method.

Furthermore, although not tested during this research, it is expected that the new methodology will yield poor results in the case of sudden bed variations in the streamwise direction, and to a lesser extent in the transverse direction.

7.2. Recommendations

7.2.1. Main recommendations

The recommendations for further use can be divided into two parts. Firstly, there is the added value of using 3D models instead of 2DH models. This is due to the capability of 3D models to solve the spiral flow, and hence account for the redistribution of streamwise momentum. Furthermore, a 3D model is more accurate near groynes and other obstacles. It depends from case to case whether these deviations play a large role. Secondly, a 2DH model underestimates the angular deviation of the bed shear stress. As a consequence, it is likely to underestimate the pace of morphological developments. It is therefore advised to validate the performance of 2DH with a reference 3D model set-up, in order to assess the impact of the weaknesses of a 2DH model. In case these play a large role, it is advised to reconsider the choice for a 2DH model.

The second recommendation is about the performance of the new methodology applied on low-vertical-resolution 3D models in comparison conventional high-vertical-resolution models. The new methodology gives a proof of concept that it is feasible to use low-vertical-resolution 3D models, yielding significant savings in computational expenses. However, the new methodology still has some issues around obstacles and in sections with developing and decaying spiral flow. These are partially inherently linked to the new methodology, and partially solvable by using non-equidistant model set-ups. The new methodology can be further developed by using additional normalized profiles adapted for developing or decaying spiral flow.

7.2.2. Recommendations for further research

- The research was limited to hydrodynamic computations, whereas the final goal is to enable more accurate morphodynamic computations. Within the context of this research, it is impossible to assess the effect of the new methodology on the morphodynamics, because the results are obtained by post-processing the output data of the hydrodynamic module of Delft3D in MATLAB. The added value of the new methodology can be further assessed by including the new methodology in the code of Delft3D, and subsequently carrying out morphodynamic computations.

- The transverse velocity profile found in the model results and measurements deviates slightly from the normalized profile of De Vriend (1976) in case of developed spiral flow. Other authors, such as Blanckaert and De Vriend (2003) improved this profile by accounting for the interaction between main and secondary flow. This might lead to some improvement, but this is not expected to be of large significance. In this research, it is shown that the largest mismatch between the measured or modelled profile and the normalized profile is found in sections with developing or decaying flow. Kalkwijk and Booij (1986) made notice of this phenomenon, but considered it to be justified to neglect it. This seems to be a rather crude assumption based on the results found in this research. Both conventional 2DH models and the new methodology could be improved if the distortion of the profile is taken into account.

- The deficient measurement data available for Case 2 makes it difficult to determine the outer wall effects. Although it is mentioned by De Vriend and Koch (1978) that no outer bank cell is present, it seems that there are still significant turbulence-related features near the outer wall. In case the raw measurement data could be obtained, it would be interesting to research this phenomenon, as it did not appear to be a point of focus in the report of De Vriend and Koch (1978).

- Within the context of this research, it seems that the effect of momentum redistribution is minimal for real-world rivers with a developed geometry. However, this is only based on the results of one modelled case. More thorough research would be required to validate this suspicion.

- It is shown for Case 1 that low-vertical-resolution 3D models perform relatively well in comparison with their high-vertical-resolution counterparts, apart from a smaller level of detail. However, this has not been validated for the other cases.

- Building on the previous statement, there might as well be other possibilities for low-vertical resolution 3D models. An example is modelling of suspended sediment transport with these models, yielding

considerable savings in required computational resources.

- Only a limited number of cases is investigated in the context of this research. Despite the mutual differences between the case, each of these can be considered as a mildly curved bend. In comparison with depth-averaged models, the new methodology is expected to be of advantage for more complex geometries, especially when three-dimensional flow phenomena play a large role. The performance of the methodology could be validated when modelling more geometries, such as listed below:
  - a river bend section with a widening or narrowing
  - a braiding river
  - a river bend with a confluence or bifurcation
  - a sharply curved bend
- Furthermore, only a single discharge was modelled for each case in order to compare the outcomes with available measurement data. The latter is of importance for investigating the performance of models in general. However, the performance of the new methodology can as well be validated using high-resolution set-ups of the same 3D model. More insight into the performance and consistency of the methodology could be gained when carrying out a sensitivity analysis by varying the input parameters, such as the discharge.
- The angular deviations of the bed shear stress calculated using the new methodology were compared with the flow direction of the bottommost layer of a 30 or 50-layer 3D model set-up. Although it is thought to be the best reference available for this research, it can be considered to be a rather crude. It would be interesting to research the directions of the bed shear stress and near-bed flow in case of both smooth and rough beds, in order to validate the model results and the analytical descriptions of De Vriend (1976) underlying the new methodology.
- The new methodology has only been applied to models with an equidistant vertical layering. It is expected that the new methodology can be improved by applying a more detailed grid near the bed, but it was not possible to test and validate this.
- Within the context of this research, no detailed assessment has taken place into the required computation times of the 2DH and 3D models, which is a crucial factor in river engineering practice. It is obvious that reducing the vertical resolution of a 3D model reduces calculation times, but this was not investigated thoroughly. Further research is required to obtain more insight into this aspect.

Bibliography

[1] W. van Balen. *Curved open-channel flows*. PhD thesis, Delft University of Technology, 2010.

[2] W. van Balen, W. S. J. Uijttewaal, and K. Blanckaert. Large-eddy simulation of a curved open-channel flow over topography. *Physics of Fluids*, 22(7):1–18, 2010. ISSN 10706631. doi: 10.1063/1.3459152.

[3] J. C. Bathurst, C. R. Thorne, and R. D. Hey. Direct measurement of secondary currents in river bends. *Nature*, 269:504 – 506, 1977.

[4] L. van Bendegom. Some consideration on river morphology and river improvement (in Dutch). *Ingenieur*, 59(4):B1–B11, 1947.

[5] K. Blanckaert. Saturation of curvature-induced secondary flow , energy losses , and turbulence in sharp open-channel bends : Laboratory experiments , analysis , and modeling. 114:1–23, 2009. doi: 10.1029/2008JF001137.

[6] K. Blanckaert. Hydrodynamic processes in sharp meander bends and their morphological implications. *Journal of Geophysical Research: Earth Surface*, 116(1):1–22, 2011. ISSN 21699011. doi: 10.1029/2010JF001806.

[7] K. Blanckaert and W. H. Graf. Momentum Transport in Sharp Open-Channel Bends. *Journal of Hydraulic Engineering*, 130(3):186–198, 2004. ISSN 0733-9429. doi: 10.1061/(ASCE)0733-9429(2004)130:3(186).

[8] K. Blanckaert and H. J. de Vriend. Nonlinear modeling of mean flow redistribution in curved open channels. *Water Resources Research*, 39(12):n/a–n/a, 2003. ISSN 00431397. doi: 10.1029/2003WR002068.

[9] K. Blanckaert and H. J. de Vriend. Secondary flow in sharp open-channel bends. *Journal of Fluid Mechanics*, 498:353–380, 2004. ISSN 0022-1120. doi: 10.1017/S0022112003006979.

[10] K. Blanckaert, A. Duarte, Q. Chen, and A. J. Schleiss. Flow processes near smooth and rough (concave) outer banks in curved open channels. *Journal of Geophysical Research F: Earth Surface*, 117(4):1–17, 2012. ISSN 01480227. doi: 10.1029/2012JF002414.

[11] T. Blokland. Turbulentiemetingen in een gekromde goot. Master's thesis, 1985.

[12] R. Booij. Measurements and large eddy simulations of the flows in some curved flumes. *Journal of Turbulence*, 4(March 2015):37–41, 2003. ISSN 1468-5248. doi: 10.1088/1468-5248/4/1/008.

[13] R. Booij and Joh. G. S. Pennekamp. Improved simulation of main flow and secondary flow in a curved open channel. Technical Report 1, Delft Univ. of Techn., Dept. of Civil Engrg., Lab. of Fluid Mech., Delft, 1984.

[14] M. J. Boussinesq. Mémoire sur l'influence des frottements dans les mouvements réguliers des fluides. *Journal de mathématiques pures et appliquées*, 13(2e série, tome 13):377–424, 1868.

[15] Deltares. *Delft3D-FLOW User Manual*. 2017.

[16] Deltares. *D-FLOW Flexible Mesh Technical Reference Manual*. 2017.

[17] A. Einstein. Die Ursache der Mäanderbildung der Flußläufe und des sogenannten Baerschen Gesetzes. *Die Naturwissenschaften*, 14(11):223–224, 1926.

[18] D. A. Ervine, K. Babaeyan-Koopaei, and R. H. J Sellin. Two-Dimensional Solution for Straight and Meandering Overbank Flows. *Journal of Hydraulic Engineering*, 126(September):653–669, 2000.

[19] P. Ph. Jansen, L. van Bendegom, J . van den Berg, M. de Vries, and A. Zanen. *Principles of River Engineering*. Delftse Uitgevers Maatschappij bv., Delft, 1979. ISBN 90-6562-146-6.

[20] J. P. Th. Kalkwijk and R. Booij. Adaptation of secondary flow in nearly-horizontal flow. *Journal of Hydraulic Research*, 24(1):19–37, 1986. ISSN 0022-1686. doi: 10.1080/00221688609499330.

[21] F. J. Koch. Fully three-dimensional computations of steady turbulent flow in curved channels with a rectangular cross-section. Technical report, 1981.

[22] F. R. Menter. Two-equation eddy-viscosity turbulence models for engineering applications. *AIAA Journal*, 32(8):1598–1605, aug 1994. ISSN 0001-1452. doi: 10.2514/3.12149.

[23] K. W. Olesen. *Bed topography in Shallow River Bends*. PhD thesis, Delft University of Technology, 1987.

[24] W. Ottevanger. *Modelling an parameterizing the hydro- and morphodynamics of curved open channels*. PhD thesis, Delft University of Technology, 2013.

[25] W. Ottevanger, K. Blanckaert, and W. S. J. Uijttewaal. Finite difference modelling of the vertical flow structure in strongly curved shallow channel flow. pages 1–20, 2009.

[26] L. Prandtl. Über die ausgebildete Turbulenz (investigations on turbulent flow). *Z. Angew. Math. Mech*, 5: 136–139, 1925. doi: 10.1007/978-3-662-11836-8_60.

[27] W. Rodi. Turbulence Modeling and Simulation in Hydraulics : A Historical Review. *Journal of Hydraulic Engineering*, 143(5):1–20, 2017. ISSN 19437900. doi: 10.1061/(ASCE)HY.1943-7900.0001288.

[28] I. L. Rozovskii. Flow of Water in Bend of Open Channel. Technical report, Institute of Hydrology and Hydraulic Engineering, Academy of Sciences of the Ukrainian SSR, Kiev, 1957.

[29] A. van Sabben. Sharp bend flow: Comparison of Delft3D-FLOW with LES and measurements for sharp bends. Master's thesis, 2010.

[30] R. H. J. Sellin. A laboratory investigation into the interaction between flow in the channel of a river and that of its flood plain. *La Houilte Blanche,*, (7):793–801, 1964.

[31] K. Shiono and Y. Muto. Complex flow mechanisms in compound meandering channels with overbank flow. *Journal of Fluid Mechanics*, 376:S0022112098002869, 1998. ISSN 00221120. doi: 10.1017/S0022112098002869.

[32] N. Struiksma, K. W. Olesen, C. Flokstra, and H. J. de Vriend. Bed deformation in curved alluvial channels. *Journal of Hydraulic Research*, 23(1):57–79, 1985. ISSN 0022-1686. doi: 10.1080/00221688509499377.

[33] A. M. Talmon, N. Struiksma, and M. C. L. M. Van Mierlo. Laboratory measurements of the direction of sediment transport on transverse alluvial-bed slopes. *Journal of Hydraulic Research*, 33(4):495–517, 1995. ISSN 0022-1686. doi: 10.1080/00221689509498657.

[34] J. Thomson. Flow Round River bends. *Proceedings of the Institute of Mechanical Engineers*, (August): 456–461, 1879.

[35] W. S. J. Uijttewaal. *Lecture notes 'Turbulence in hydraulics', CT5312*. 2003.

[36] H. J. de Vriend. A mathematical model of steady flow in curved shallow channels. Technical report, TU Delft, Department of Hydraulic Engineering, 1976.

[37] H. J. de Vriend. Developing laminar flow in curved rectangular channels. *Report no. 6-78*, 1978.

[38] H. J. de Vriend. Flow Measurements in a Curved Rectangular Channel. (9):80, 1979.

[39] H. J. de Vriend. *Steady Flow in Shallow Channel Bends*. PhD thesis, Delft University of Technology, 1981.

[40] H. J. de Vriend and J. P. Th. Kalkwijk. Computation of the flow in shallow river bends. Technical report, Delft University of Technology, Delft, 1980.

[41] H. J. de Vriend and F. J. Koch. Flow of water in a curved open channel with a fixed plane bed. Technical report, 1977.

[42] H. J. de Vriend and F. J. Koch. Flow of water in a curved channel with a fixed uneven bed. Technical Report November, 1978.

[43] E. Waite. A River Runs Through (photograph), 2017.

Appendices

A

Reynolds-averaging of the Navier-Stokes equations

A.1. Boussinesq hypothesis

Open channel flows as found within hydraulic engineering practice are virtually always turbulent, which can also be concluded from large Reynolds numbers found in these flows. As stated by Rodi (2017), turbulent fluctuations contribute significantly to the transport of momentum, heat and mass. Hence, the phenomenon of turbulence influences, among other things, the flow development, acting forces, losses and sediment transport. In the RANS equations the turbulent fluctuations are averaged out. This has led to the appearance of additional terms in the form $\rho\overline{v_i' v_j'}$ $(i, j = s, n, z)$, which are generally called turbulent or Reynolds stresses. Rodi (2017) describes these terms as correlations of fluctuating velocities which act as stresses on the fluid, in addition to the always present viscous stresses. Due to the appearance of these stresses, the system of equations is no longer closed anymore. Solving the system of equations requires a closure model for the Reynolds stresses. The first steps in order to achieve this were taken by Boussinesq (1868), who proposed to include the effect of turbulence by complementing or replacing the molecular viscosity term η by an artificial viscosity ν_t, known as the eddy viscosity. The latter is generally much larger than the molecular viscosity. In essence, the eddy viscosity will depend on the gradient of the mean velocity using this approach. This characteristic makes the eddy viscosity, in contradiction to the molecular viscosity, a flow property rather than a fluid property (Rodi, 2017). An important drawback of this method is mentioned by Blokland (1985), who states that the methodology of linking the eddy viscosity to the local flow gradient is essentially incorrect, due to the fact that turbulence is not just a local phenomenon. The concept described above is commonly referred to as the Boussinesq hypothesis. When applying this hypothesis, all correlations of fluctuating velocities ($\rho\overline{v_i' v_j'}$) are replaced by adding an eddy viscosity ν_t term.

A.2. Closure models

The Boussinesq hypothesis in itself is not enough for solving the RANS equations. Additionally, a turbulence model is required for calculating the eddy viscosity. The eddy viscosity is defined to be related to the local state of turbulence and is unknown a priori (Rodi, 2017). Multiple turbulence closure models have been developed by several researchers. The paper written by Rodi (2017) gives an overview of the use of RANS models in hydraulic engineering. He states that most hydraulic engineering calculations are still carried out using linear eddy viscosity models. In other words, the relation between the velocity gradients and turbulent stresses is linear. Rodi (2017) states that the simplest approach is using a constant eddy viscosity for which the value is prescribed empirically, which is considered to be only suitable for large-water body calculations. A more refined method is the mixing-length model developed by Prandtl (1925). This model relates the eddy viscosity to the local mean velocity gradients and an empirically prescribed mixing length. However, Rodi (2017) states the determination of the mixing length is problem dependent, and therefore especially difficult for complex geometries. Despite this drawback, it is mentioned that this simple and robust, and therefore still used. The problem of defining a mixing length scale can be circumvented by applying so-called two-equation models. It is explained that in addition to the k-equation for the velocity scale, a second transport equation is solved for

determining the length scale. The well-known $k-\epsilon$ model is based on this principle and widely applied within computational fluid dynamics software. Rodi (2017) describes that this model is considered to be applicable to a wide variety of flows with reasonable success. Nevertheless, he mentions that the model performs unsatisfactory in flows with an adverse pressure gradient, or flows in which the anisotropy of turbulence or streamline curvature play an important role. Another problem is the dominance of viscous stresses near the channel walls. Low-Reynolds-number versions have been developed which account for this by near-wall damping functions. These models require a detailed resolution near the walls which is unfavourable form a numerical point of view (Rodi, 2017). Finally, Rodi (2017) mentions the $k-\omega$ which is being used increasingly in modelling practice. He states that the length scale is calculated with the turbulence frequency, rather than the dissipation rate in $k-\epsilon$ models. The conclusion follows that this model performs better near the walls, but can be excessively sensitive to the chosen boundary conditions for ω. Menter (1994) developed a model which uses both approaches. His model (SST) makes use of the $k-\omega$ model near the walls, and the $k-\epsilon$ model away from the walls. Rodi (2017) states that this model has become increasingly preferred within turbulence modelling practice.

B

Mathematical model of De Vriend (1981)

This appendix presents the RANS equations forming the basis of the derivations of De Vriend (1981). The Reynolds stresses are related to the rate-of-strain tensor of the time-averaged flow by means of the scalar ν_t, the eddy viscosity. Parameter A describes the combined viscosity, existing of both the molecular (η) and eddy (ν_t) viscosity. In the following equations the overbar is omitted for the time-averaged quantities v_Φ, v_R and v_z.

$$v_\Phi \frac{\partial v_\Phi}{\partial \Phi} + v_R \frac{\partial v_\Phi}{\partial R} + v_z \frac{\partial v_\Phi}{\partial z} + \frac{v_\Phi v_R}{R_c} = -\frac{1}{\rho}\frac{\partial p}{\partial \Phi} + \frac{A}{\rho}\left(\nabla^2 v_\Phi - \frac{v_\Phi}{R_c^2} + \frac{2}{R_c}\frac{\partial v_R}{\partial \Phi}\right) + \frac{1}{\rho}\left[2\frac{\partial A}{\partial \Phi}\left(\frac{\partial v_\Phi}{\partial \Phi} + \frac{v_R}{R_c}\right) + \frac{\partial A}{\partial R}\left(\frac{\partial v_R}{\partial \Phi} + \frac{\partial v_\Phi}{\partial R} - \frac{v_\Phi}{R_c}\right) + \frac{\partial A}{\partial z}\left(\frac{\partial v_\Phi}{\partial z} + \frac{\partial v_z}{\partial \Phi}\right)\right] \tag{B.1}$$

$$v_\Phi \frac{\partial v_R}{\partial \Phi} + v_R \frac{\partial v_R}{\partial R} + v_z \frac{\partial v_R}{\partial z} - \frac{v_\Phi^2}{R_c} = -\frac{1}{\rho}\frac{\partial p}{\partial R} + \frac{A}{\rho}\left(\nabla^2 v_R - \frac{v_R}{R_c^2} + \frac{2}{R_c}\frac{\partial v_\Phi}{\partial \Phi}\right) + \frac{1}{\rho}\left[\frac{\partial A}{\partial \Phi}\left(\frac{\partial v_R}{\partial \Phi} + \frac{\partial v_\Phi}{\partial R} - \frac{v_\Phi}{R_c}\right) + 2\frac{\partial A}{\partial R}\frac{\partial v_R}{\partial R} + \frac{\partial A}{\partial z}\left(\frac{\partial v_R}{\partial z} + \frac{\partial v_z}{\partial R}\right)\right] \tag{B.2}$$

$$v_\Phi \frac{\partial v_z}{\partial \Phi} + v_R \frac{\partial v_z}{\partial R} + v_z \frac{\partial v_z}{\partial z} = -\frac{1}{\rho}\frac{\partial p}{\partial z} - g + \frac{A}{\rho}\nabla^2 v_z + \frac{1}{\rho}\left[\frac{\partial A}{\partial \Phi}\left(\frac{\partial v_\Phi}{\partial z} + \frac{\partial v_z}{\partial R}\right) + \frac{\partial A}{\partial R}\left(\frac{\partial v_z}{\partial R} + \frac{\partial v_R}{\partial z}\right) + 2\frac{\partial A}{\partial z}\frac{\partial v_z}{\partial z}\right] \tag{B.3}$$

In which:

$$\nabla^2 = \frac{\partial^2}{\partial \Phi^2} + \frac{\partial^2}{\partial R^2} + \frac{1}{R_c}\frac{\partial}{\partial R} + \frac{\partial^2}{\partial z^2} \tag{B.4}$$

C

Model set-up of Case 3

Figure C.1: Case 3, location of the area of interest

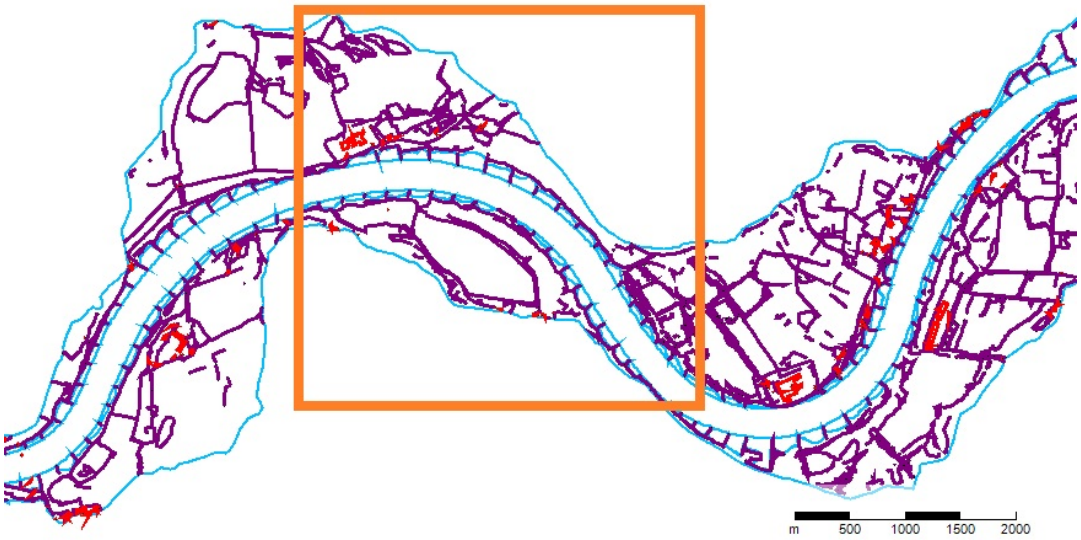

Figure C.2: Case 3, location of the area of interest with modelling components

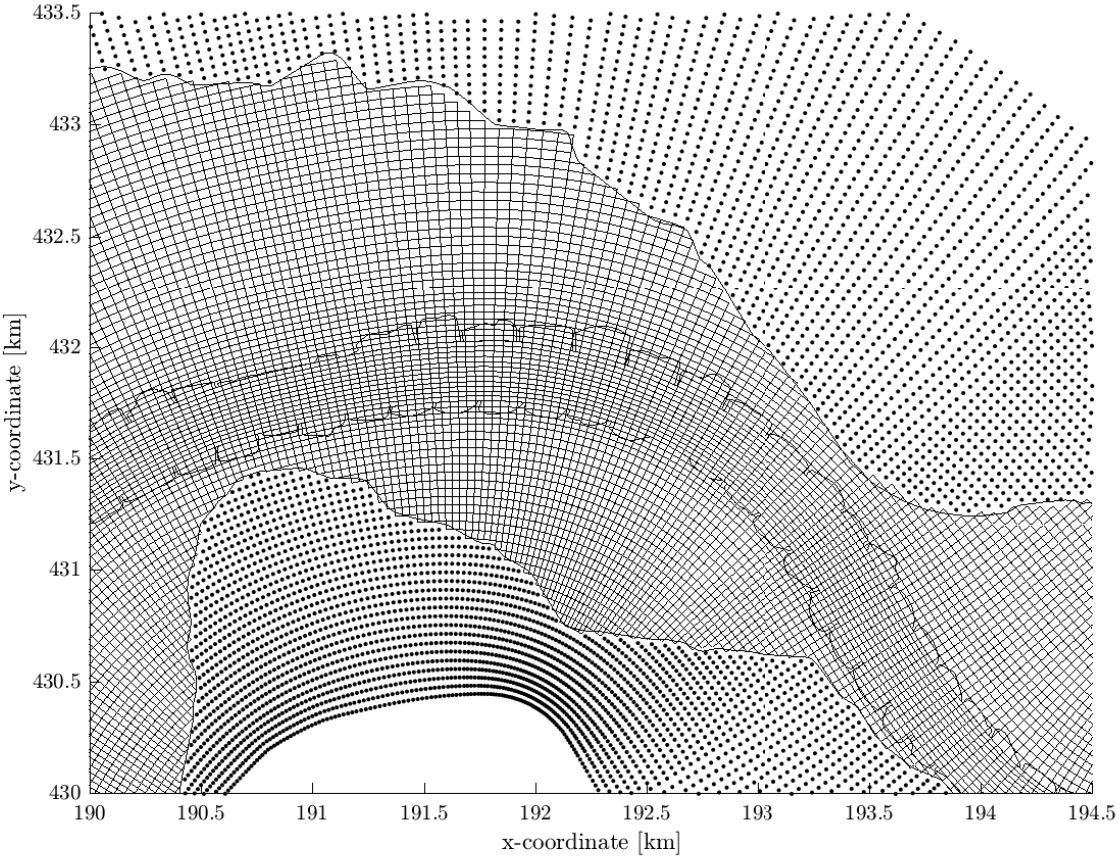

Figure C.3: Case 3, computational grid of the area of interest

D

Methodology review

D.1. Hydrodynamics

3D model accuracy for varying vertical resolution

The performance of the 3D model is tested for a varying number of layers in the vertical. Figure D.1 shows the results for runs with 3, 5, 15 layers for the 145° cross-section with fully developed spiral flow. In Appendix E.1.4 one can find as well the velocities at the straight flow (-1 m) and 15° cross-sections (figs. E.12 to E.14). Besides the smaller level of detail, some small differences can be observed. In the cross-section with developing flow (fig. E.13) one can observe that low-resolution set-ups slightly underestimate the transverse velocities in regions with developing flow. Other observations are were carried out for the 145° cross-section (fig. D.1) with fully developed flow, in which an overestimation of transverse velocities is observed in low-resolution set-ups, particularly in outer bend regions. Other remarkable differences are the overestimation of streamwise velocities at the inner bends and an underestimation at the outer bend. This leads to the suspicion that low-resolution models have small difficulties with reproducing the momentum redistribution in curved flow.

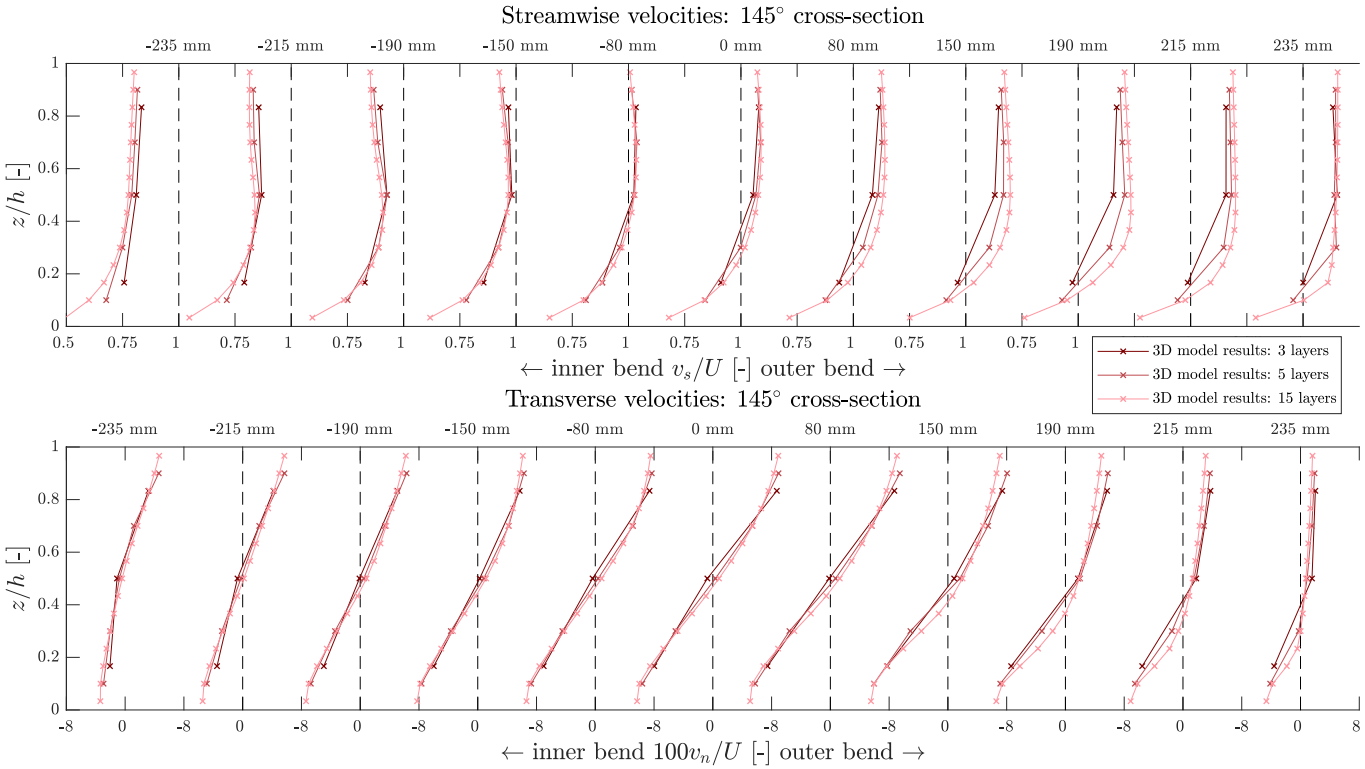

Figure D.1: Case 1, flow velocities at the 145° cross-section

D.2. Spiral flow intensity

Calculation methods

Multiple calculation methods were explored for determining the spiral flow intensity based on the transverse velocity profiles in Appendix D.2, using the methods explained in Figures 3.4 and 3.5 in Section 3.3.2. The performance of each of the four approaches is tested on case 1. As observed in Appendix D.1, the hydrodynamics did not differ much for high and low-vertical-resolution models (fig. D.1). The next step is testing whether the four methods are consistent with a varying number of layers used in the model. The results are depicted in Figure D.2a at the channel axis, and Figure D.2b for the cross-section averaged value. Figure D.3 shows the performance of the various approaches at the 145° cross-section of the flume for a model with 4 and 5 layers.

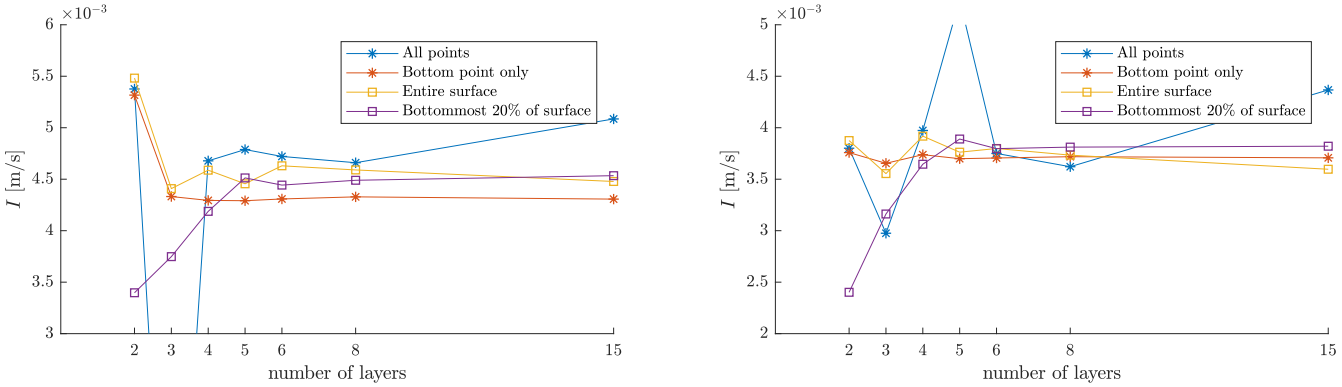

(a) At the channel axis (b) Cross-section averaged

Figure D.2: Case 1, spiral flow intensity at the 145° cross-section, dependency on the vertical resolution (number of layers)

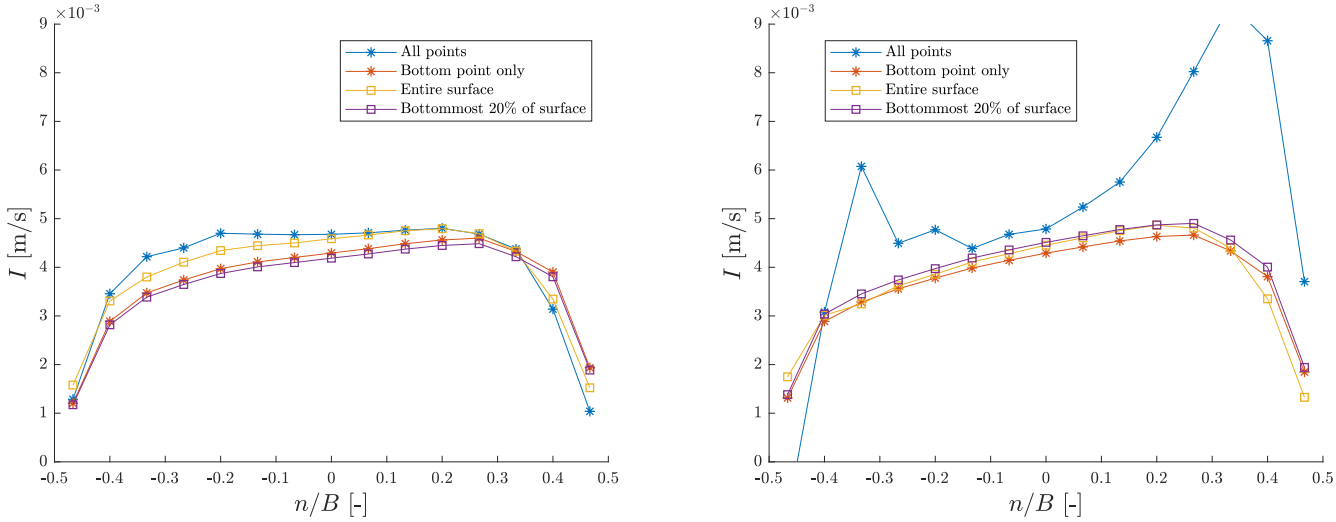

(a) 4 layer model set-up (b) 5 layer model set-up

Figure D.3: Case 1, spiral flow intensity at the 145° cross-section, performance of calculation methods

The following can be observed:

- The method using the determination based on all velocity points shows large errors for models with an odd number of layers. This is also clearly visible in Figure D.3.
- The method using solely the bottom point shows very consistent behaviour, already at a model using 3 layers.
- The method based on the entire transverse velocity profile shows as well consistent behaviour from 3 layers onward, except for some small variations between odd and even numbers in Figure D.2.
- The method using the bottommost part of the transverse velocity profile requires somewhat more layers before becoming consistent.

The calculation method based on the integral of the entire secondary flow velocity profile is preferred. This is due to the consistent behaviour for model results with a varying number vertical resolution and due to the fact that it is closest to the underlying idea of the derivations of De Vriend (1976). The calculation method using all points shows erroneous behaviour. This is caused by the velocity points in the area near z/h =0.5 where the transverse velocities are close to zero. Small absolute differences between the computed transverse profile and normalized profile can lead to very large relative differences, inducing large deviations. This is especially the case for low-resolution models with an odd number of layers, of which the transverse velocity component near z/h =0.5 is generally close to zero. For these cases, the relative magnitude of the central point can become either very large or small, inducing large deviations in the spiral flow intensity which is based on an average of all points describing the transverse velocity profile.

The method using solely the bottom point proved to be very consistent. This also applies to the method using the bottommost part of the surface, in case the bottommost part contains at least one entire velocity vector. In other words, the integral should at least be based on the bottommost 20% of the transverse velocity profile in case of a set-up using 5 layers, or 10% in case of 10 layers. The drawback of this calculation method is a decoupling from the theoretical foundation of the derivations of De Vriend (1976), which is based on the entire transverse velocity profile. This is especially the case when the transverse velocity profile differs strongly from the standard profile as derived by De Vriend (1976). However, when determining the bed shear stress direction, the outcomes are probably more realistic. This is due to the fact that mainly the bottommost part of the transverse flow velocity profile is of importance for calculating the transverse bed shear stress component.

Required vertical resolution

The first step is determining the minimum number of layers necessary for a consistent determination of the spiral flow intensity. This is shown in Figure D.4, in which the figures show the absolute value of the spiral flow intensity for the 15° and 145° cross-sections.

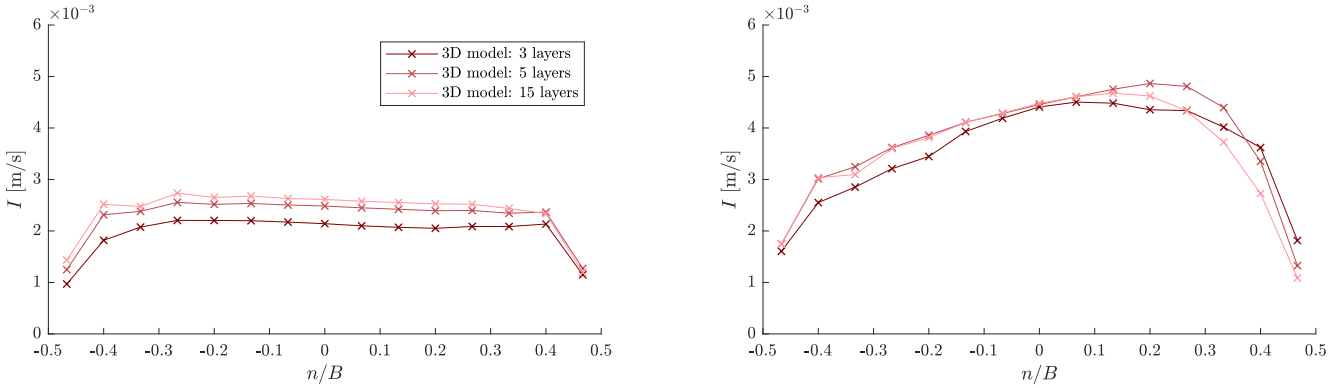

(a) 15° section (b) 145° section

Figure D.4: Case 1, spiral flow intensity, dependency on the vertical resolution (number of layers)

One can observe the large deviation for the set-up with 3 layers. The outcomes of the set-up with 5 layers agree relatively well with the reference set-up with 15 layers. The following differences can be observed:

- At the 15° cross-section, the spiral flow intensity is underestimated over the entire width by the set-up using 3 layers, and to a lesser extent by the set-up using 5 layers.
- At the 145° cross-section, the set-up using 3 layers differs from the 15 layer reference case over the entire width. The set-up using 5 layers agrees relatively well, except for a significant overestimation near the outer bend.

Figure D.5 indicates a significant difference in spiral flow intensity in the case of the set-up using 3 layers. The set-up using 5 layers slightly underestimates the spiral flow intensity at the stage of developing flow (0° to 60°), and overestimates the intensity at the stage of developed flow (from 60° onward).

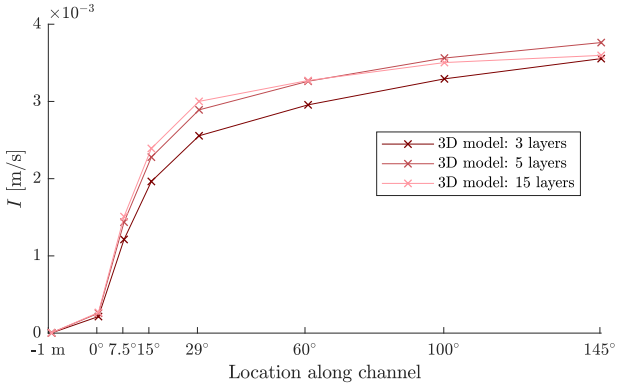

Figure D.5: Case 1, cross-section averaged spiral flow intensity, dependency on the vertical resolution (number of layers)

Loss of information

An important consequence of using the spiral flow intensity as input for the bed shear stress calculation, is the loss of information regarding the specific shape of the transverse velocity profile. As seen in Appendix E.1.3, the actual transverse velocity profile can differ from the analytically derived profile of De Vriend (1976). In case of the analytical profile of De Vriend (1976), the transverse velocities are of equal magnitude near the surface and bottom. The measurements and model results in Appendix E.1.3 show significantly larger flow velocities near the bed, which are likely to affect the transverse bed shear stress component. As a result, this component and thereby the angle deviation might be underestimated when using the new methodology. This could be prevented by using the calculation method which determines the spiral flow intensity solely on the bottommost part of the transverse velocity profile, as described above. Another solution might be using another normalized transverse velocity profile than obtained by De Vriend (1976). However, a perfectly fitting normalized profile does not exist, because the shape of the measured or modelled profile may vary per situation.

D.3. Bed shear stress

Magnitude

The first step taken in this section is the determination of the bed shear stress magnitude. Figure D.6 gives the development of the bed shear stress along the channel axis for the 3D model with a varying number of layers.

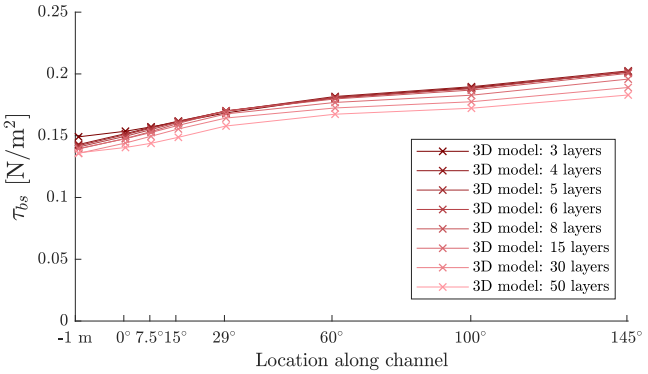

Figure D.6: Case 1, bed shear stress magnitude at the channel axis, dependency on the vertical resolution (number of layers)

A higher-resolution model is able to capture flow closer to the bed, however, the difference in bed shear stress magnitude is small. This is to be expected, as the distance at which the velocity is modelled is as well taken into account in determining the magnitude. The computed water level of all set-ups is the same. One can observe that the bed shear stress slightly decreases when defining a model set-up with more layers. In other words, low-vertical resolution models overestimate the velocities in the bottommost layer.

Direction

The next and last step is the determination of the bed shear stress direction. As a reference, Figure D.7 indi-

cates the flow direction of the bottommost layer in 3D models, for a varying number of layers. Normally the bed shear stress direction is set equal to this flow direction.

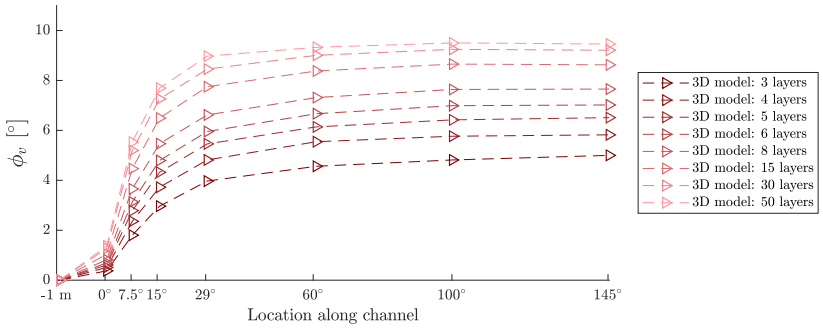

Figure D.7: Case 1, flow angle deviation in the bottommost layer at the channel axis, dependency on the vertical resolution (number of layers)

One can observe an increase of the angle with the number of layers. It is shown that the flow direction of the bottommost layer varies strongly with the applied resolution. The rate of change of the flow direction decreases when adding more layers. Nevertheless, a 15 layer model still underestimates the flow direction by about 1-1.5° compared with the 50 layer model. Figure D.7 indicates that at least 15 layers should be chosen when one desires to keep the error within 10% from a 50-layer reference set-up, when using the conventional 3D models using the conventional approach of equating the bed shear stress direction with the flow direction in the bottommost layer.

Figure D.8 depicts the angle deviation of the bed shear stress using the proposed method of this research, based on the spiral flow intensity.

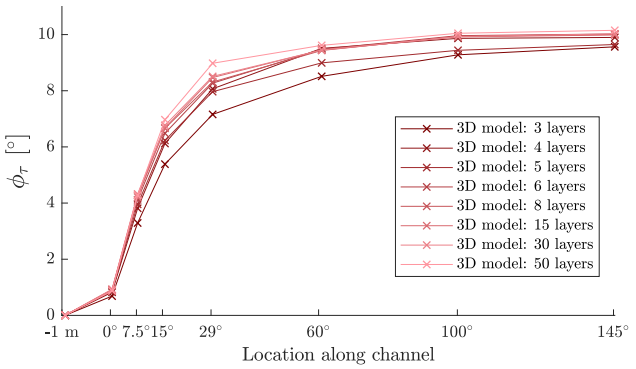

Figure D.8: Case 1, bed shear stress angle deviation at the channel axis, dependency on the vertical resolution (number of layers)

One can observe that the angle deviation barely varies for models with 5 layers or more. The largest differences for set-ups using 5 layers or more are found in the sections with developing flow (0° to 60°). At sections with developed flow (from 60° onward) only minor differences remain. Model set-ups using less than 5 layers generate significant deviations due to the following two reasons. At first, the hydrodynamics deviate from more detailed reference cases. The second cause is due to deviations in calculating the spiral flow intensity of models set-up using less than 5 layers. The set-up using 5 layers is considered to be sufficiently accurate because results based on this set-up are about equal to results of set-ups with a higher resolution.

E

Results

E.1. Case 1

E.1.1. Overview

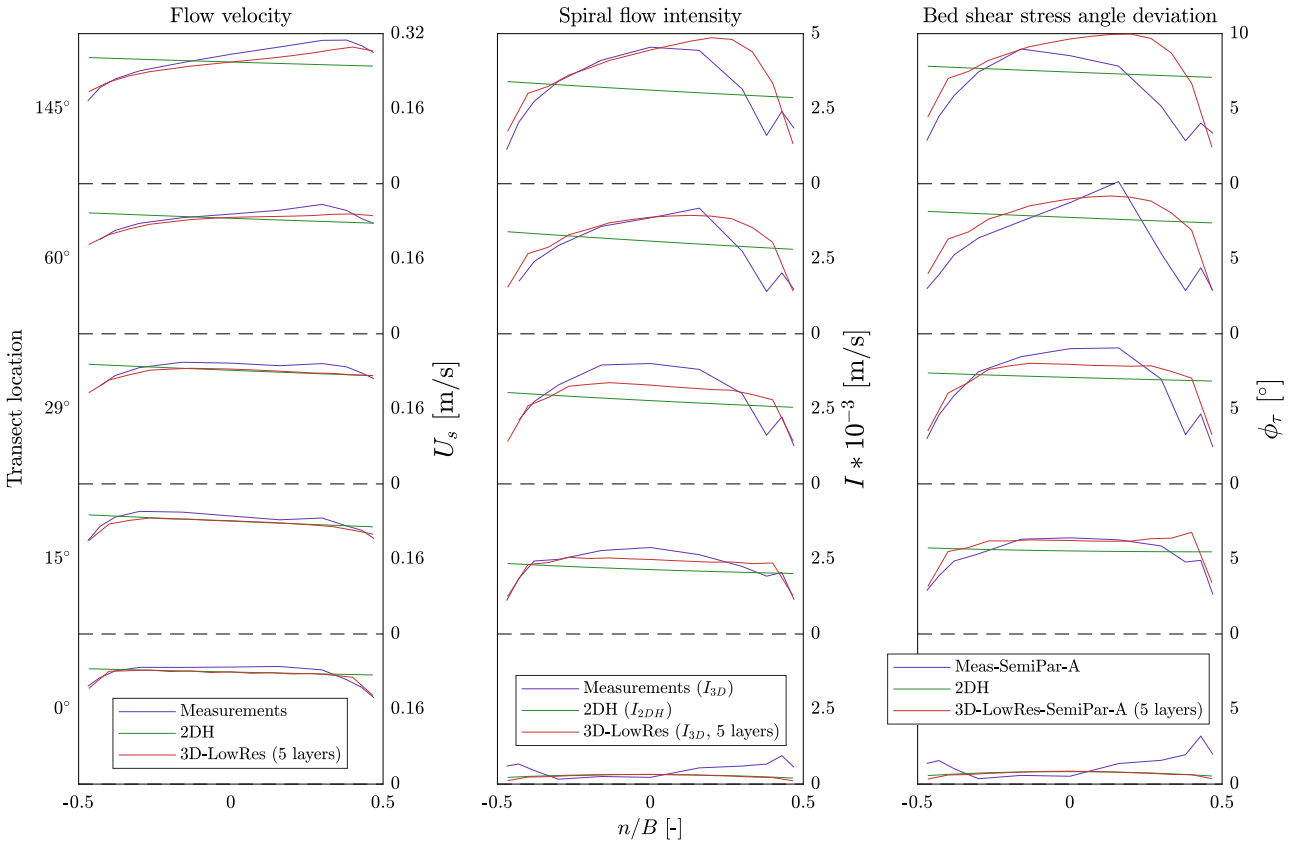

Figure E.1: Case 1, combined plot

E.1.2. Flow field

Figure E.2 depicts the flow velocities and water levels (both cross-section averaged) of the 2D and 3D model results and measurements. The most particular differences which can be observed in Figure E.2 are as follows:

- The maximum deviation of the water levels and velocities of the 2D and 3D model results from the measurements is about 4%.
- The 2D model results show larger flow velocities and lower water levels than the 3D model results.

- Both the 2D and 3D model results show a smooth development of the velocity and water level, where the measurements show a more varying development. The most particular feature of measurement data is the flow acceleration from -1 m to at 15°.

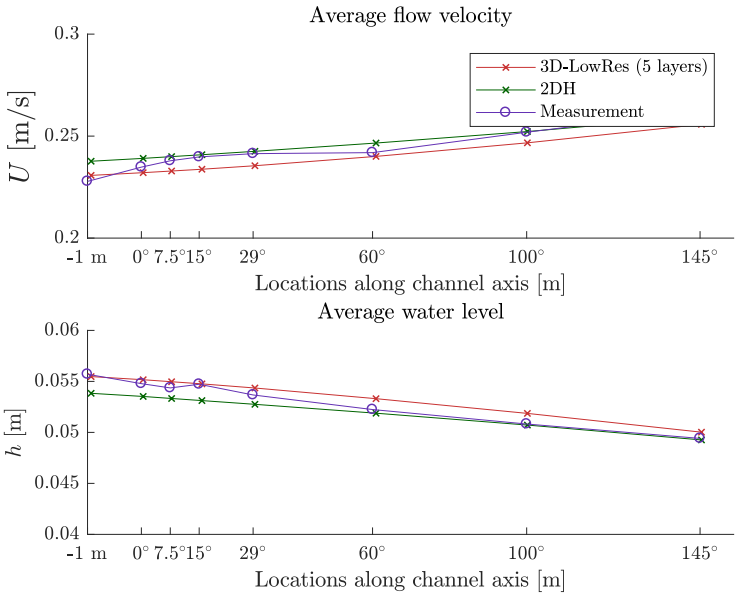

Figure E.2: Case 1, water level and velocity development

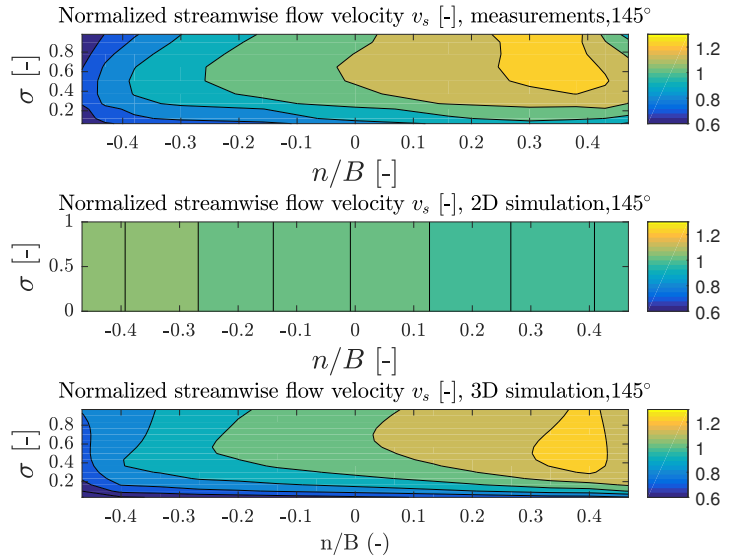

Figure E.3: Case 1, normalized streamwise flow velocities

E.1.3. Streamwise and transverse velocity profiles

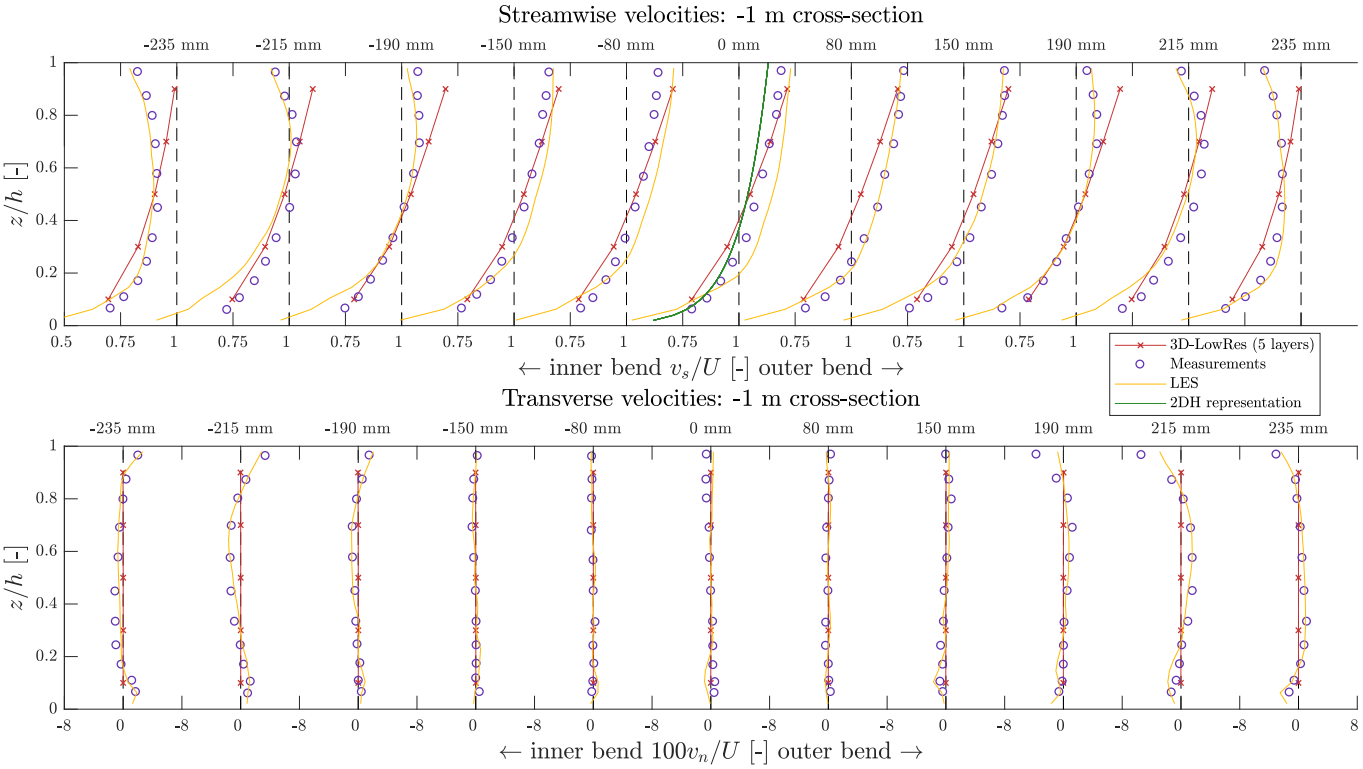

Figure E.4: Case 1, flow velocities at 1 m before bend

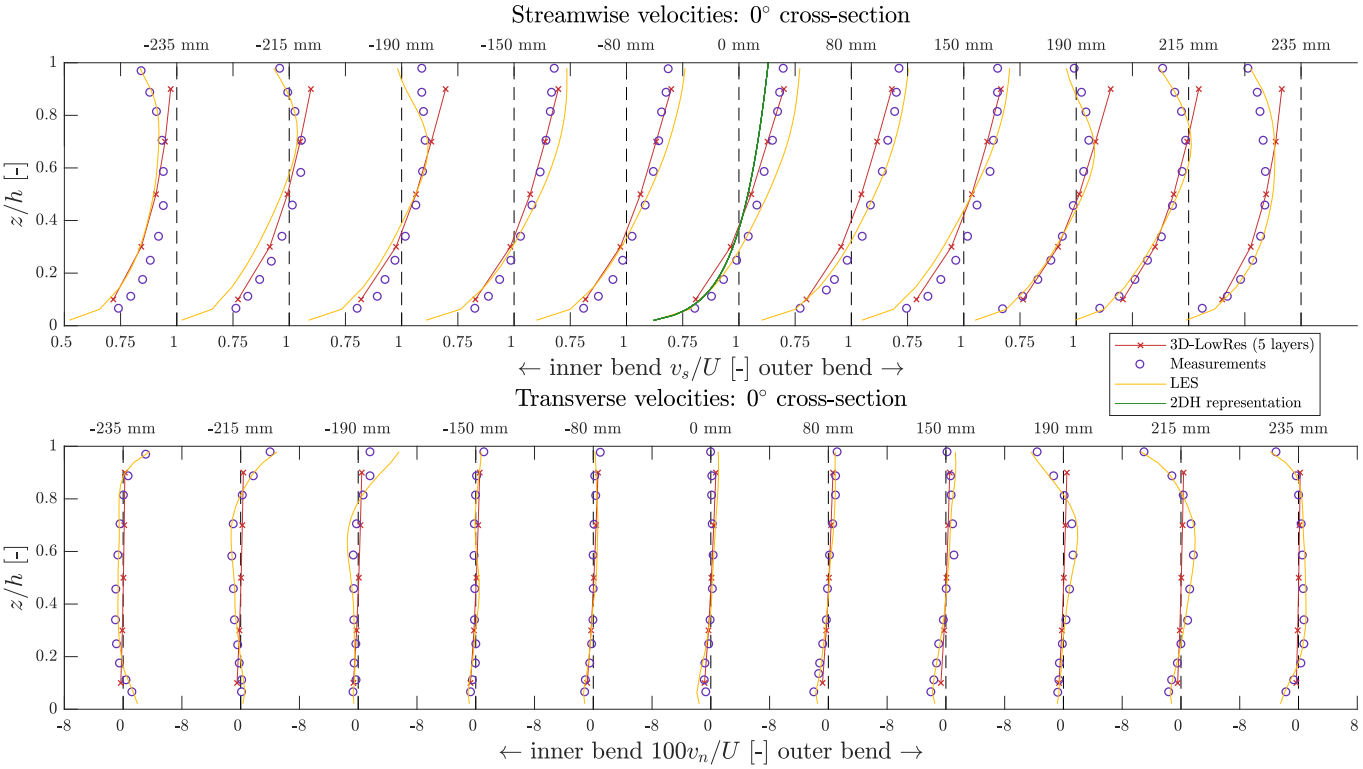

Figure E.5: Case 1, flow velocities at bend entrance

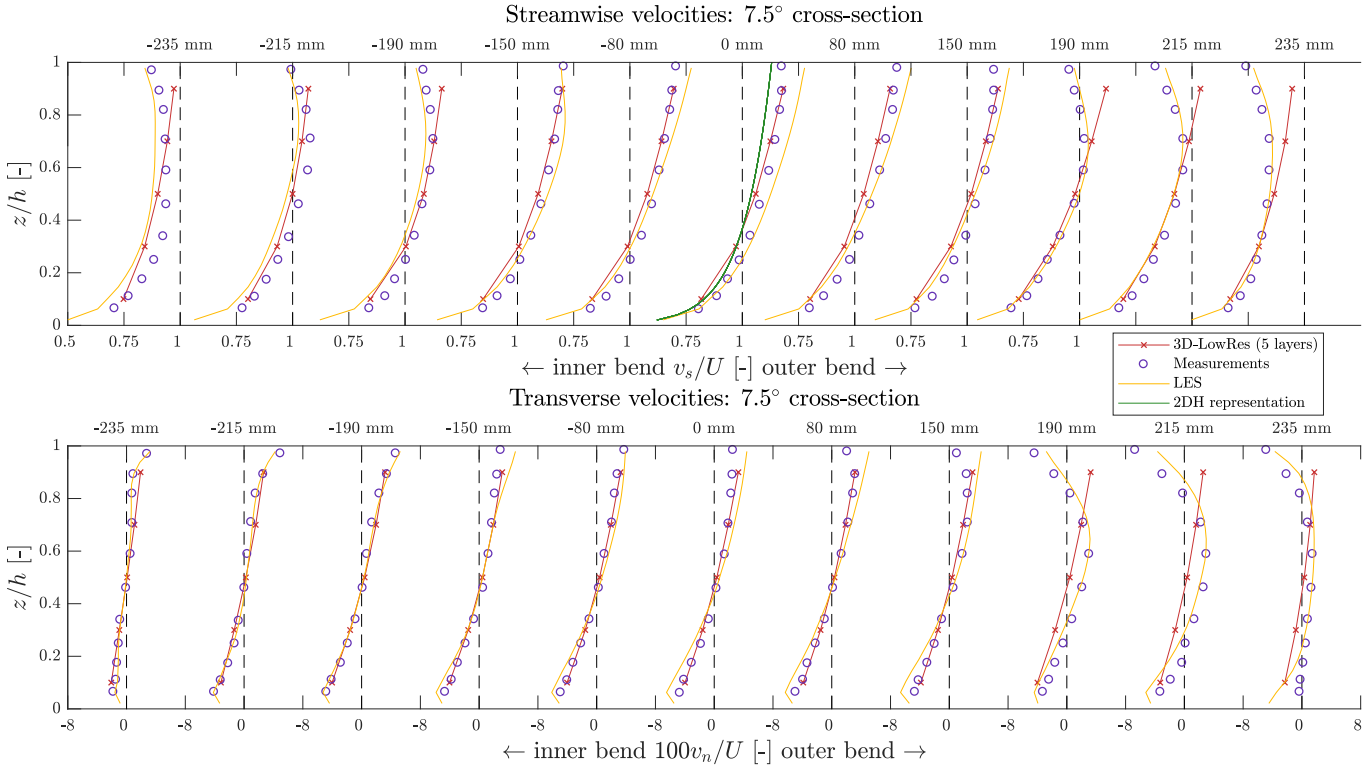

Figure E.6: Case 1, flow velocities at 7.5° cross-section

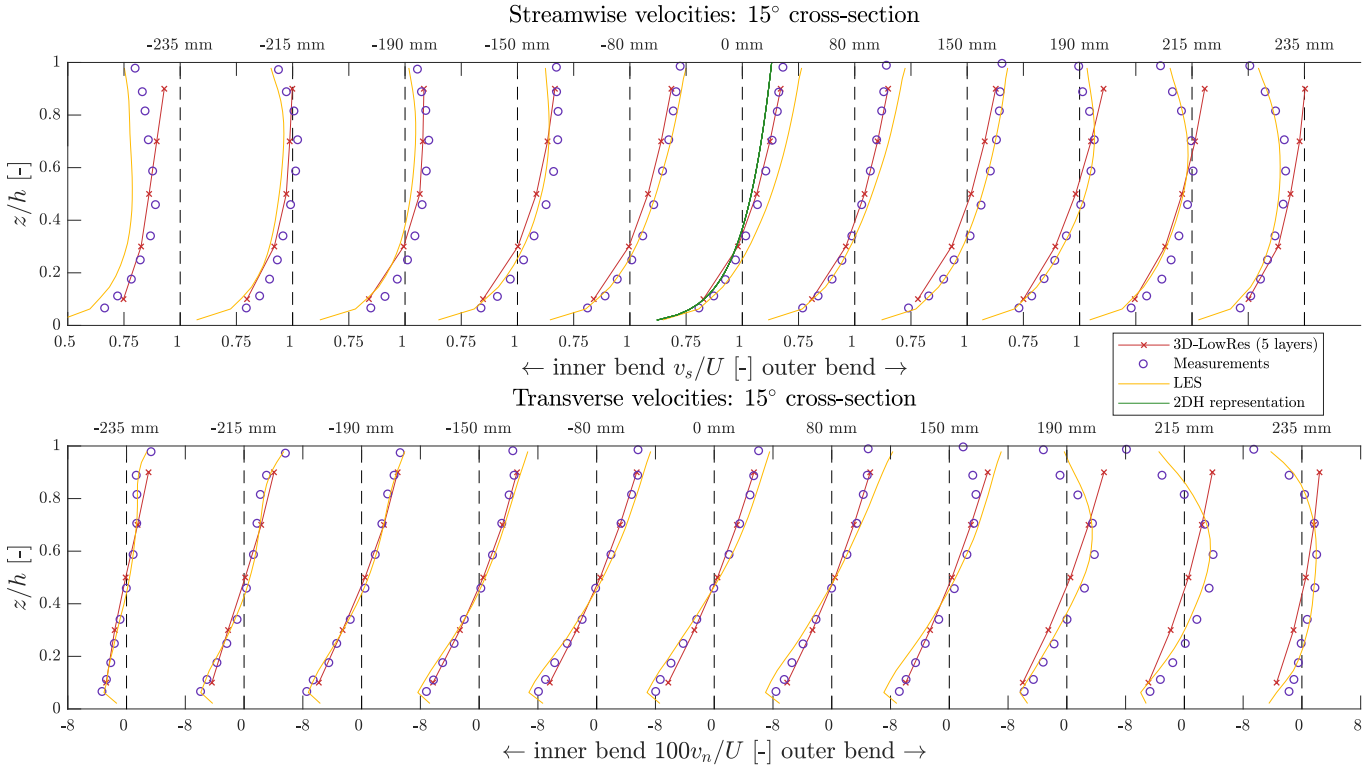

Figure E.7: Case 1, flow velocities at 15° cross-section

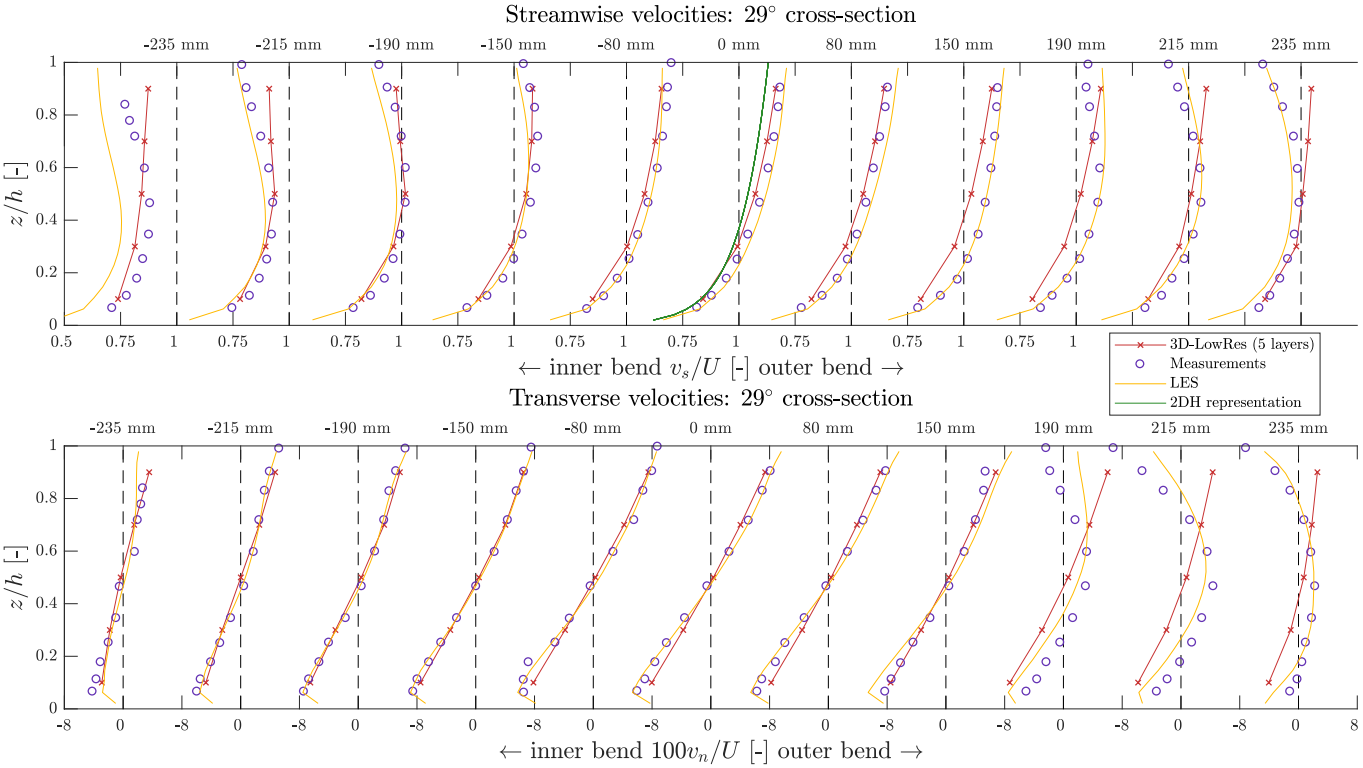

Figure E.8: Case 1, flow velocities at 29° cross-section

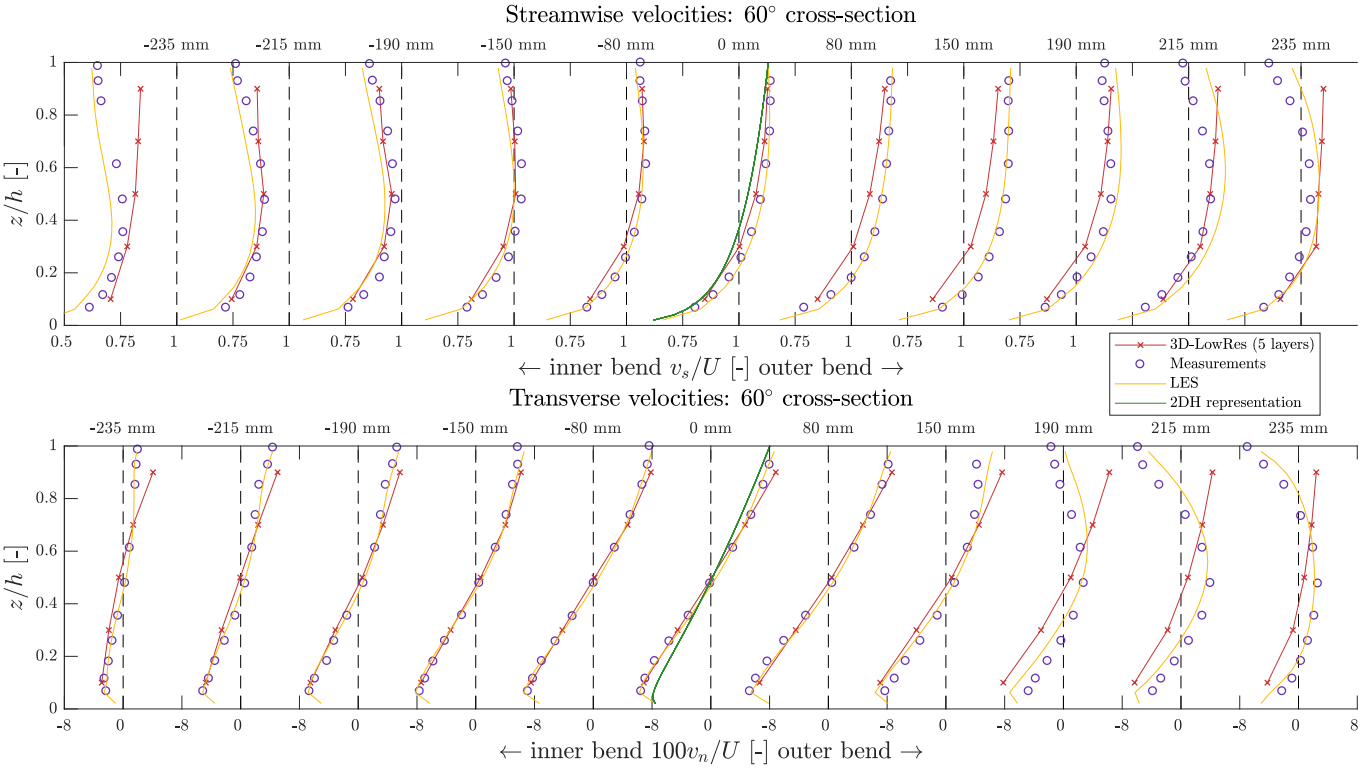

Figure E.9: Case 1, flow velocities at 60° cross-section

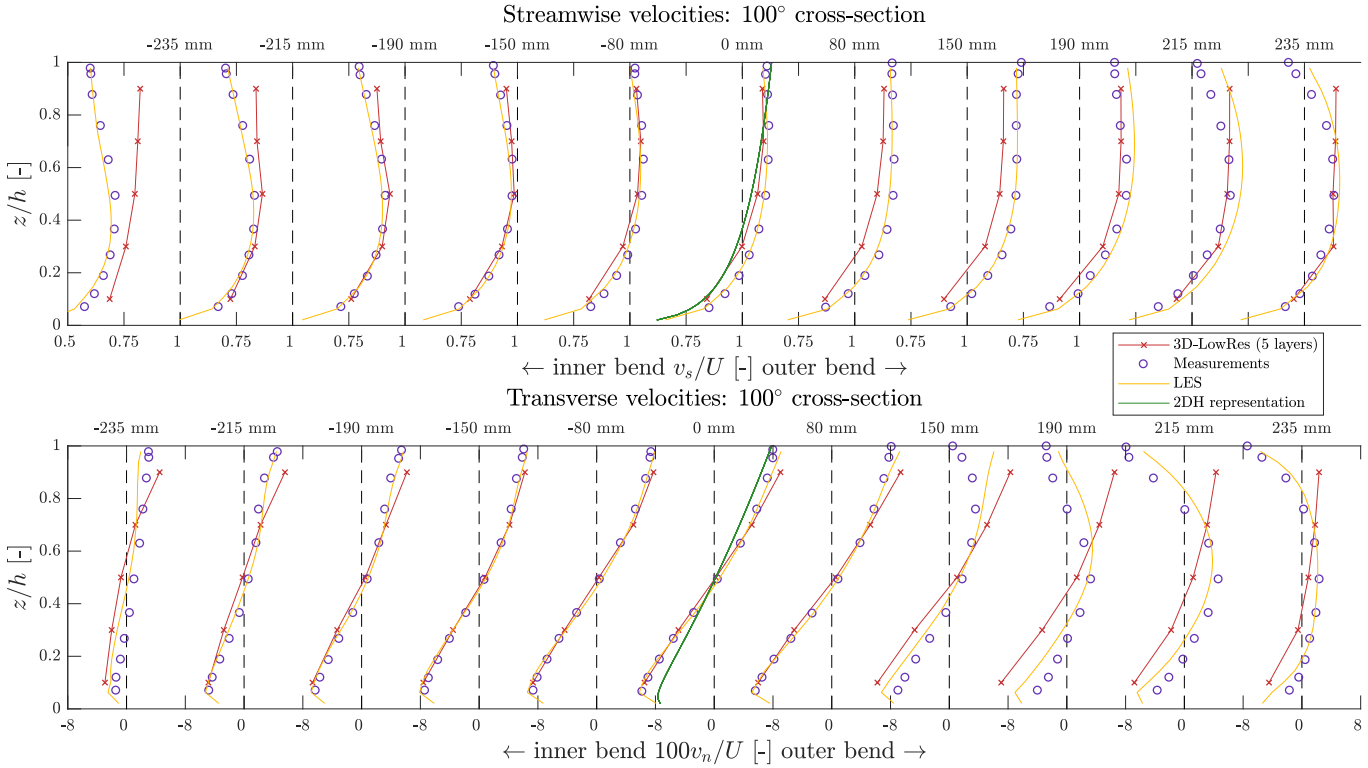

Figure E.10: Case 1, flow velocities at 100° cross-section

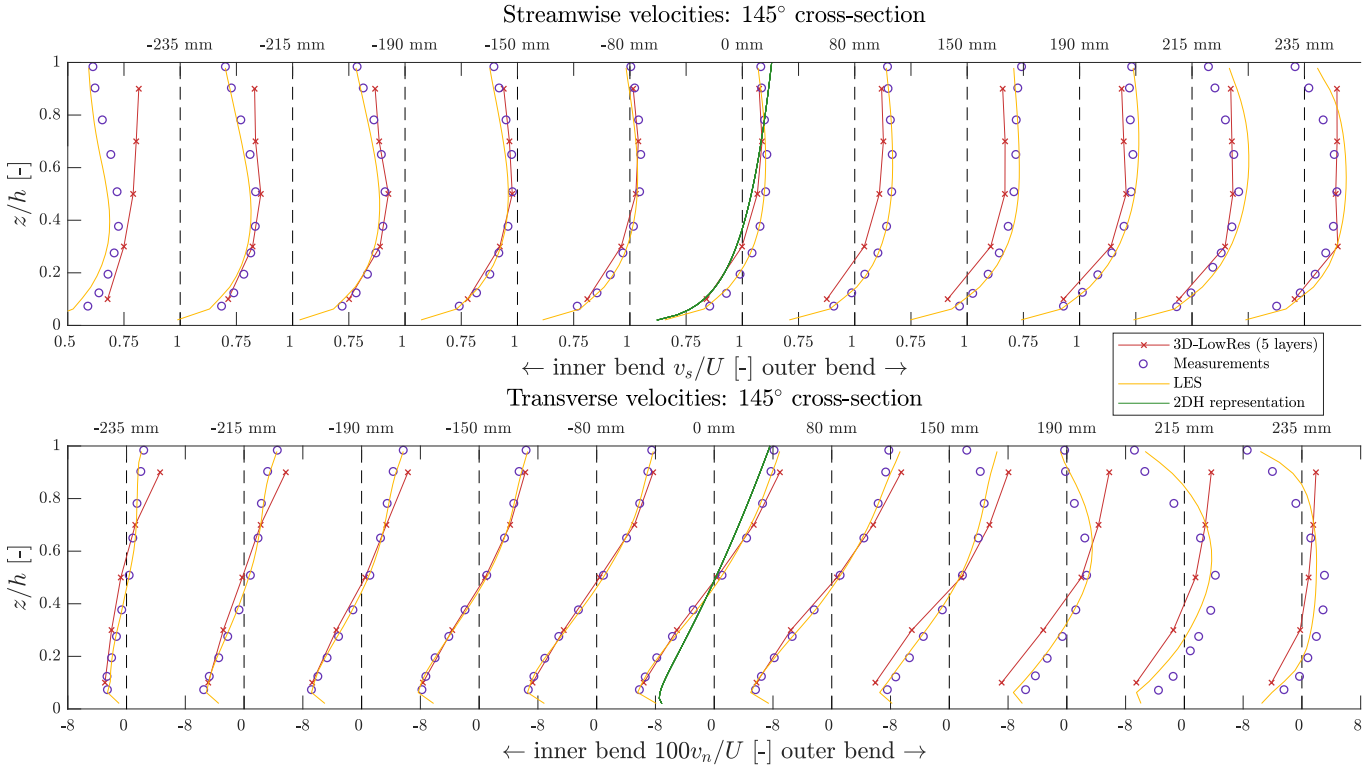

Figure E.11: Case 1, flow velocities at 145° cross-section

E.1.4. Effect of varying vertical resolutions on the velocity profiles

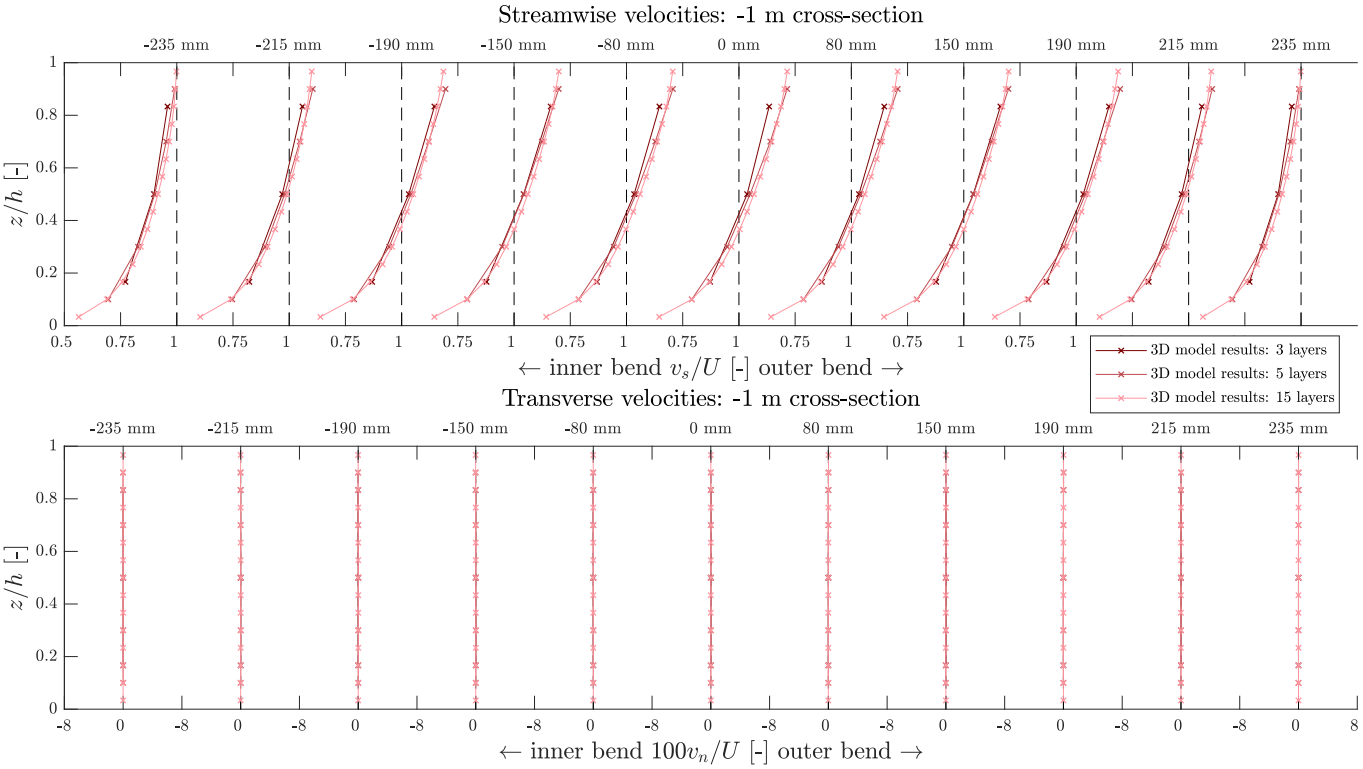

Figure E.12: Case 1, flow velocities at 1 m before bend

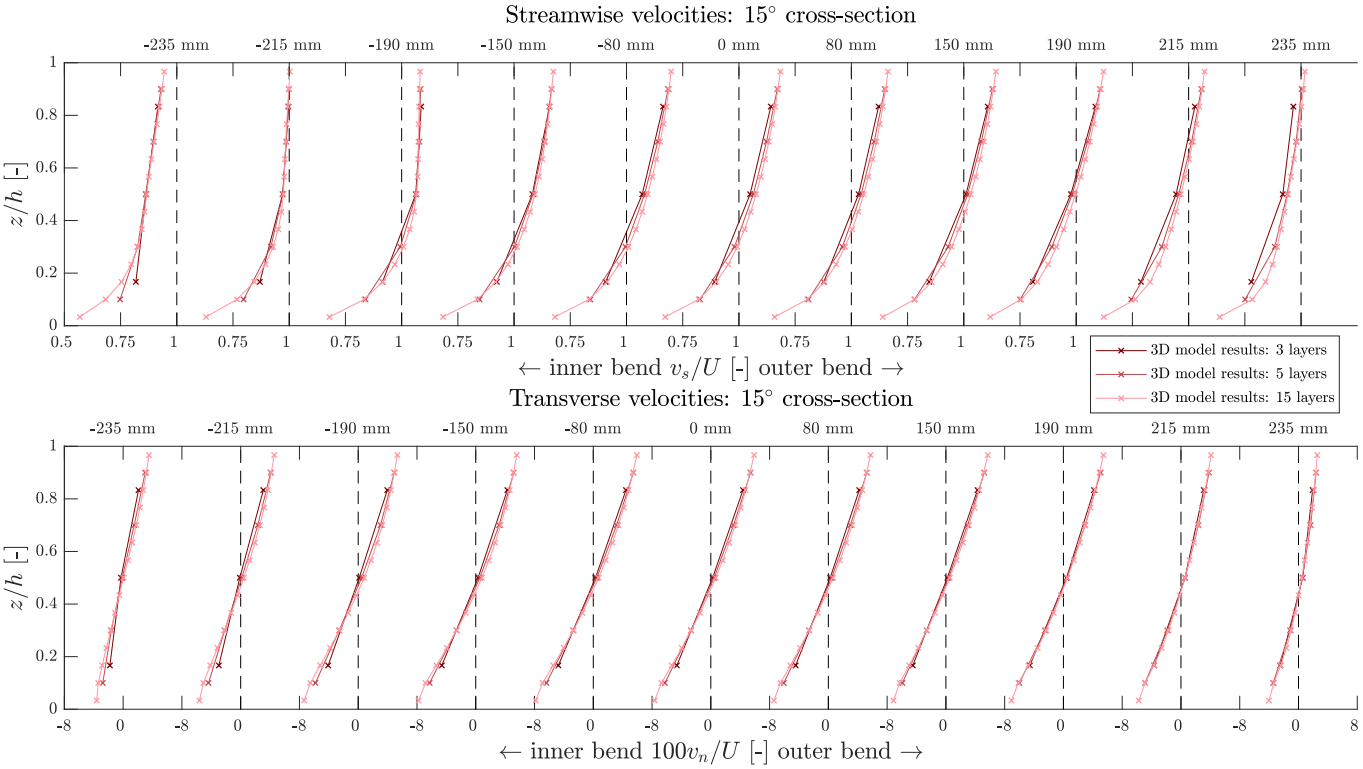

Figure E.13: Case 1, flow velocities at the 15° cross-section

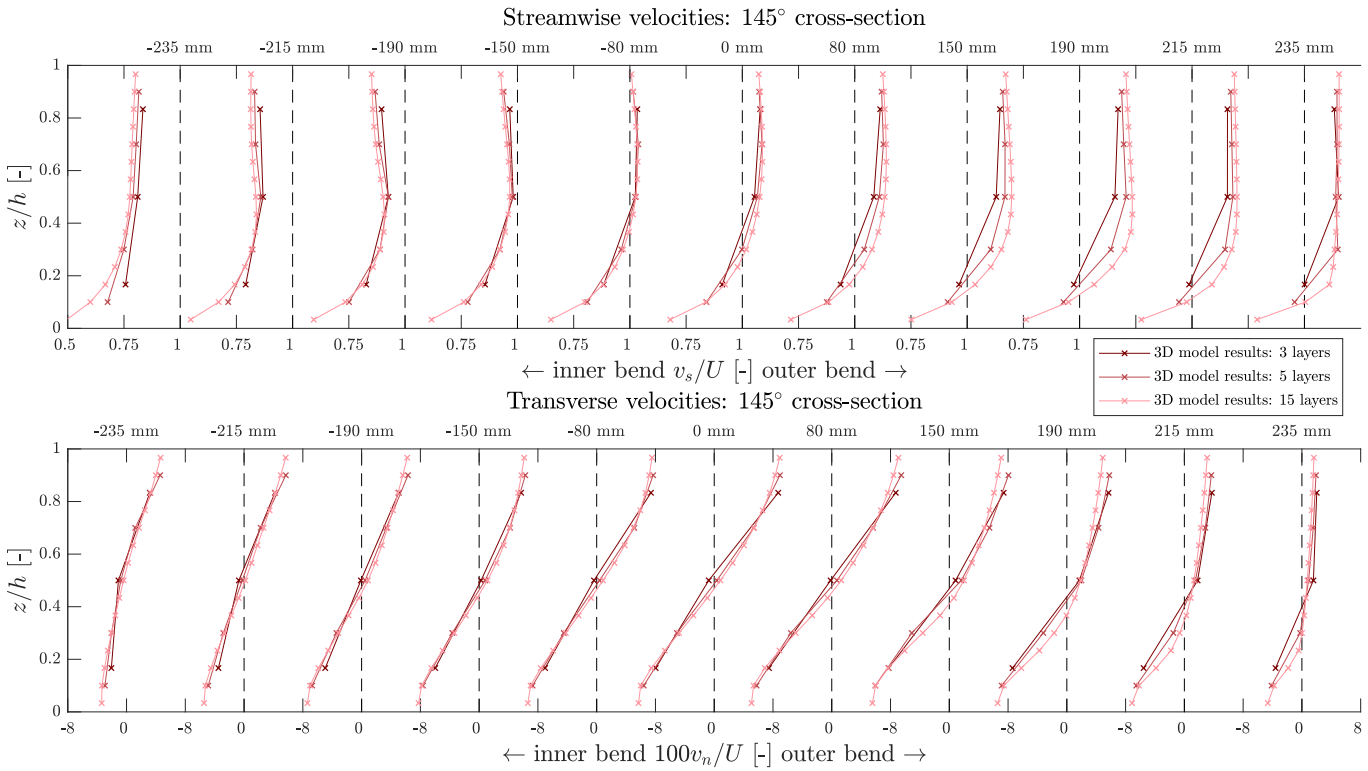

Figure E.14: Case 1, flow velocities at the 145° cross-section

E.2. Case 2

E.2.1. Overview

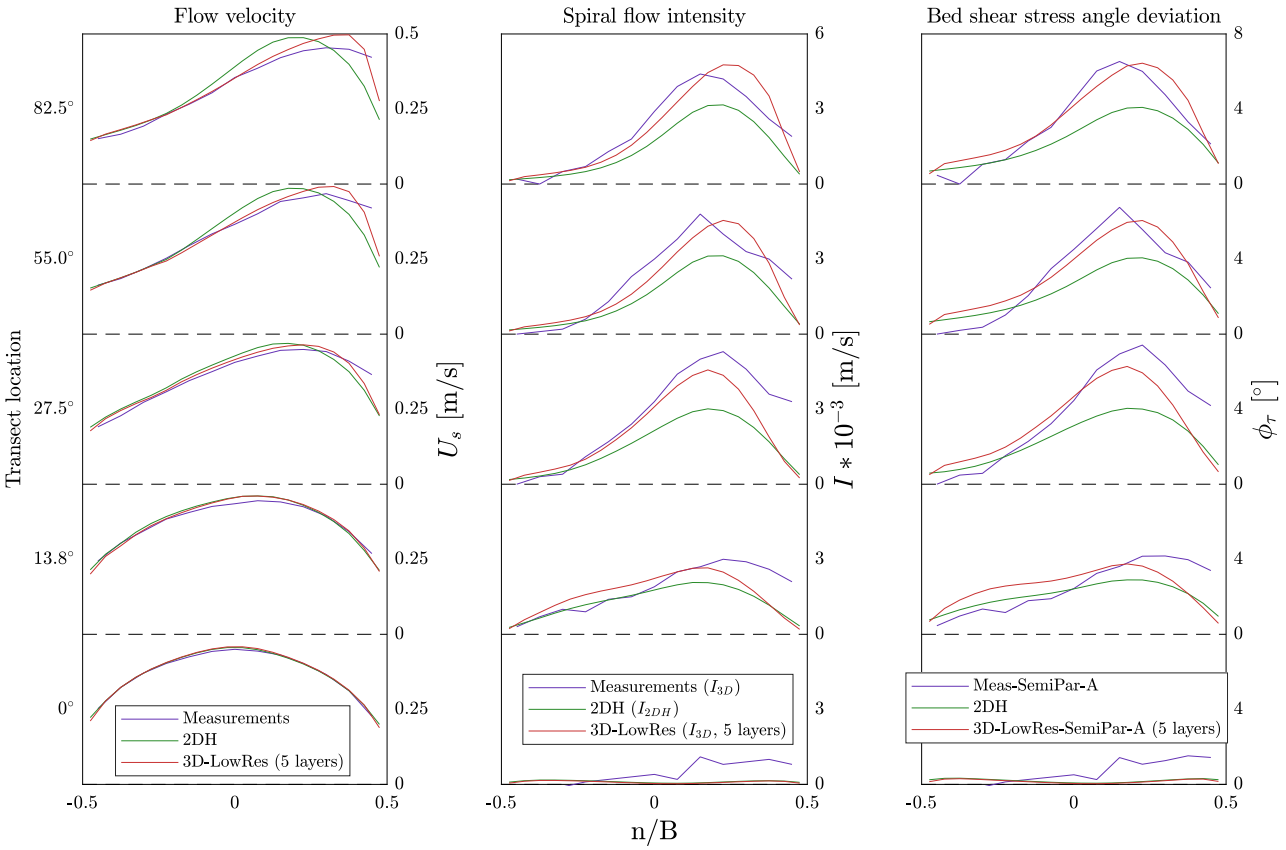

Figure E.15: Case 2, combined plot

E.2.2. Flow field

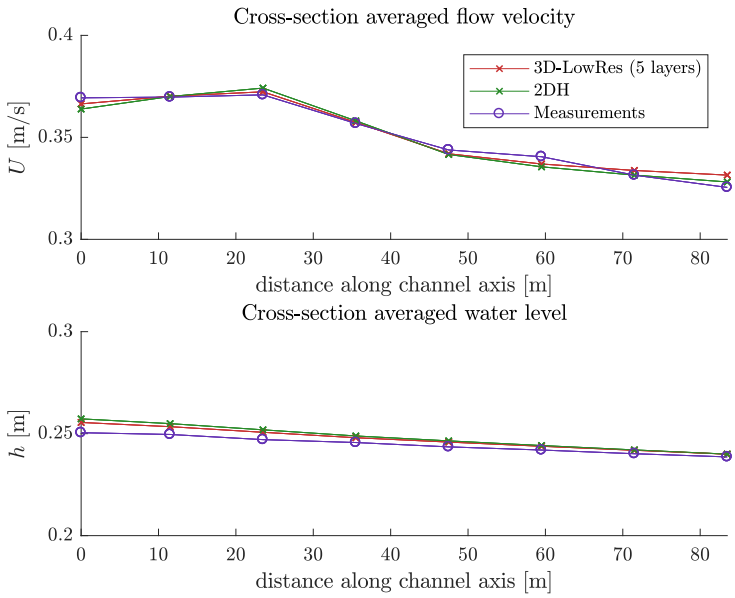

Figure E.16: Case 2, water level and velocity development

E.2.3. Bed shear stress

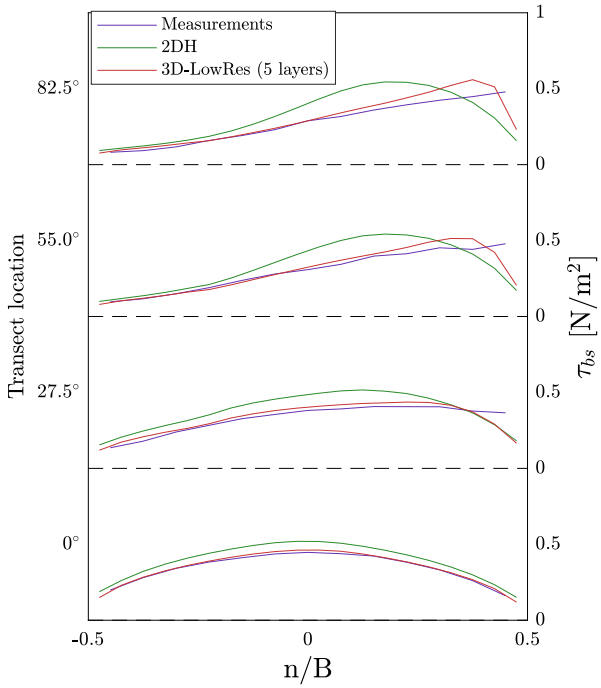

Figure E.17: Case 2, distribution of the bed shear stress magnitude at several cross-sections

E.2.4. Streamwise and transverse velocity profiles

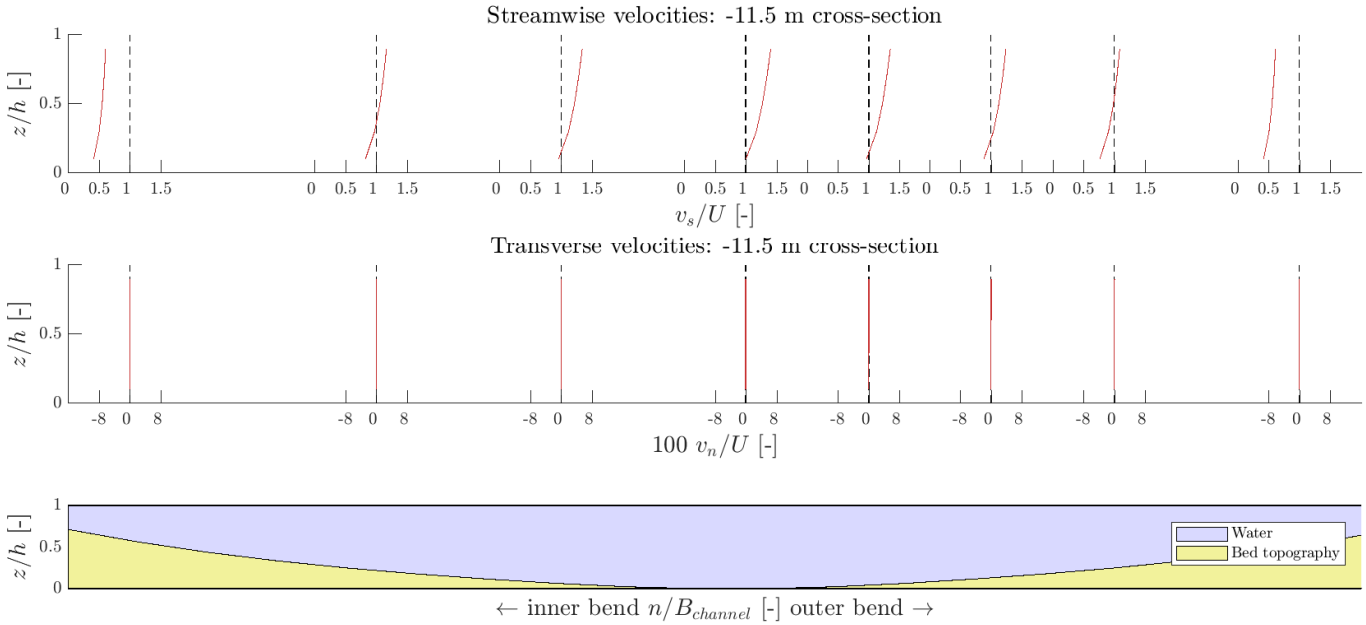

Figure E.18: Case 2, flow velocities at straight channel section

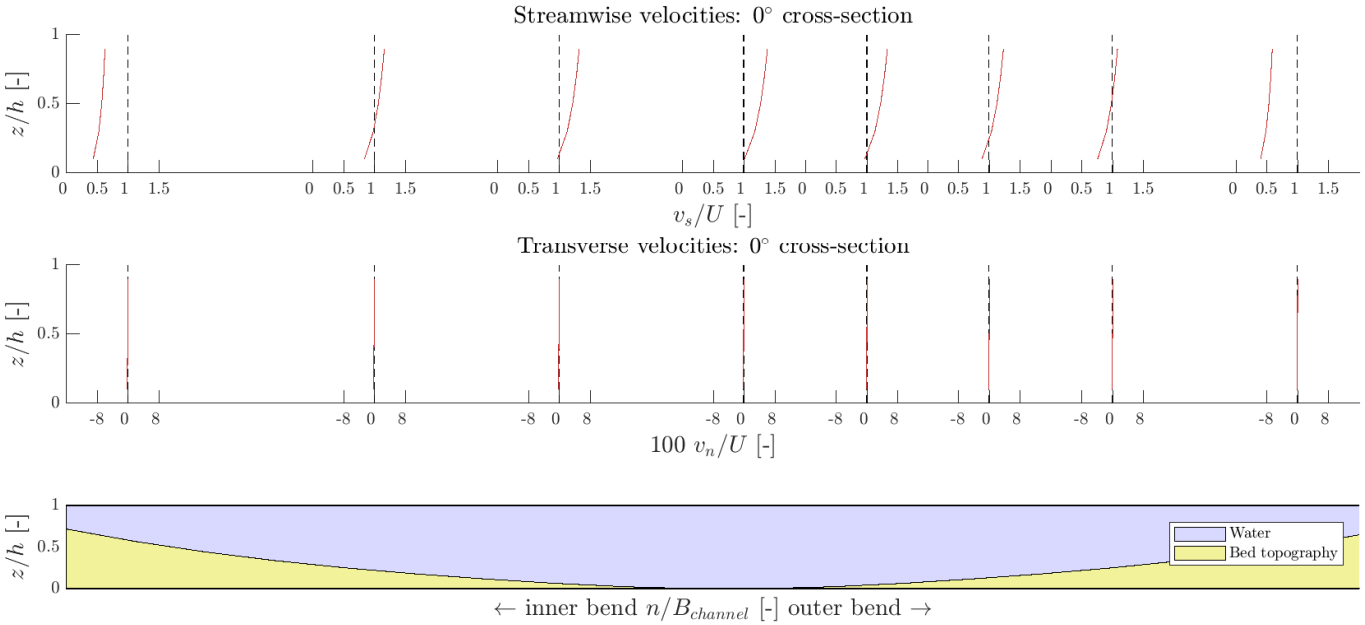

Figure E.19: Case 2, flow velocities at 0° cross-section

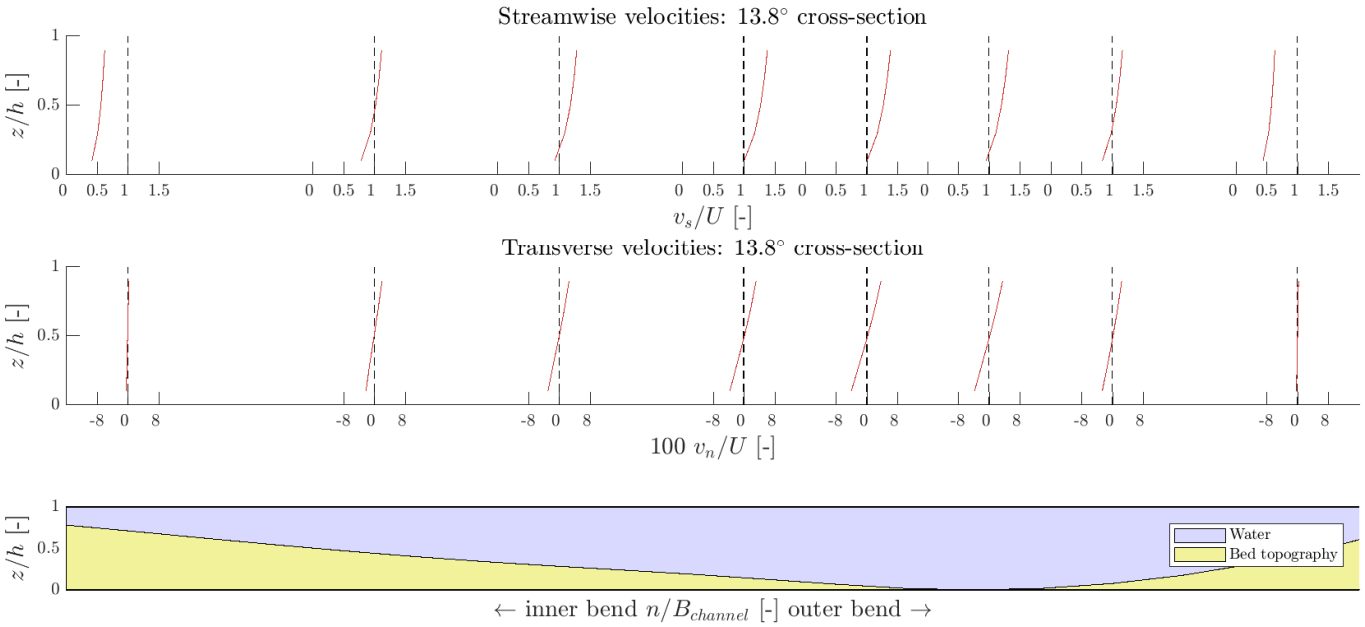

Figure E.20: Case 2, flow velocities at 13.8° cross-section

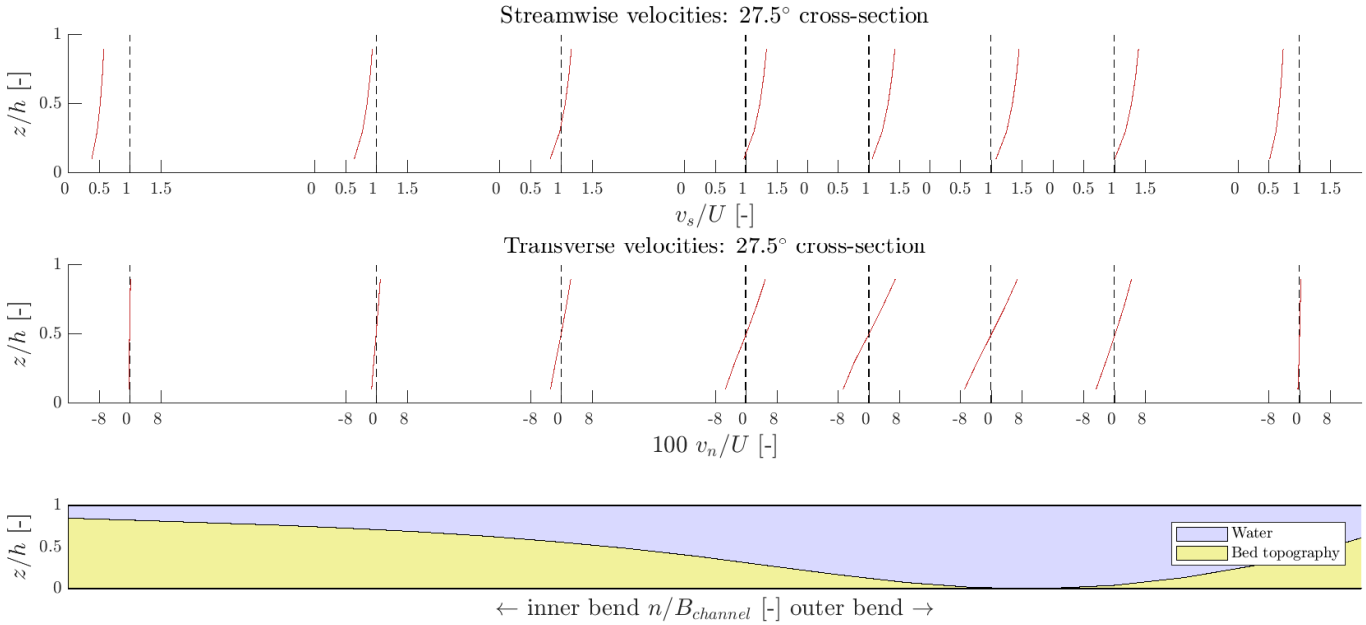

Figure E.21: Case 2, flow velocities at 27.5° cross-section

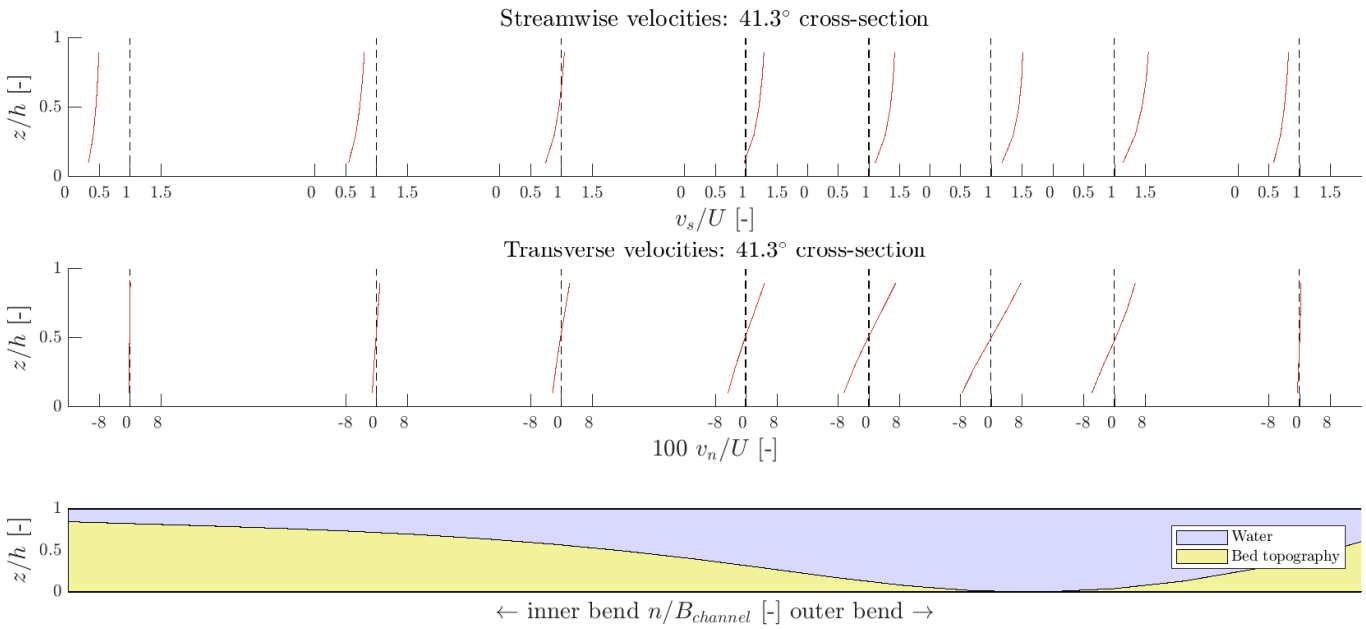

Figure E.22: Case 2, flow velocities at 41.3° cross-section

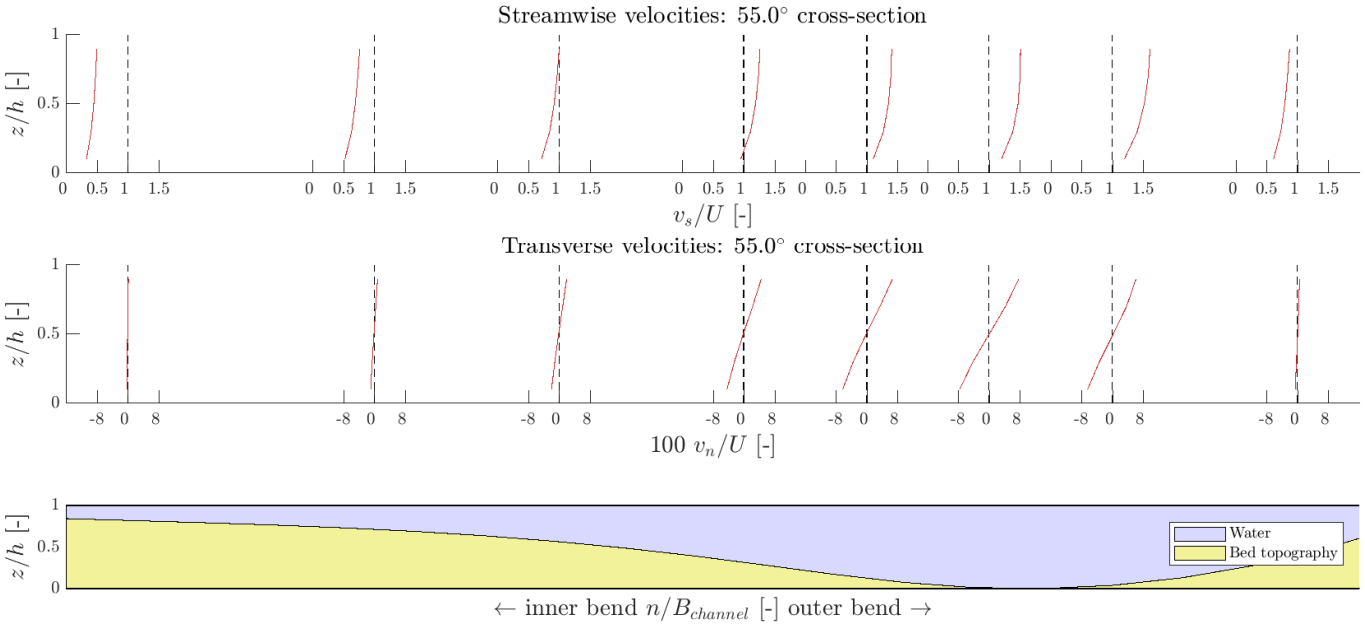

Figure E.23: Case 2, flow velocities at 55° cross-section

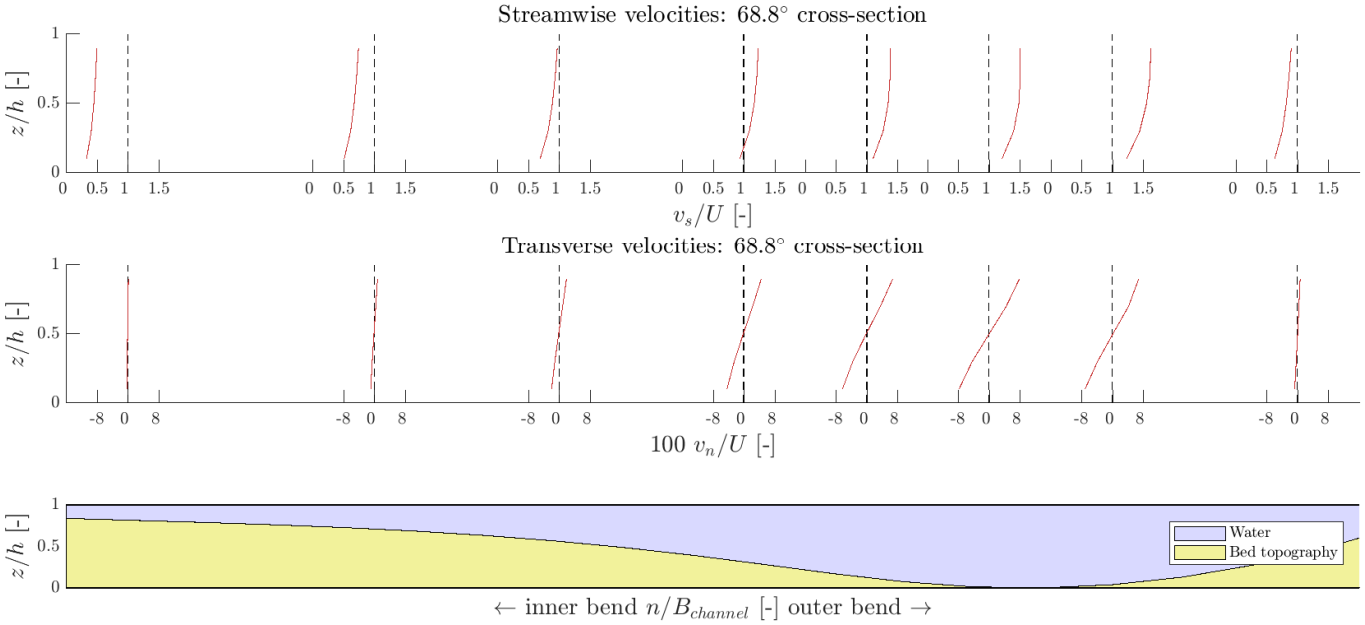

Figure E.24: Case 2, flow velocities at 68.8° cross-section

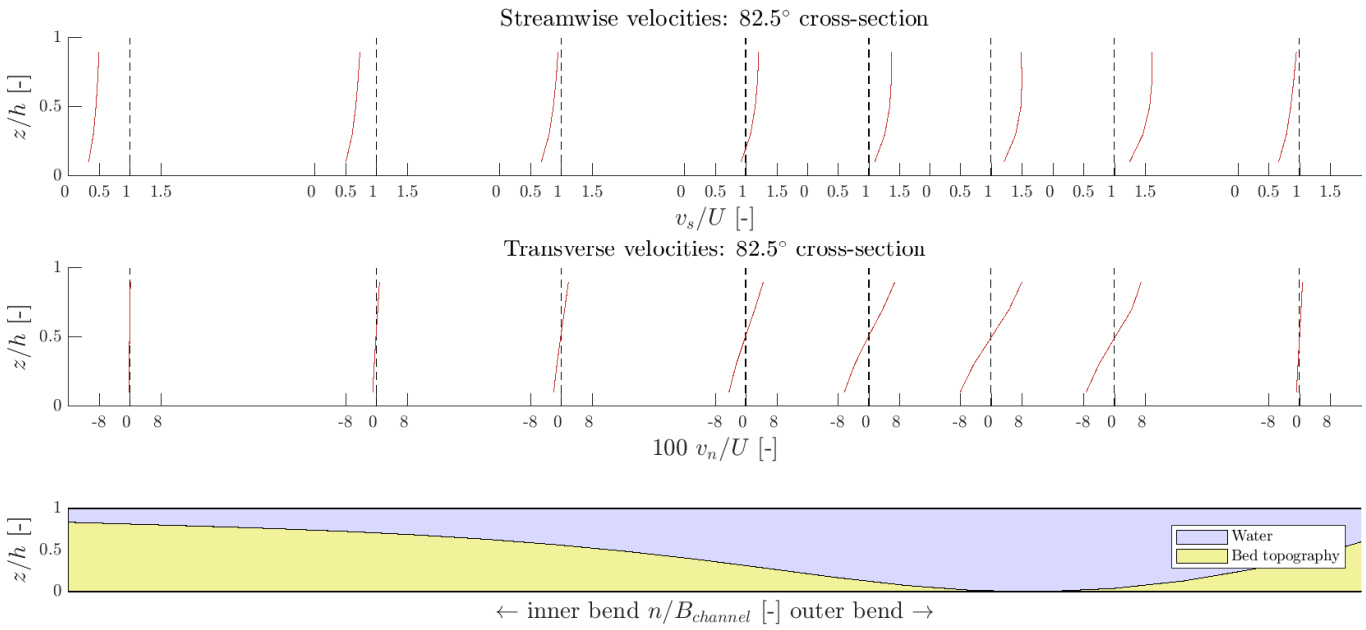

Figure E.25: Case 2, flow velocities at 82.5° cross-section

E.3. Case 3

E.3.1. Overview

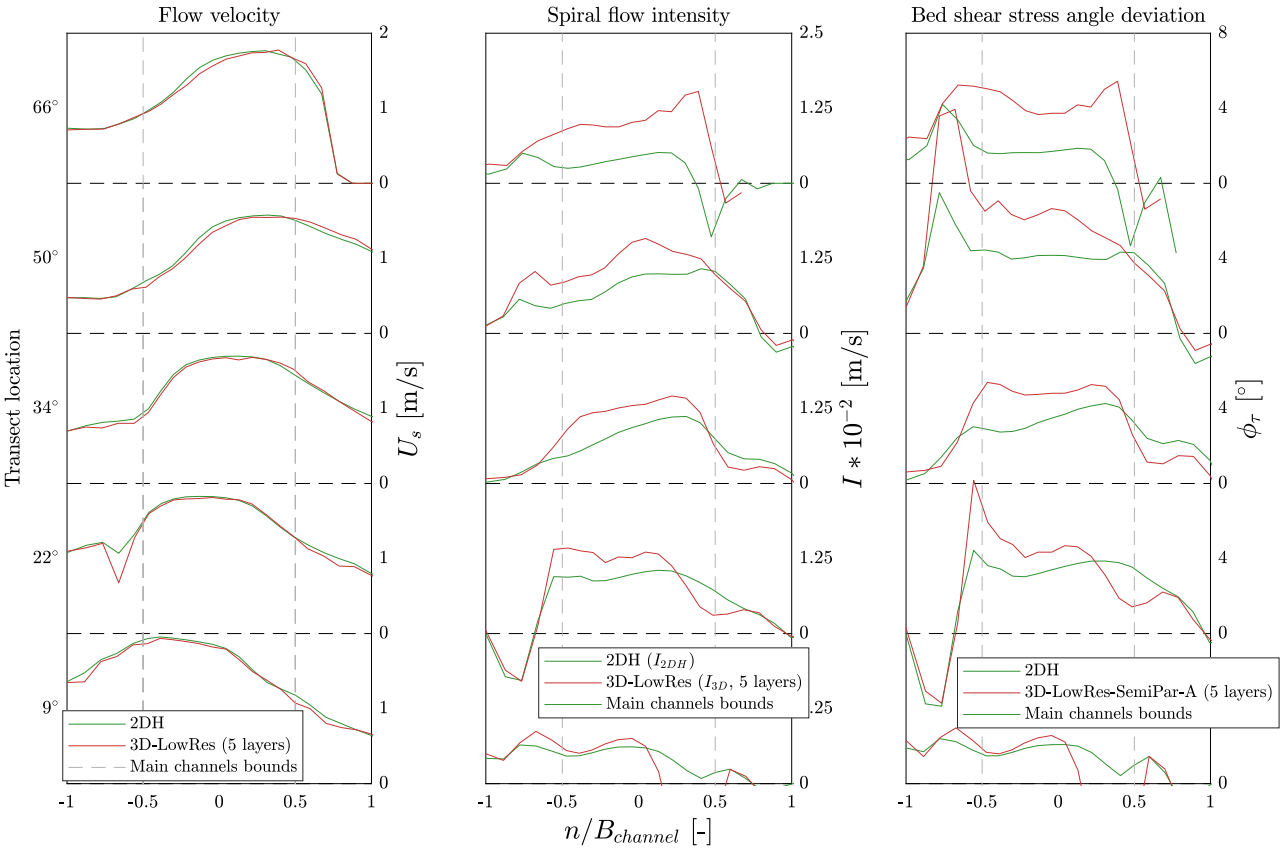

Figure E.26: Case 3, combined plot

E.3.2. Flow field

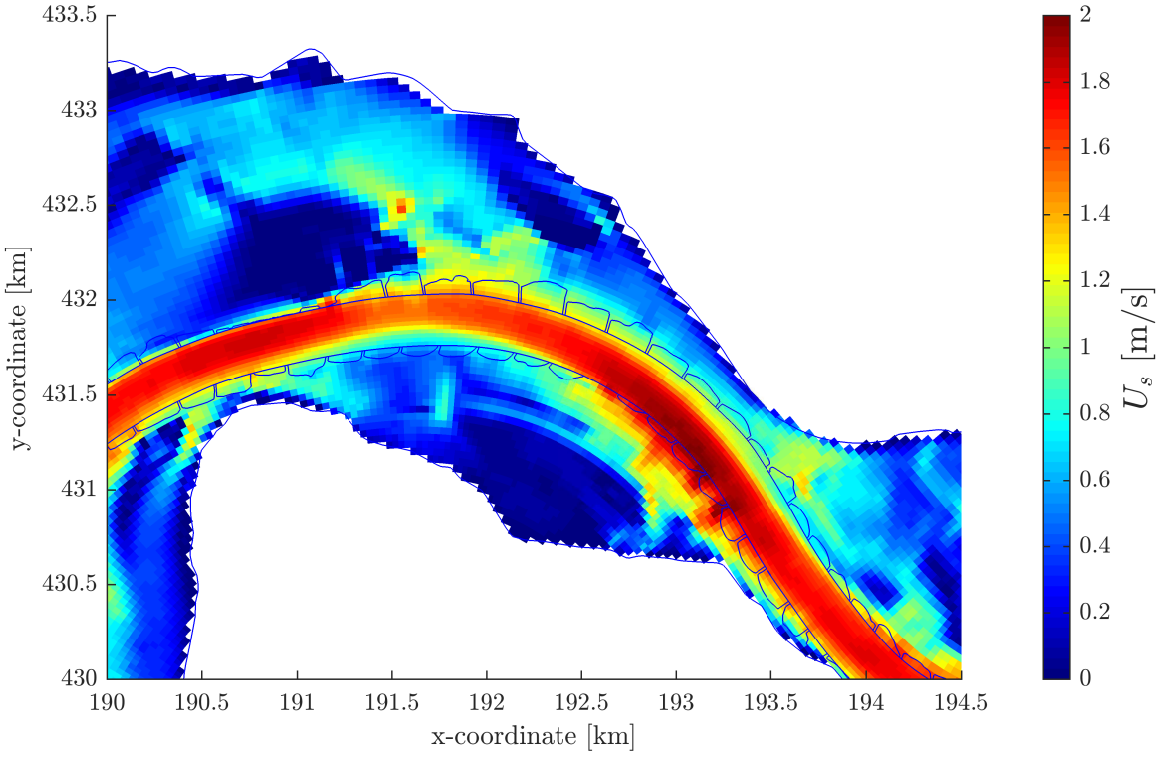

Figure E.27: Case 3, depth-averaged flow velocities of the 2DH model (enlarged)

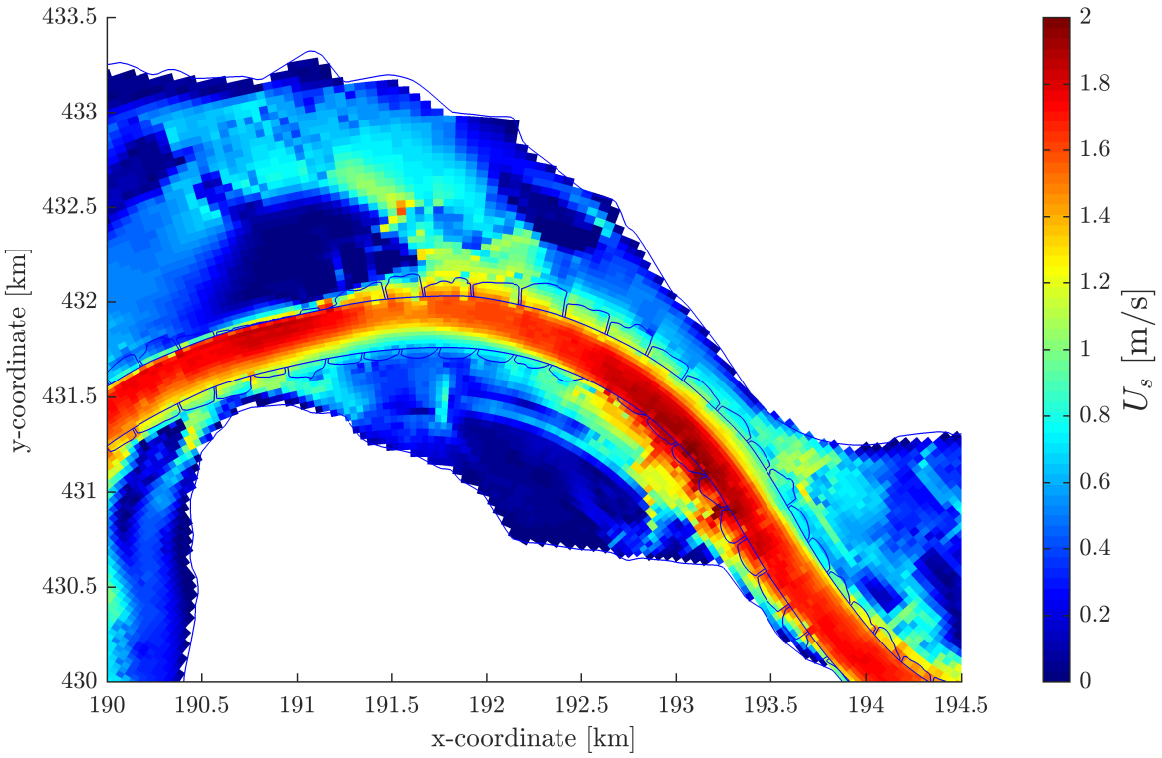

Figure E.28: Case 3, depth-averaged flow velocities of the 3D model (enlarged)

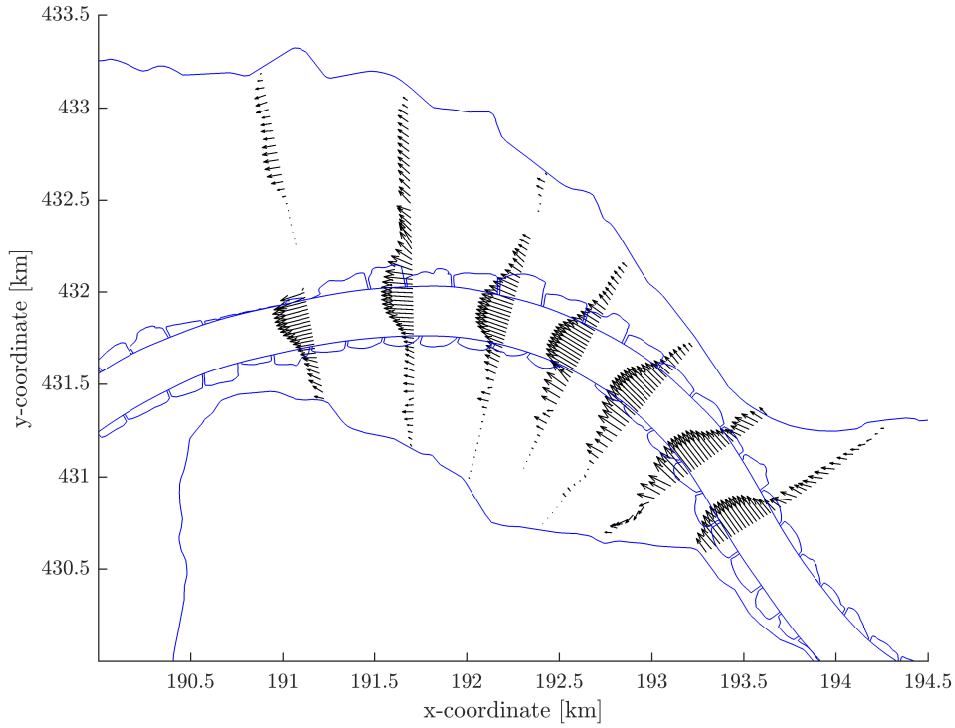

Figure E.29: Case 3, flow vectors of the 3D model

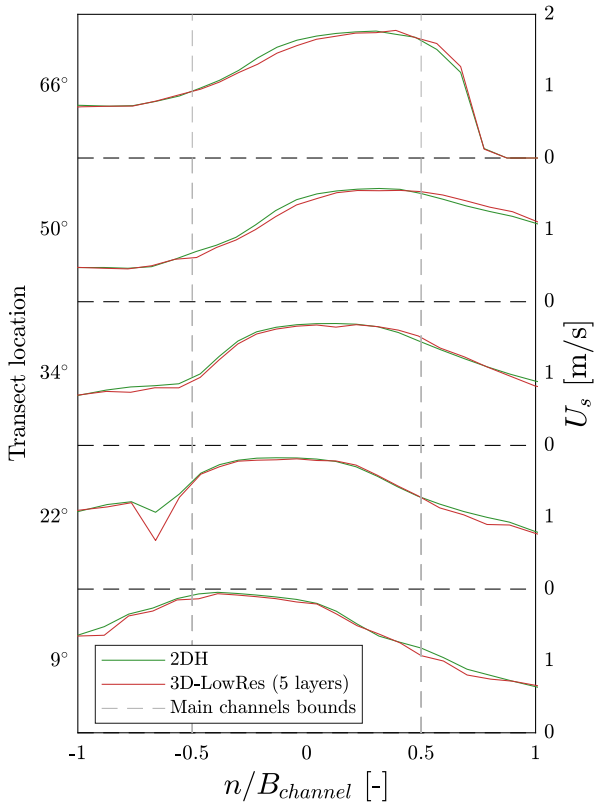

Figure E.30: Case 3, depth-averaged flow velocities

E.3.3. Bed shear stress

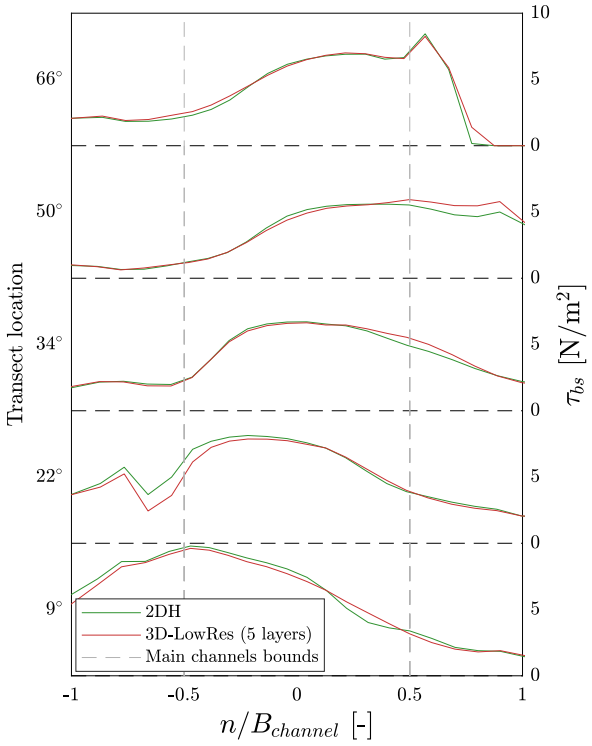

Figure E.31: Case 3, distribution of the bed shear stress magnitude at several cross-sections

E.3.4. Streamwise and transverse velocity profiles

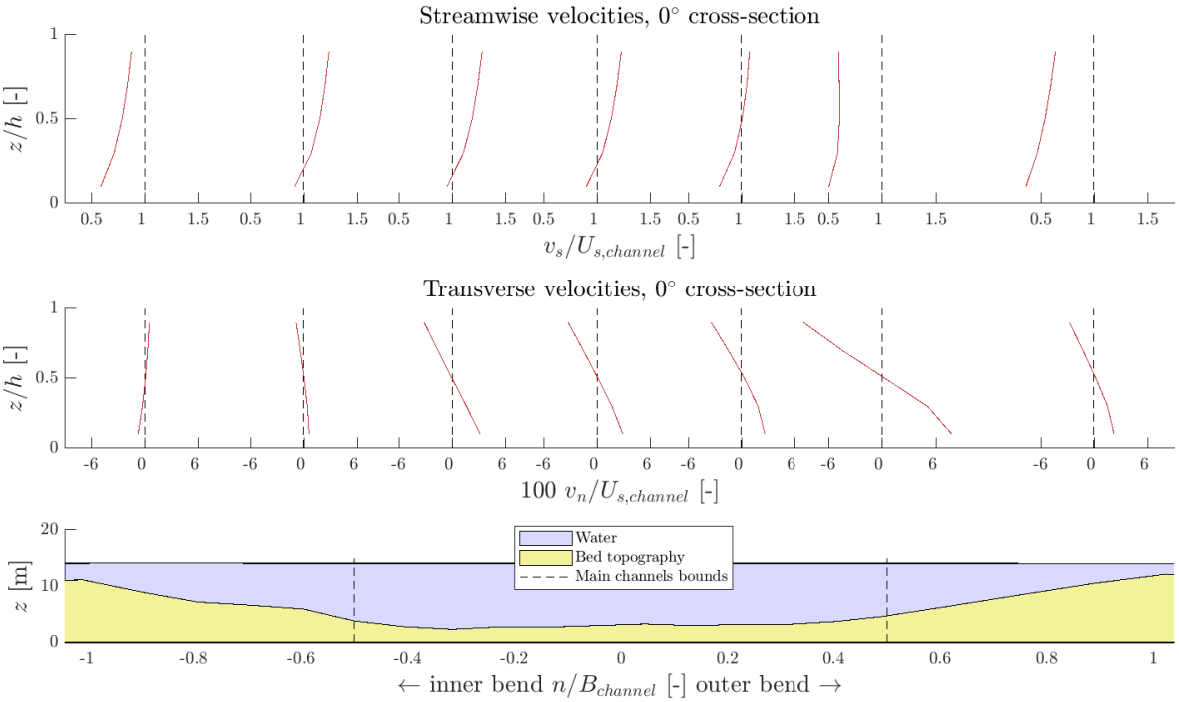

Figure E.32: Case 3, flow velocities at 0° cross-section

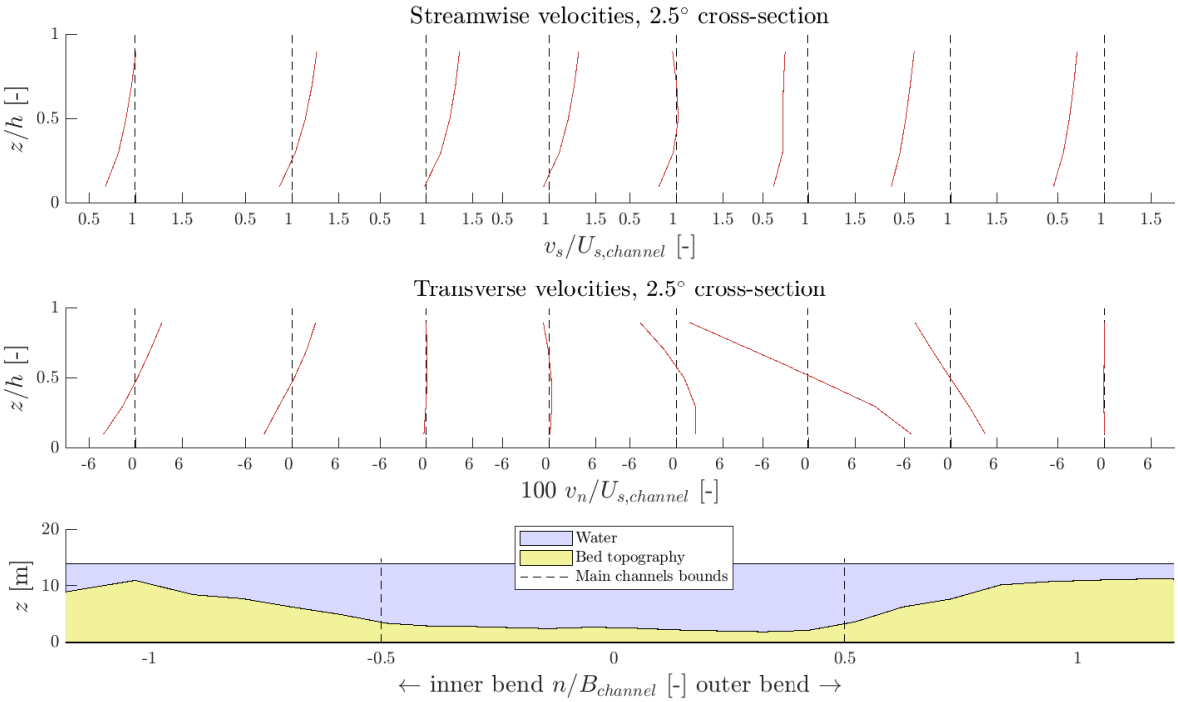

Figure E.33: Case 3, flow velocities at 2.5° cross-section

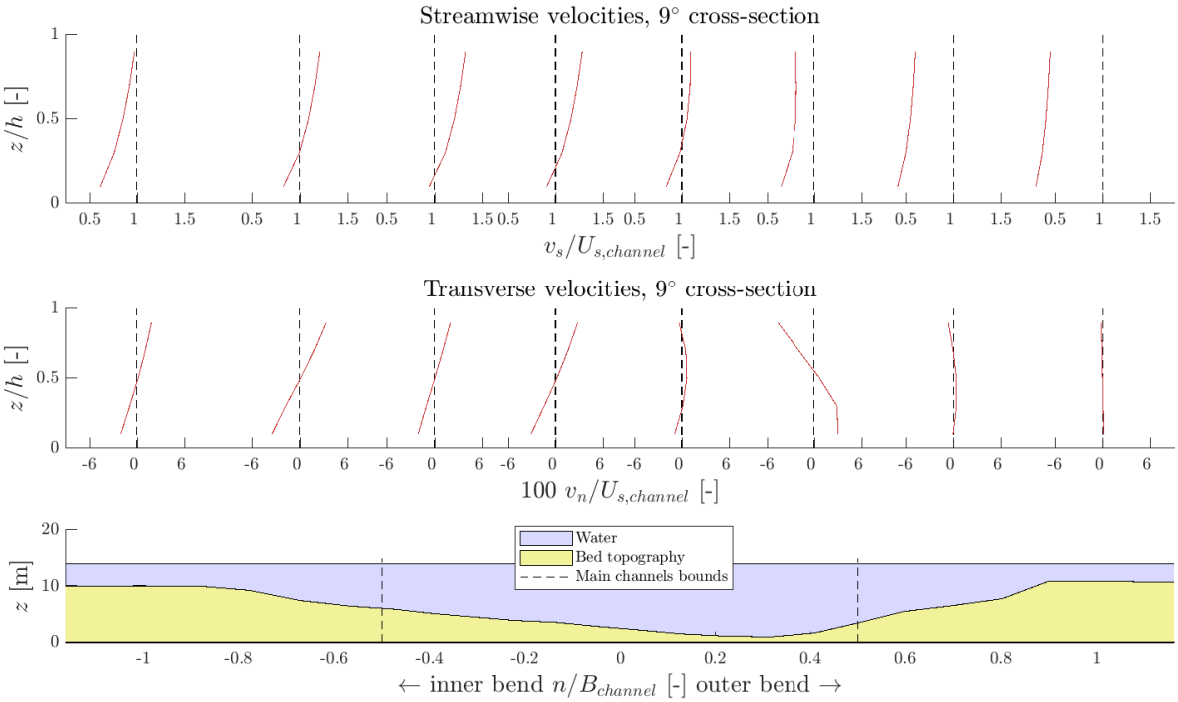

Figure E.34: Case 3, flow velocities at 9° cross-section

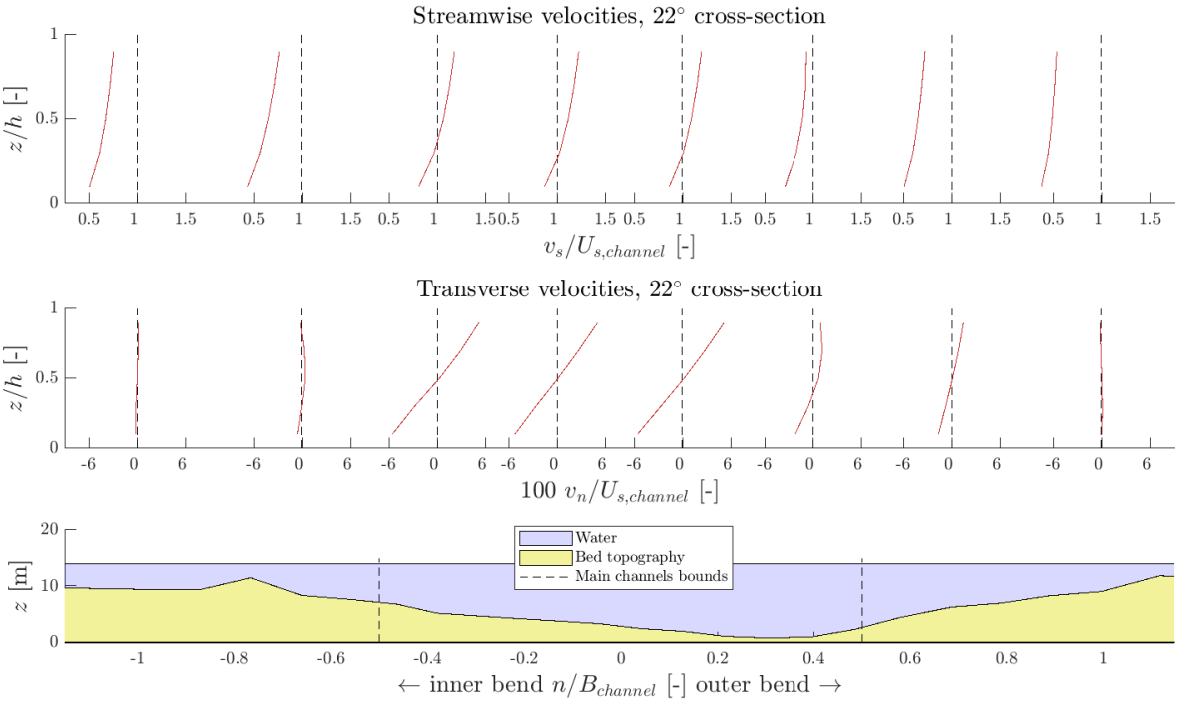

Figure E.35: Case 3, flow velocities at 22° cross-section

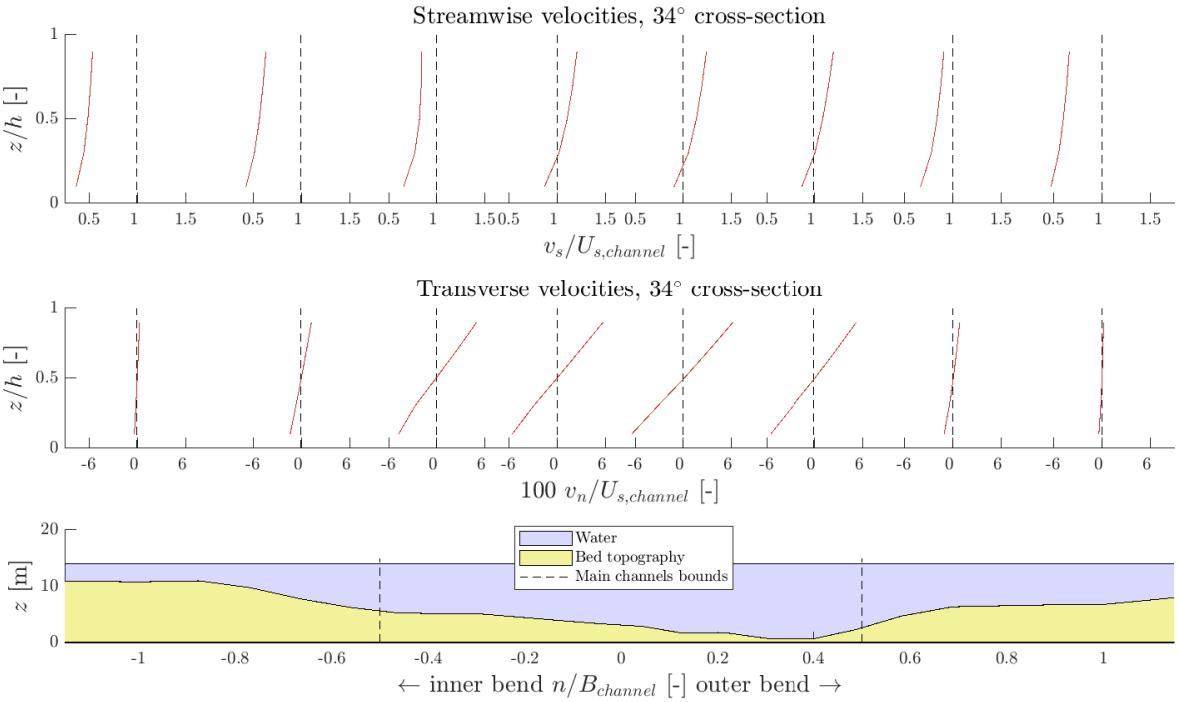

Figure E.36: Case 3, flow velocities at 34° cross-section

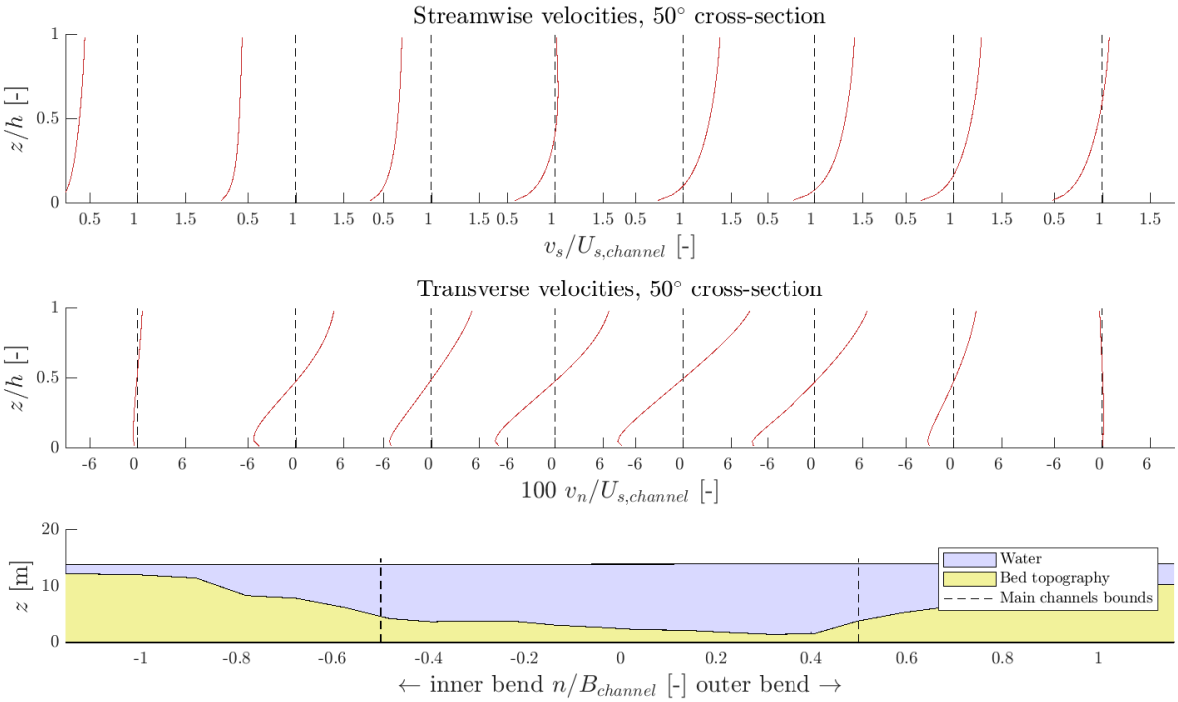

Figure E.37: Case 3, flow velocities at 50° cross-section

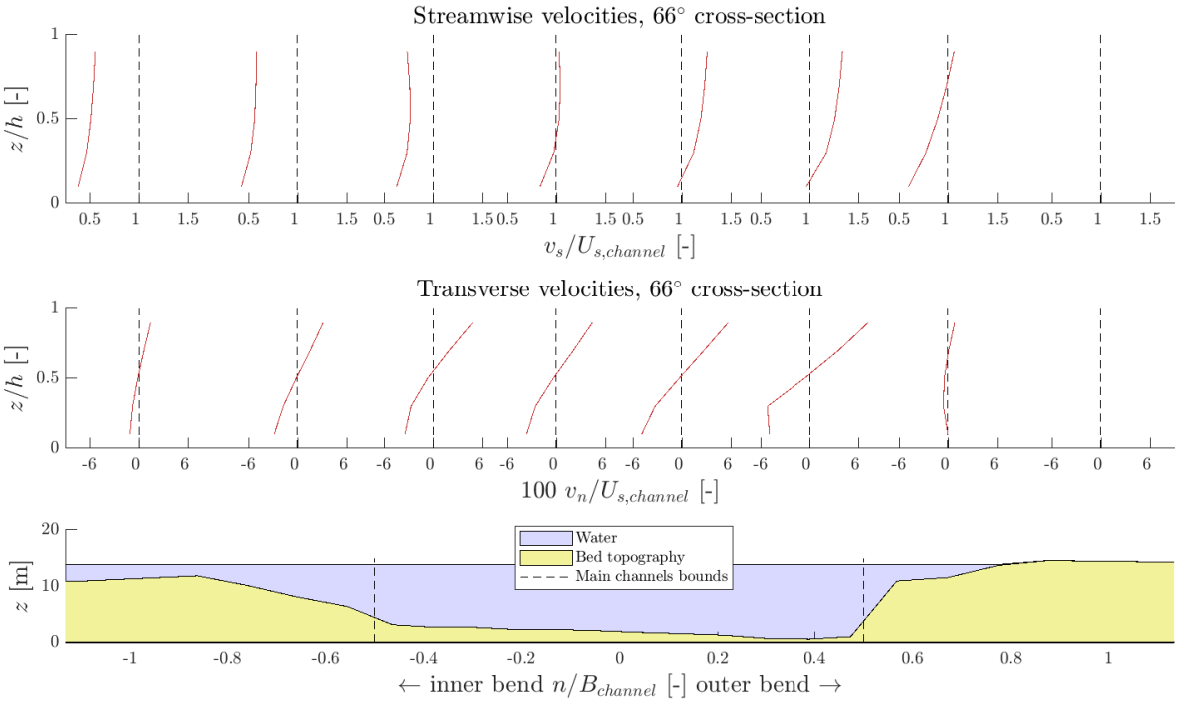

Figure E.38: Case 3, flow velocities at 66° cross-section